technische universität
dortmund

Aspects of Charge Carrier Dynamics in Germanium and Cadmium Zinc Telluride

Dissertation

zur Erlangung des akademischen Grades
Doktor der Naturwissenschaften

Fakultät Physik
Technische Universität Dortmund

vorgelegt von

Jan Lohrenz

2016

Contents

Part I

Spin Dynamics in Bulk Germanium

Introduction

In 1925, an intrinsic form of angular momentum of electrons was proposed by G. E. Uhlenbeck and S. Goudsmit [1]. In actual fact, they had identified the quantum mechanical property inherent to elementary particles that we now call spin. One unique feature of the spin angular momentum of a particle is the fact that the spin eigenstates can only have two distinct values along a certain quantization direction, denoted as spin-up $|\uparrow\rangle$ and spin-down $|\downarrow\rangle$. As each spin angular momentum can be attributed to a spin magnetic moment, this novel fundamental property was able to be observed and manipulated through the use of magnetic fields. Indeed, three years earlier in 1922, O. Stern and W. Gerlach had already experimentally shown that particular atoms possess a quantized magnetic moment that is related to their spin angular momentum [2]. While this study became one of the best-known experiments of quantum mechanics, it also set the foundation for the field of nuclear magnetic resonance (*NMR*), established by I. I. Rabi. Together with the work of F. Bloch and E. M. Purcell on NMR spectroscopy, the consequential advances in medical imaging by magnetic resonance tomography became one of the most prominent applications that are publicly associated with the term *spin*.

In contrast, phenomena related to the electron spin received considerably less public attention until the 1970s, when the effect of tunnel magnetoresistance (*TMR*) was discovered [3]. Together with the following discovery and technological improvement of giant magnetoresistance (*GMR*), which was honored with a Nobel Prize in physics for A. Fert and P. Grünberg, as well as the development of GMR-based HDDs and MRAM, carrier spin phenomena gained popularity. In relation to this progress, a whole branch of novel application-oriented physics has emerged within the last three decades, which we now refer to as spin-based electronics or *spintronics* [4–6].

The field of spintronics aims to implement the spin degree of freedom of the charge carriers in a classical computation scheme by solely conveying the spin orientation of the carriers in order to overcome power dissipation related to the transport of the charge carriers. The experimental breakthrough in this field of research was

to a large amount enabled by innovations in sample-preparation. Therein, especially the progress on molecular beam epitaxy (*MBE*) made it possible to fabricate sufficiently pure crystals in order to suppress undesired scattering of the spin-carriers [5]. Moreover, MBE facilitated the production of thin layers on the scale of hundreds of nanometers that are typically required to observe and manipulate quantum mechanical processes such as tunneling.

Contrary to the classical computing in spintronics, the field of quantum computing aims to exploit quantum mechanical phenomena inherent to spin states such as their superposition or entanglement. Referring to bits in classical computing, the states used for quantum computing are called quantum bits or *qubits* [7]. Among other concepts, spin states are often identified as promising candidates for qubits, owing to their binary nature, as well as the relatively well-established concepts for spin injection and readout.

Both spintronics and quantum computing based on spin qubits require elevated lifetimes of the spin states or, more generally, elevated coherence times of the ensemble of spin states. However, in an actual physical system, spin carriers undergo scattering processes that lead to a relaxation of the excited state to the equilibrium state. In particular, the mechanisms that lead to such a relaxation and the timescales involved in the process markedly depend on the system that surrounds the spin or the spin ensemble. As a loss of spin information corresponds to a loss of data in spin-based computing, the longevity of a spin system is one of the key challenges in order to facilitate advances in future applications. Moreover, for the applicability in the context of quantum computing, a system must offer tools to initialize a well-defined spin state, as well as to read out the current state of the system [8].

While a variety of approaches exist in order to fulfill these requirements, the idea of optically manipulating spins in semiconductors has been of particular interest for its relatively efficient and convenient spin injection and readout [9]. The concept of optically orienting spins in a semiconductor is based on interband absorption of photons from an externally applied electromagnetic field, which leads to the excitation of electron-hole pairs. By favoring certain interband transitions by means of the manipulation of the state of polarization of the applied field, it can be achieved that the excited charge carriers have a higher probability of being in a spin-up than in a spin-down state or vice versa.

The optical readout of the spin orientation can be realized by sensing the degree of polarization of the radiative recombination of the electron-hole pairs or by monitoring reflection or transmission changes of an electromagnetic field incident

on the semiconductor. The manipulation of the population of semiconductor states with electromagnetic fields has historically been well established, based on the optical pumping technique [10], which has its roots in the work of A. Kastler [11]. More recently, the commercial availability of ultrafast mode-locked laser sources has greatly facilitated the progress on optical spin orientation and readout on timescales as low as hundreds of femtoseconds. Furthermore, mode-locked lasers enable the use of several (time-resolved) spectroscopy techniques that provide a measure of fundamental properties of semiconductor spin environments [12] such as the charge carrier dynamics.

Studies of optical spin orientation and spin relaxation have received great attention in relation to the prominent III-V semiconductor GaAs [13, 14]. Furthermore, experiments on spin phenomena have spread out widely among the III-V and II-VI compound semiconductors [15, 16], as well as nanostructures that consist of these materials [17–21].

In contrast, the scientific community has paid much less attention to the dynamics of optically injected spins in the centrosymmetric group IV semiconductors silicon (Si) and germanium (Ge). This seems surprising at first, as these materials were conveniently available from the emerging semiconductor industry early on, and silicon has historically been one of the first materials where optical manipulation of electron spins has been performed in [22]. Moreover, insight on the spin dynamics in indirect semiconductors might help to implement spintronics and quantum computing in the widely accessible silicon platform.

Another advantageous characteristic of indirect semiconductor spin systems is the fact that, due to their crystal structure, the dominant mechanism of spin relaxation that is inherent to III-V semiconductors is missing. Consequently, the spin lifetime can be expected to be considerably higher. However, indirect band gap semiconductors have their lowest conduction band minimum at a different position in k-space than their highest valence band maximum, which means that they require the interaction with quantized lattice vibrations (*phonons*) for the interband absorption of photons with energies close to the indirect band gap energy [23]. As a consequence from this reduced probability of light-matter interaction, optical experiments in this energetic regime require more elaborate experimental arrangements with higher sensitivity for indirect semiconductors. In fact, for an indirect band gap or group-IV semiconductor, the first magneto-optical analysis of spin dynamics and coherence has only been carried out recently [24, 25]. In these studies, spin coherence times of several nanoseconds for low temperatures of $T \leq 50\,\mathrm{K}$ have been found. Although the observed coherence times are already comparatively long

for bulk semiconductors, theoretical predictions point towards spin lifetimes on the order of several microseconds in high purity Ge at cryogenic temperatures [26].

Related to these promising expectations, the first part of this thesis aims to find out whether the experimental conditions demonstrated in the above-mentioned previous work on magneto-optical experiments in germanium can be improved in order to drive the applicability of germanium and indirect semiconductors in general within the field of spintronics and quantum computing. Moreover, the presented study seeks to give further insight on the fundamental properties of spin dynamics in indirect semiconductors.

In the following chapters, two different aspects of spin dynamics and optical spin injection in the indirect semiconductor germanium are analyzed with the help of experimental results obtained from all-optical experiments that utilize femtosecond laser pulses. More specifically, a pump-probe measurement scheme is applied for the analysis of the spin dynamics of the material. This technique utilizes intense laser pulses (*pump pulses*) for the excitation of the semiconductor system, whose temporal behavior is subsequently studied by monitoring transmission changes of laser pulses with much weaker intensity (*probe pulses*).

The first experimental chapter will address the fundamental optical spin injection and readout process in bulk germanium. In particular, a profound understanding of the dependence of the spin injection and readout efficiency on the involved photon energies might help to guide future experiments and applications on the choice of suitable laser systems. As recent theoretical predictions point out that the spin injection efficiency is enhanced in the energetic proximity of the indirect band gap for the case of silicon [27], one focal point of the study addresses the question of whether this effect can be observed in the analogous semiconductor germanium. To monitor the spectral dependence on the spin injection and readout process on different ranges of photon energies, samples of different thicknesses can be applied. At the same time, the reiteration of the experiment for different samples makes it possible to identify eventual dependencies on the sample orientation and doping concentration.

In a following experimental approach, the issue is addressed whether the previously predicted elevated spin lifetimes [26] on the order of hundreds of nanoseconds to several microseconds can be experimentally verified for germanium. This aspect is of particular interest for a possible future applicability of indirect semiconductors in spintronics and quantum computing, as one of the key requirements within this context is an elevated coherence time, i.e., long-term stability of the system. With regard to commercial applicability, the corresponding experiments are carried out

in the well-established telecom wavelength regime around $1.55\,\mu$m (photon energies of $0.8\,$eV).

It is to be expected that the persistence of the ensemble of oriented spins markedly depends on the application of external magnetic fields. Thus, the corresponding experiments employ the resonant spin amplification technique (*RSA*) [13], where information on the lifetimes is derived from the resonant accumulation of spin polarization oriented by consecutive pump pulses. A key advantage of this technique is that it allows for the observation of the magnetic field dependence of the spin ensemble coherence for comparatively low magnetic fields on the order of several millitesla. As the conventionally applied time-resolved Faraday rotation technique (*TRFR*) typically requires fields that are a factor of 100 higher, the choice of RSA in this study promises unique insight on the onset of spin ensemble decoherence.

Concurrently, the measurements are carried out for a variable temperature ranging down to $5\,$K. While the adaption of the spin system to higher temperatures is usually desirable in order to overcome the need for costly cooling, the study of the temperature dependence of the spin lifetimes and spin ensemble coherence times also allows for the identification of the fundamental mechanisms of spin relaxation by their characteristic temperature fingerprints. Finally, by observing how the magnetic field orientation with respect to the sample influences the RSA traces, the study aims to provide insight on how spin-oriented electrons from different conduction band minima interact.

In order to give the reader insight into the fundamental processes that are necessary to comprehend the experimental results, the first chapter of this dissertation outlines the basic principles of optical spin injection in direct and indirect semiconductors, as well as the optical readout process. In addition, the origins of spin relaxation and the corresponding terminology are introduced. Chapter 2 subsequently aims to demonstrate the experimental toolset that can be used to carry out the above-mentioned optical studies. Therein, the measurement techniques of pump-probe, TRFR, and RSA are portrayed together with the experimental setup and the particular germanium specimens that are used for the experimental studies.

Prior to the publication of this work, parts of the results presented in the first part of the thesis have been published in [28–30].

Chapter 1

Theoretical Background

The experiments carried out in the first part of the thesis investigate the spin dynamics of charge carriers in the indirect semiconductor germanium. The time-dependent study utilizes intense femtosecond laser pulses (pump pulses) to inject a macroscopic spin orientation of the charge carriers in the material, i.e., by exciting a higher number of electrons and holes with spin-up orientation than with spin-down orientation or vice versa. The ensemble of carrier spins will subsequently undergo scattering processes that lead to a relaxation of the previously excited spin polarization until the amount of spin-up and spin-down oriented carriers are equal. By reading out the spin polarization of the semiconductor with the help of a second, less intense laser pulse (probe pulse) for a variable time delay relative to the first pulse, the spin relaxation dynamics can be monitored.

In order to aid the reader's understanding of the experiments conducted in this work, a short explanation of the processes involved in spin orientation and readout as well as the dominant relaxation mechanisms will be given in this chapter. To a great extent, the information presented in the following sections is based on common literature of spin and semiconductor physics [9, 31–33].

1.1   Optical Spin Injection and Selection Rules

The process of optical spin orientation in semiconductors relies on interband absorption of photons, which leads to the excitation of electron-hole pairs. If the light incident on the semiconductor is left- or right-circularly polarized, it carries an angular momentum of -1 or 1 projected on the direction of its Poynting-vector in units of $\hbar$, respectively. When the photon is absorbed it transfers its angular momentum to the photoexcited carriers due to angular momentum conservation. According

to the quantum mechanical selection rules present in the respective semiconductor, the change of the angular momentum quantum number by a value of 1 or -1 only permits certain transitions from the initial to the final states occupied by the charge carriers.

Owing to the spin-orbit interaction of a particle's motion (represented by the angular momentum quantum number) with its spin, selectively addressing certain transitions from the valence band to the conduction band allows for favoring final states of the charge carriers with a certain spin orientation over those with the opposite orientation. Ultimately, it can therefore be achieved to orientate a macroscopic spin polarization by choosing the right photon energies and polarization of the electromagnetic field that excites the semiconductor material.

To what extent the spin ensemble is polarized, i.e., by what fraction the amount of a certain spin state of the charge carriers exceeds the other can be gauged by the degree of spin polarization (DSP), given by:

$$\text{DSP} = \frac{N_\uparrow - N_\downarrow}{N_\uparrow + N_\downarrow} \tag{1.1}$$

Here, $N_\uparrow$ and $N_\downarrow$ denote the amount of carriers with spin-up or spin-down orientation, respectively.

In the following sections, the characteristics of spin injection are outlined for direct and indirect semiconductors.

Direct Semiconductors

The selection rules for optical transitions that lead to a possible spin injection crucially depend on the crystal lattice and the resulting band structure. Admittedly, the spin-related experiments carried out within the scope of this thesis focus on indirect band gap semiconductors such as germanium, silicon and gallium phosphide. However, it is instructive to discuss the spin injection process in the prototypical direct semiconductor GaAs and subsequently discuss the specifics of indirect semiconductors.

Analogous to the hydrogen atom, it is possible to describe the possible states of both holes and electrons with a set of quantum numbers that represent their wave functions. At the Γ-point (k=0) of the band structure, the conduction band (cb) states are s-like ($l = 0$), and the valence band (vb) states are p-like ($l = 1$). Here, l denotes the eigenvalues of the orbital angular momentum **l**. Consequentially, for vb states the eigenvalues $j = |l \pm s|$ of the total angular momentum **j** can amount to ³/₂ or ¹/₂.
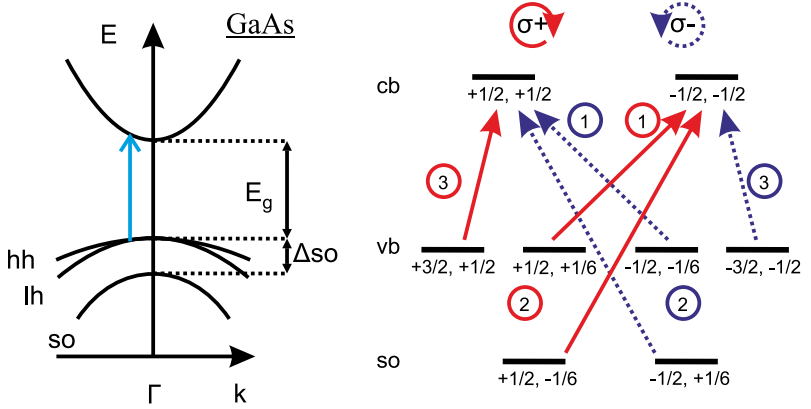
Figure 1.1: Left: band structure schematic of GaAs in the vicinity of the Γ-point. The light blue arrow illustrates a direct interband transition. Right: States of the cb and vb and their corresponding quantum numbers m_j and m_s in units of $\hbar$, taken from [34]. Possible optical transitions for right- and left-circularly polarized light are shown as red and blue arrows, respectively. The circled numbers represent the relative probability of the respective transition.

Owing to spin-orbit interaction, states with different j undergo an energetic splitting, which results in the formation of the split-off band (*so*), as depicted in Fig. 1.1, left side. The eigenvalues of the projection onto the z-axis of the total angular momentum are denoted as m_j and can posses values in the range of $-j, -j+1, \ldots, j-1, j$.

Ultimately, the cb states at the Γ-point are two-fold degenerate in spin with $m_j = -1/2, 1/2$. The vb states are all two-fold degenerate and cover $m_j = -1/2, 1/2$ for light hole, $m_j = -3/2, 3/2$ for heavy hole, and $m_j = -1/2, 1/2$ for split-off bands.

The right side of Fig. 1.1 depicts the available cb and vb states in the vicinity of the Γ-point. The corresponding quantum numbers m_j and m_s are shown right below each state, where the quantum number m_s denotes the eigenvalues of the projection of the spin angular momentum onto the z-axis. Possible transitions between the valence band and conduction band states are indicated by red solid arrows for right-circularly polarized light (σ^+), and blue, dashed arrows for left circulary-polarized light (σ^-). Since optical transitions conserve energy and momentum, only transitions with $\Delta m_j = \pm 1$ are allowed for σ^+ and σ^-, respectively.

The relative probability of each transition is given by the adjacent circled numbers in Fig. 1.1, following Fermi's golden rule calculations. For example, the excita-

tion with right-circularly polarized light with a photon energy of $E_g < \hbar\omega < E_g + \Delta so$ has a three times higher probability to excite an electron from the vb state with $m_j = 3/2$ to the cb state with $m_j = 1/2$ and $m_s = 1/2$ than to excite an electron from the vb state with $m_j = 1/2$ to the cb state with $m_j = -1/2$ and $m_s = -1/2$.

Obviously, when a huge number of electron-hole pairs are excited with σ^+ polarization for the above-mentioned photon energies, a larger fraction of electrons occupies spin-up states than spin-down states, thus creating a macroscopic spin polarization in the semiconductor.

For a given polarization of light incident on the semiconductor, it is possible to calculate the average excited spin polarization by summing up the product of the relative transition probabilities with their respective average spin m_s of the final states.

As an example, at the Γ-point, a σ^+ excitation with a photon energy of $E_g < \hbar\omega < E_g + \Delta so^1$ leads to an average spin orientation per conduction band electron of:

$$\text{DSP}_e = \frac{3 \cdot \frac{\hbar}{2} + 1 \cdot \frac{-\hbar}{2}}{4 \cdot \frac{\hbar}{2}} = \frac{1}{2} = 50\% \tag{1.2}$$

The degree of spin polarization for the case of holes can be calculated analogously. However, the corresponding final states are those of the valence band. For the above-mentioned configuration, the DSP for holes consequently reads:

$$S_h = \frac{3 \cdot \frac{-\hbar}{2} + 1 \cdot \frac{-\hbar}{6}}{4 \cdot \frac{\hbar}{2}} = -\frac{5}{6} \approx -83.3\% \tag{1.3}$$

From this simple calculation it is apparent that optical orientation is a powerful tool to induce a macroscopic spin polarization in a semiconductor for $E_g < \hbar\omega < E_g + \Delta so$.

The calculation yields a DSP of 0 for cb electrons for the case of $\hbar\omega > E_g + \Delta so$. However, the calculation of the degree of spin polarization presented in this chapter neglects transitions at $k \neq 0$, which start to play a role for increasing photon energies. For this case, the conduction band and valence band states lose their strict s- and p-likeness, respectively. As a consequence, the calculated values for the DSP only hold true for transitions exactly at the Γ-point. It is therefore still possible to excite a macroscopic spin polarization for $\hbar\omega > E_g + \Delta so$ in a real experiment.

---

[1]At room temperature, the direct bandgap and split-off energies of GaAs amount to $E_g = 1.43\,\text{eV}$ and $\Delta so = 0.34\,\text{eV}$, respectively [35].

Indirect Semiconductors

To a certain degree, the insight on the spin injection process in direct semiconductors gathered in the previous chapter can be transferred to the situation for indirect semiconductors. This is due to the fact that indirect semiconductors can also possess a local cb minimum at the Γ-point, which allows spins to be injected. However, because the absolute cb minimum is located at $k \neq 0$, phonon-scattering plays an important role in the spin injection process [27].
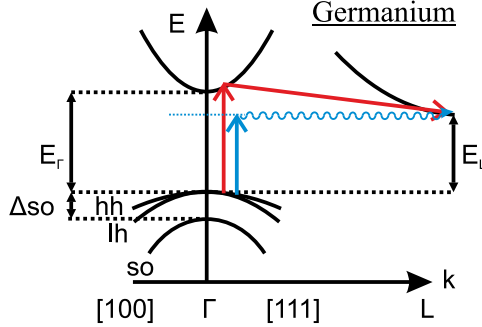

Figure 1.2: Schematic of the band structure of germanium. The absolute cb minimum is located at the L-point. Electrons injected via direct transitions with $\hbar\omega > E_\Gamma$ are scattered to the L-valley (red arrows). Indirect transitions with $E_L < \hbar\omega < E_\Gamma$ rely on a virtual state and a phonon scattering event (blue arrows).

Experimentally observable electron spin phenomena in indirect semiconductor materials originate to a large fraction from cb electrons in the lowest cb valley independent of the photon energy used for optical excitation [24]. This circumstance is a consequence of intervalley scattering processes that successively reduce the energy of electrons until they reside in the lowest cb valley (red arrows in Fig 1.2). At room temperature, this intervalley scattering happens on time scales of $\sim 200\,\mathrm{fs}$ [36–38]. The achievable electron DSP in indirect semiconductors is consequently lowered when electron-hole pairs are excited by circularly polarized light with $\hbar\omega \geq E_\Gamma$, as each scattering process has a non-zero probability of causing a spin-flip event (see Chap. 1.3).

Recent experimental studies report that for germanium the scattering from the conduction band minimum at the Γ-point to the L-valley happens via a transit state at the X-valley [39], thus further reducing the degree of spin polarization. The

reason for this transition is given by the fact that the scattering rates of $\Gamma \to X$ and $X \to$ L are higher than the immediate scattering of $\Gamma \to$ L.

For photon energies of $E_i < \hbar\omega < E_\Gamma$, where E_i denotes the lowest indirect bandgap energy, electron-hole pairs can be created with a remaining hole at the Γ-point and an electron in the indirect cb minimum, e.g., the L-valley in germanium. However, because of the mismatch of the wave vector k, a phonon scattering event is required to allow this transition. As stated before, carrier-phonon scattering has a non-zero spin-flip probability, which means that also for this kind of spin injection process the DSP is lowered.

The maximum DSP for indirect bandgap spin injection has been calculated to be 25% in the limit of $\hbar\omega = E_i$ at low temperatures [27] for silicon. As pointed out in this reference, for increasing photon energies an increasing variety and amount of different types of phonons can contribute to the thermalization in the L-valley that follows the interband transition. As a result, the DSP decreases, as an enhanced amount of scattering events increases the probability of a spin-flip.

Theoretical values for the electron and hole DSP in germanium have been calculated for injection with excess energies above the direct band gap [34]. In recent experimental studies on the spin injection efficiency, the theoretically predicted trends in this energetic regime have been partially verified [40]. In contrast, a detailed theoretical and experimental analysis of the spin injection in germanium for photon energies of $E_i < \hbar\omega < E_\Gamma$ is lacking so far. Therefore, the first experimental part of this thesis aims to provide insight into this so-far unknown regime (Chap. 3). As pointed out earlier, the optical spin injection efficiency has been calculated for indirect transitions in silicon [27]. As silicon and germanium exhibit similar structural properties, it is to be expected that the predicted overall trends may apply for both materials.

1.2 Optical Readout of Spin Polarization

Each spin angular momentum $\mathbf{S}$ can be attributed to a spin magnetic moment $\boldsymbol{\mu}_{\mathrm{S}}$ via:

$$\boldsymbol{\mu}_{\mathrm{S}} = -g\frac{\mu_{\mathrm{B}}}{\hbar}\mathbf{S} \tag{1.4}$$

(g = g-factor, μ_{B} = Bohr magneton, $\mathbf{S} = \frac{\hbar\boldsymbol{\sigma}}{2}$, $\boldsymbol{\sigma}$ = Pauli-vector = $(\sigma_x, \sigma_y, \sigma_z)^T$)

Therefore, orienting a macroscopic amount of spins in a material also changes its magnetization. Consequently, it is possible to study the spin polarization of an ensemble of particles by observing the magnetic response of the system.

The experiments conducted within the scope of this thesis will utilize the Faraday effect to sense the dynamics of spins in semiconductors. Already in 1846, Michael Faraday reported that the axis of linear polarization of an electromagnetic wave passing through a transparent medium could be changed by applying an external magnetic field [41]. With the help of Maxwell's equations, it can be shown that the magnetization $\mathbf{M}$ of a material alters the polarization axis and ellipticity of a transmitted electromagnetic wave. A detailed derivation of this result can be found in [42].

Phenomenologically, the Faraday effect can be understood as follows: In an isotropic medium, the dielectric permittivity $\boldsymbol{\epsilon}$ is reduced to a scalar, which is accurate for a cubic crystal without a macroscopic magnetization. If a magnetization is induced in the crystal, the response of the polarization of the material is altered along the direction of the magnetic field. Consequently, the symmetry of the dielectric permittivity is reduced and it gains the character of a tensor. For example, a given magnetization along the z direction $\mathbf{M} = (0, 0, M_z)^T$ leads to a dielectric tensor of the form:

$$\boldsymbol{\epsilon} = \begin{pmatrix} \epsilon_{xx} & \epsilon_{xy} & 0 \\ -\epsilon_{xy} & \epsilon_{yy} & 0 \\ 0 & 0 & \epsilon_{zz} \end{pmatrix} \tag{1.5}$$

Additionally, each linear polarized electromagnetic wave can be understood as a superposition of left- and right-circularly polarized waves with the same amplitude. Considering a wave propagating along the z direction, the complex index of refraction for each circularly polarized part (left and right denoted as - and +, respectively) of the wave $N_\pm = n_\pm + i\kappa_\pm$ is given by:

$$N_\pm^2 = \epsilon_{xx} \pm i\epsilon_{xy} \tag{1.6}$$

By recalling the formula of a plane wave propagating along the z direction

$$E(\omega, t) = E_0(\omega)e^{i\left[(n+i\kappa)\frac{\omega}{c}z - \omega t\right]}, \tag{1.7}$$

it becomes apparent that the changes of the dielectric function caused by the magnetization ultimately lead to a phase difference (circular birefringence) and a change of the amplitude of the left- and right-circularly polarized fractions of the wave (circular dichroism).

The circular birefringence causes a rotation of the linear polarization axis by the Faraday rotation angle θ_F, given by:

$$\theta_F(\omega,\mathbf{M}) \propto \mathrm{Re}(N_+ - N_-) \tag{1.8}$$

The circular dichroism changes the relative amplitudes of the different circular wave components and thus leads to an increasing elliptical polarization of the beam, which is called Faraday ellipticity:

$$\eta_F(\omega,\mathbf{M}) \propto -\mathrm{Im}(N_+ - N_-) \tag{1.9}$$

By sensing changes of a linearly polarized probe beam that passes through the material, it is therefore possible to observe the temporal evolution of an ensemble of spins induced by a circulary polarized intense pump beam. An in-depth explanation of the principle of pump-probe measurements will be given in Chap. 2.1.

By applying an external magnetic field, the spin ensemble undergoes a collective Larmor precession, in which the precession frequency gives rise to the g-factor of the corresponding spin-carrying particles:

$$\omega_{\mathrm{L}} = \frac{g\mu_{\mathrm{B}}}{\hbar}B \tag{1.10}$$

The experimental technique of monitoring Faraday rotation in a pump-probe measurement is referred to as time-resolved Faraday rotation (TRFR) and will be described in more detail in chapter 2.2.

1.3   Relaxation of Spin Polarization

In general, a system, which is excited to non-equilibrium conditions, will relax to its thermodynamic equilibrium on a certain time scale. Accordingly, a macroscopic spin polarization that has been oriented in a semiconductor will relax or dephase to a state where the average observable spin orientation is zero.

Within the field of spintronics or quantum computing, it is of great interest to minimize the rate at which the spin degree of freedom of a single particle or an ensemble of particles loses its defined state because this would correspond to a loss of data or usability of the stored information [4]. However, when the spin state of

an excited spin ensemble is read out in an experiment, the observed time scale of the relaxation of the spin-related signal can be of different origin depending on the alignment of the setup. More specifically, within an all-optical study the orientation of the excitation and readout laser beams, as well as the orientation of an eventual magnetic field are the parameters that determine which process can be resolved in the data.

With regard to the discussion of the experimental results on the transient dynamics of an ensemble of spins that will be given later in this thesis, this chapter aims to clarify how the experimentally resolved spin information is lost for each configuration. To this end, the terminology of the different spin lifetimes or coherence times is introduced. Afterwards, a short, phenomenological overview of the physical mechanisms that lead to a loss of spin information is given. With respect to the experimental study, the explanations will mainly focus on the specifics of electron spins in bulk group IV semiconductors.

Terminology of Spin Lifetimes

The intrinsic spin lifetime T_s is the time constant at which an excited non-equilibrium spin polarization, i.e., a higher amount of spin-up states than spin-down states or vice versa, will relax to its equilibrium state, where the corresponding spin-up and spin-down states are equally distributed. Strictly speaking, it is only viable to address the spin lifetime T_s when no external magnetic field is applied to the material.

Obviously, a conduction band electron or a valence band hole can only contribute to a macroscopic spin polarization of their type until they eventually recombine. Therefore, the carrier lifetime constitutes an upper limit for the spin lifetime T_s.

When an external magnetic field is applied, the rate of loss of spin information is usually quantified by the longitudinal spin decay time T_1 and transversal spin decoherence time T_2, which are defined within the Bloch equations [4, 43]. Which one of these time constants is addressed in an experiment depends on the orientation of the magnetic field with respect to the direction of propagation of the laser pulses that induce and probe the spin polarization [44].

The (longitudinal) spin relaxation time T_1 is addressed if the direction of propagation of the laser beams and the magnetic field are parallel (Faraday geometry). In this configuration, the spin-up and spin-down states are energetically split due to the Zeeman-effect. Therefore, an equilibration of the spin polarization excited along this direction corresponds to an energetic relaxation from the upper to the lower Zeeman-level with the time constant T_1. This requires energy to be taken

from the spin system, which is usually caused by phonon-scattering that transfers energy from the spin-carriers to the lattice.

The (transverse) spin decoherence time T_2 , in contrast, describes a loss of spin information for a perpendicular alignment (Voigt geometry) of the magnetic field with respect to the direction of propagation of the laser pulses. For this orientation, the excited spin polarization undergoes a Larmor precession in the plane normal to the orientation of the magnetic field. T_2 therefore corresponds to the time scale on which the projection of the spin orientations of the individual carriers lose their coherence inside the plane of Larmor precession due to spin-flip events or fluctuations of the Larmor precession frequency. In contrast to processes related to T_1, the equilibration in the context of T_2 does not necessarily correspond to a loss of energy of the carriers.

If an ensemble of spins with different Larmor precession frequencies is probed in Voigt geometry, spins with different ω_L run out of phase. However, this dephasing happens in an organized, well-defined way, such that it is possible to reverse the process with the help of, e.g., spin-echo techniques [4, 45]. The observed relaxation time constant is called dephasing time in this case, denoted as T_2^*. In general, the decoherence time and the reversible dephasing time obey the inequation $T_2 \geq T_2^*$. Results from experiments that are insensitive to whether or not the observed spin dephasing is reversible usually use the term T_2^* to provide an estimate of the lower boundary of the spin dephasing time.

The longitudinal spin relaxation time T_1 will not be addressed in the experimental study conduced in the context of this thesis, since the experimental setup cannot be used in Faraday geometry. However, the time scales T_1 and T_2 or T_2^* do not differ drastically and T_1 can be estimated from T_2 by the inequation $T_2 \leq 2\,T_1$ [4, 46]. Furthermore, for conduction band electrons the approximation $T_2^* \approx T_2$ can be used [4].

Obviously, the existence of a spin polarization is a necessary condition for the observation of spin coherence. Thus, the spin lifetime T_s serves as an upper boundary for T_1 and T_2. Ultimately, the hierarchy of the different types of relaxation times yields:

$$T_s \geq T_1 \geq T_2 \geq T_2^* \tag{1.11}$$

In cases where aspects of spin relaxation are discussed irrespective of the underlying relaxation mechanism, the term τ_S will be used throughout this thesis.

Relaxation Mechanisms

In general, spin information can be lost when spin-altering processes occur at random times or change the orientation of the spin in random directions. For these occurrences, the spin polarization or its projection along a certain direction will exponentially approach its initial, unexcited state where the spin orientation is completely randomized.

The corresponding time scales of the spin relaxation and decoherence have been introduced above. Now, those fundamental processes that cause the loss of spin information are briefly portrayed, which are most relevant for the experimental study presented in this thesis. A more detailed overview of spin relaxation mechanisms can be found in common literature, such as [9, 32].

In principle, these relaxation channels are consequences of mutual interactions of the spin carriers or interactions with their environment, e.g., scattering with phonons from the surrounding crystal. As the scattering with phonons becomes less probable for low temperatures, experiments that focus on the limits of spin longevity are usually carried out at cryogenic temperatures of $\approx 4\,\mathrm{K}$.

The Elliot-Yafet type relaxation, reported by Elliot [47] and Yafet [46], results from the fact that electronic Bloch states mix spin-up and spin-down states in a semiconductor due to spin-orbit interaction. As a consequence of this, normally spin-independent scattering events like electron-phonon scattering can cause a spin-flip and therefore lead to a relaxation of the spin polarization [48]. As a result, for Elliott-Yafet relaxation the spin relaxation rate $\frac{1}{\tau_S}$ is proportional to the momentum relaxation rate $\frac{1}{\tau_p}$

$$\frac{1}{\tau_S} \propto \frac{1}{\tau_p},\tag{1.12}$$

with the accompanying factors depending on the band structure, the spin-orbit splitting energy, and the excess energy of the electrons [9].

The temperature-dependence of the Elliot-Yafet relaxation for the case of low doping and/or optically excited carrier concentrations in a semiconductor is given by [4, 9]:

$$\frac{1}{\tau_S(T)} \propto \frac{T^2}{\tau_p(T)}\tag{1.13}$$

To estimate the temperature dependence, it is therefore necessary to know the temperature dependence of the momentum scattering.

The D'yakonov-Perel mechanism is a spin relaxation channel in crystals without an inversion center, such as GaAs [49]. In these non-centrosymmetric semiconductors, spin-orbit interaction causes the degeneracy of the conduction band

states with different spins to be lifted for $k \neq 0$. This case is mathematically equivalent to an internal magnetic field whose magnitude depends on the wave vector k. Due to the dependence of the Larmor precession frequency on the magnetic field amplitude (c.f. (1.10)), scattering events that cause a change of the wave-vector of the electrons cause the spins to precess at different frequencies and the spin ensemble loses its coherence.

Another relaxation process is given by **Hyperfine Interaction of the electron spins with nuclear spins**. As the orientations of the nuclear spins of the lattice are usually unorganized, they create a weak, random magnetic field. The interaction between this effective field with the electron spins causes them to be altered randomly, and thus the spin coherence vanishes. The relaxation related to hyperfine interaction usually is weak compared to the other processes. However, when other relaxation mechanisms that are related to the electron motion do not apply, the relaxation due to hyperfine interaction can dominate [32].

In detail, which of the above-mentioned relaxation channels has the biggest impact on the overall spin equilibration depends on the properties of the semiconductor material that contains the spin carriers, such as its doping concentration, concentration of optically injected charge carriers and externally applied fields.

As already mentioned, the experimental study in the first part of this thesis focuses on the indirect group IV semiconductor germanium. The inversion symmetry inherent to group IV semiconductors rules out the Dyakonov-Perel relaxation mechanism, which makes them promising candidates for spin systems with elevated spin lifetimes. In the review "Spin dynamics in semiconductors", Wu et al. state that, depending on the insulating state of n-type germanium, either the Elliott-Yafet mechanism or the hyperfine interaction dominate the spin relaxation process ([48] and references therein). Anticipating the experimental results of this thesis, it will be seen that the experimental data indicates the Elliott-Yafet type relaxation to be the dominant relaxation channel.

For germanium, P. Li et al. [26] have calculated the intrinsic spin lifetimes with a theoretical model based on Elliott-Yafet type relaxation that takes into account electron-phonon scattering and the consequential intervalley scattering, i.e., scattering of the electrons from one L-valley to another. It will later be shown that up to a certain point these theoretical results are in good agreement with the experimental results obtained in this thesis.

Chapter 2

Experimental Methods and Sample Characterization

While the surrounding parameters and the addressed physical aspects of part I and II of this thesis are indeed highly different, their underlying experimental principles and measurement techniques are to some extent identical. Both have in common the utilization of ultrashort laser pulses in a pump-probe measurement scheme to study specific physical phenomena. In detail, the time dependence of different effects in the particular semiconductor specimen is investigated by probing the respective transmission changes.

In section 2.1, the pump-probe technique is illustrated, which lays the foundation for nearly all the experiments conducted within this thesis. Furthermore, the time-resolved Faraday rotation (TRFR) and resonant spin amplification (RSA) methods are demonstrated, which facilitate the study of spin dynamics in semiconductors. Chapter 2.4 portrays the experimental setup in more detail and gives an overview on the parameters of the utilized laser systems. Ultimately, the properties of the studied semiconductor material germanium are summarized in chapter 2.5.

2.1   Pump-Probe Technique

The pump-probe technique is a well-known tool for time-resolved spectroscopy on the femtosecond time scale. The central idea is to induce a physical effect within a sample utilizing an intense ultrashort laser pulse called *pump pulse*. The excited effect will subsequently relax until the next pump pulse of the pulse train hits the sample after the repetition period $T_{\mathrm{rep}} = {}^1/f_{\mathrm{rep}}$ of the laser system. In addition, another much weaker *probe pulse* is spatially superimposed with the pump on the

sample. By detecting the transmission of the probe beam[1], it is therefore possible to detect the momentary transmission changes that originate from the excitation induced by the pump beam. In most cases, one initial laser pulse is split into a pump and probe fraction in order to guarantee temporal stability. This way, problems caused by the timing jitter, i.e., the fluctuations of temporal pulse positions of consecutive laser pulses, can be overcome.

The exact time at which the excitation and relaxation cycle is probed depends on the time of flight difference of the pump and probe beam and thus on the relative optical path length. Consequently, continuously detecting the transmitted probe beam while increasing or decreasing the optical path length of one of the beams enables the study of the temporal evolution of the transmission changes. The experimental implementation of this scheme is most commonly realized by moving a pair of orthogonal mirrors in one of the beam paths with the help of a motorized linear stage (see chapter 2.4). The rate at which the time of flight $\Delta\tau$ changes with the optical path length Δx is determined by the speed of light c:

$$\Delta\tau = \frac{\Delta x n}{c} \tag{2.1}$$

As the experiments are carried out in ambient conditions, the deviations caused by $n_\mathrm{air} \neq 1$ are negligible. Since commercially available linear stages commonly feature minimum incremental steps that correspond to one femtosecond, the limiting factor of the temporal resolution is the pulse duration τ_p, given by the laser system. In the case of the experiments conducted within this thesis, the pulse duration τ_p usually is on the order of $\sim 100\,\mathrm{fs}$ (c.f. chapter 2.4).

The application of the pump-probe technique allows the replacement of elaborate electronics that feature high temporal resolutions, such as streak cameras, with ordinary, commercially available photodiodes. As the temporal resolution is achieved in an indirect manner, the pump-probe technique makes it possible to average individual data points over elevated periods of time. This and the use of modulation techniques of the optical beams together with lock-in amplifiers (c.f. Chap. 2.4) facilitates a significant increase of the signal to noise ratio compared to other techniques, which makes pump-probe spectroscopy the method of choice for many time-resolved optical experiments.

---

[1]In this context, the term *beam* refers to the train of optical pulses, which usually has the visual impression of a solid beam due to its high repetition rate.

2.2 Time-Resolved Faraday Rotation (TRFR)

In chapter 1.2, the fundamental principles of Faraday rotation have been described. However, in order to study the temporal evolution of a spin ensemble, the detection of Faraday rotation has to be integrated into a pump-probe optical measurement scheme.
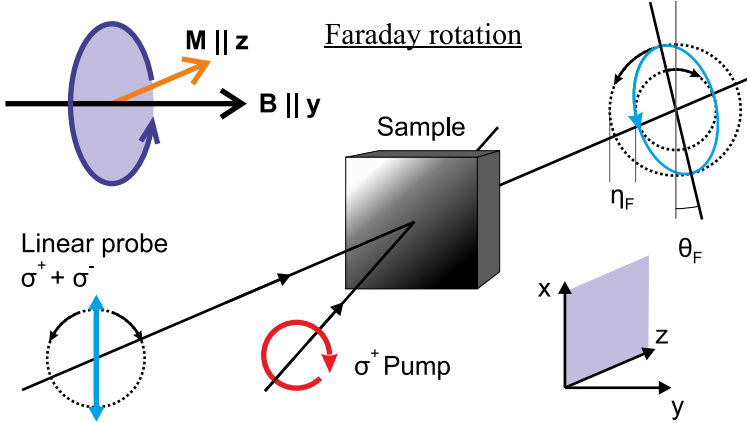

Figure 2.1: Schematic of the Faraday rotation process in a semiconductor sample. The right circular (σ^+) pump pulse induces a magnetization **M** along the z direction. The linear probe beam experiences a change of its initial linear polarization angle and an increase in ellipticity. If an external magnetic field is applied along the y-axis, the magnetization will undergo a Larmor precession in the x-z-plane.

Figure 2.1 depicts the role of Faraday rotation and ellipticity in a pump-probe setup for the case of a right circular pump and a linear polarized probe beam. The σ^+-pump pulse orientates a spin polarization in the semiconductor sample, which leads to a macroscopic magnetization along the z-direction. The linear probe beam consequently undergoes a rotation of its polarization angle and a change of its degree of elliptical polarization according to equations (1.8) and (1.9). If an external magnetic field **B** is applied along the y-axis, the spin ensemble will start to precess in the x-z-plane with the Larmor frequency ω_L given by equation (1.10). Experimentally, θ_F and η_F can be quantified by sensing amplitude changes of orthogonal polarization components.

In a semi-classical description, the carriers in a crystal are characterized by their effective mass m^* instead of the mass of the respective elemental particle, e.g., effective electron mass m_e^* instead of m_e. This correction can be used describe electrons in a semiconductor by means of the well-known characteristics of free electrons. Contrary to this approach, the notation of the Larmor frequency utilizes an effective g-factor g^* rather than an effective mass m^*. This is indeed helpful, as the effective mass depends on the particles' position in k-space. The Larmor precession frequency consequently reads:

$$\omega_L = \frac{g^* \mu_{\mathrm{B}}}{\hbar} B \tag{2.2}$$

The Larmor precession of the spin ensemble leads to a periodic change of the magnetization's projection onto the z-axis and therefore to a periodic change of θ_F. As the ensemble incurs a decoherence according to T_2^* (c.f. chapter 1.3), the observed change in the Faraday rotation signal can be modeled by:

$$\Delta\theta_F \propto \exp\left(\frac{-(t-\tau_0)}{T_2^*}\right) \sin(\omega_L(t-\tau_0)) \tag{2.3}$$

Here, τ_0 denotes the time where pump and probe are in perfect temporal overlap at the sample position.

A characteristic TRFR signal is depicted in Fig. 2.2, showing the temporal evolution of the pump-induced changes of the Faraday rotation or ellipticity. The figure includes an illustration of the orientation of **M** for one Larmor precession cycle.

At $t = \tau_0$, the pump pulse hits the sample and excites a spin polarization along the z-axis, which leads to an initial displacement of θ_F and/or η_F. Due to the externally applied magnetic field along the y-axis, the spin ensemble starts to precess with the frequency ω_L, and the signal periodically changes its sign. During this precession, spin-flip events caused by scattering processes, or dephasing of the ensemble causes the magnetization to decrease exponentially.

Recording a TRFR signal for several precession cycles allows the determination of the Larmor frequency of the excited carrier ensemble and the derivation of the corresponding effective g-factors, which can be used to identify the origin of the spin signal, i.e., what type of carriers contribute to the signal. Furthermore, observing the exponential decay of the transient facilitates the determination of the lifetime or decoherence time of the spin ensemble. However, in order to acquire reliable values of T_1 or T_2^*, it is necessary to trace a sufficient portion of the decaying signal.

The maximum delay time until which the signal can be recorded is given by the maximum distance of the linear stage. Therefore, relatively long coherence times
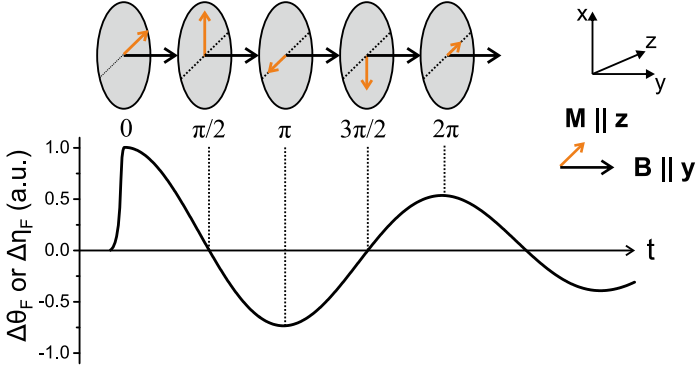
Figure 2.2: Prototypical time-resolved Faraday rotation (θ_F) or ellipticity (η_F) signal according to equation (2.3) for an external magnetic field along the y-axis and an initial magnetization along the z-axis. For characteristic phase intervals, the orientation of the magnetization **M** within the x-z plane is sketched above the graph.

exceeding several nanoseconds cause the TRFR method to become inconvenient, as motorized linear stages with lengths of several meters are expensive and difficult to handle. Moreover, in order to determine significant values of g^* with the TRFR technique, magnetic fields with relatively high amplitudes on the order of $\sim 1\,\mathrm{T}$ have to be applied, as a sufficient amount of Larmor precession periods have to be recorded.

Under certain conditions, it can be advantageous to sweep the magnetic field instead of the pump-probe delay in order to overcome these problems. Within this approach, the spin coherence time is deduced indirectly from the line shape of the observed resonances of the spin polarization. Furthermore, the spin lifetimes and coherence times can be recorded for zero magnetic field and magnetic fields as low as equivalent to one full Larmor precession cycle per pulse repetition period, respectively. Therefore, fundamental insight on the onset of spin ensemble decoherence can be obtained, which remains hidden when the TRFR method is used. The corresponding experimental technique is called resonant spin amplification (RSA) and will be illustrated in the next chapter.
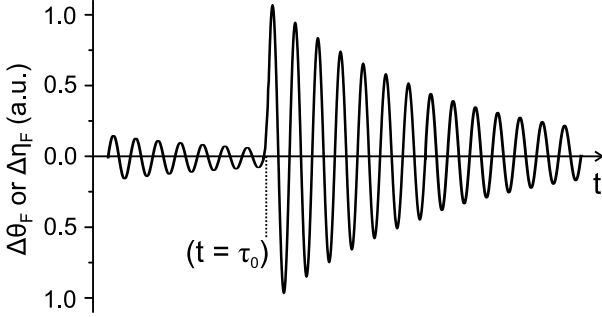
2.3   Resonant Spin Amplification (RSA)

Figure 2.3: Prototypical TRFR signal in the RSA regime. For nominally negative delay times ($t < \tau_0$), the remaining spin polarization from the preceding pump pulse can still be observed. Depending on the phase of the Larmor precession cycle, subsequent pump pulses will add up to or deplete the persistent spin polarization at $t = \tau_0$.

As stated above, the feasibility of TRFR measurements suffers from elevated spin coherence times. However, once coherence times exceed the repetition period T_{rep} of the utilized pulsed laser source, spin polarization induced by consecutive pump pulses can accumulate. This regime, as well as the consequent experimental technique, are referred to as resonant spin amplification (RSA). In this case the TRFR transient will be of the form of Fig. 2.3. This appearance can be understood by recalling the fact that nominally negative delay times in a pump-probe measurement correspond to effects that have been induced by previous pump pulses and have not fully decayed during the laser repetition period.

Whether the spin polarization is enhanced or depleted depends on the Larmor frequency and the repetition period of the laser. If the repetition period T_R is an integer multiple of the Larmor precession period

$$T_R = n\frac{2\pi}{\omega_L},\tag{2.4}$$

the spin polarization induced by subsequent pulses will constructively interfere. For the case where equation (2.4) is not fulfilled, the spin polarization is depleted. This process can be thought of as summing up an infinite amount of vectors with random orientations inside a plane, which add up to zero.
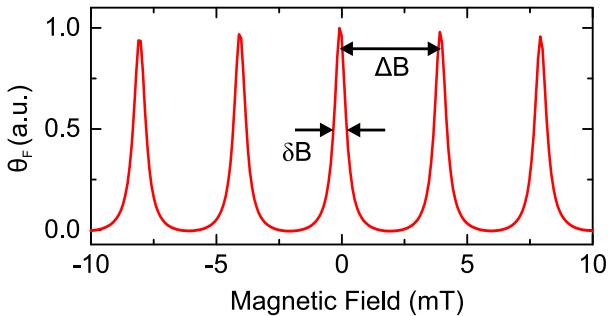
Figure 2.4: Schematic RSA trace that can be observed by sweeping the magnetic field while detecting the Faraday rotation for a given (negative) delay time. The first and second side peaks correspond to one or two full Larmor precession cycles within the laser repetition period T_R, respectively.

First applied by Kikkawa and Awschalom in 1998 [13], the RSA method relies on sweeping the magnetic field while detecting the Faraday rotation of the sample at a fixed (negative) delay time. The spin polarization and therefore also the Faraday rotation will then cycle through a series of resonance peaks as depicted in figure 2.4. In this picture, the spacing between each peak represents the Larmor frequency and therefore the effective g-factor by:

$$\Delta B = \frac{h}{g^* \mu_B T_R} \tag{2.5}$$

From this equation it is apparent that within the RSA regime the usage of laser sources with comparatively high repetition rates is favorable, as the peak spacing is narrowed for increasing pulse intervals. Laser systems with lower repetition rates would consequently require a higher precision of the external magnetic field in order to distinguish between adjacent resonance peaks. Furthermore, instabilities of the magnetic field become more problematic, as the spin ensemble excitation can shift off and on resonance, significantly increasing signal fluctuations.

Most importantly, the width of each resonance peak in an RSA trace corresponds to the spin lifetime or coherence time of the spin ensemble for the given value of the magnetic field. In particular, the width δB of an RSA peak is linked to a lifetime τ via:

$$\tau = \frac{h}{\pi g^* \mu_B \delta B} \tag{2.6}$$

Phenomenologically, this can be understood by recalling the picture of an RSA measurement being a summation of vectors that resemble the spin polarization: For the case of infinitely long spin coherence times, all of the vectors have the same amplitude. The sum of these vectors therefore amounts to infinity when the resonance condition is fulfilled. However, if the excitation of subsequent pump pulses is non-resonant, the signal instantly amounts to zero, as it resembles the case of summing up an infinite amount of vectors with random orientations. Thus, the corresponding RSA peak in this hypothetical case would corresponds to a Dirac δ-function. For finite spin lifetimes, however, the RSA measurement resembles the case of summing up a series of vectors with random orientations but with decreasing amplitude. Hence, the summation does not instantly give the value zero for small deviations from the resonance condition and the peak is broadened.

The widths of RSA peaks at different magnetic fields are related to different relaxation mechanisms, which have been described in chapter 1.3. The peak around zero magnetic field indicates the spin lifetime T_s, similar to the Hanle effect [9], while for resonance peaks with $B \neq 0$ (which shall later also be referred to as *side peaks*) spin ensemble decoherence must be taken into account and the width is given by the decoherence time T_2^*.

If the differences between the relaxation mechanisms are neglected, a series of Lorentzian peaks as depicted in Fig. 2.4 can also be expressed in an analytical form, which reads [50]:

$$\mathrm{FR}(\Delta t, \omega_\mathrm{L}) = \frac{A}{2} \exp\left(-\frac{\Delta t + T_\mathrm{R}}{\tau_\mathrm{S}}\right) \frac{\cos(\omega_\mathrm{L}\Delta t) - \exp(T_\mathrm{R}/\tau_\mathrm{S})\cos[\omega_\mathrm{L}(\Delta t + T_R)]}{\cos(\omega_\mathrm{L}T_\mathrm{R}) - \cosh(T_\mathrm{R}/\tau_\mathrm{S})}$$

(2.7)

Here, A is an amplitude factor with angular unit. In a realistic case, the intrinsic magnetic field dependence of the parameter τ_S must also be taken into account in order to incorporate the typical decrease of the spin lifetime with increasing field. In an actual experiment, the function 2.7 can be used to fit an entire RSA trace in order to study the g-factors involved in the signal. Although, for a more detailed analysis of the dependence of the spin lifetimes and coherence times on the magnetic field and temperature every peak has to be fitted individually.

2.4   Experimental Setup

The experimental setup used to trace the above-mentioned TRFR and RSA signals is outlined in figure 2.5. Two different mode-locked laser sources are used that emit pulse trains with repetition rates between 200 kHz and 90 MHz. The laser system with lower repetition rate is used for most TRFR measurements within this thesis. It consists of an amplified Ti:Sa oscillator (Coherent Micra and RegA), which seeds an optical parametric amplifier[2] (OPA), which is used to spectrally tune the emitted laser pulses. The other source is an erbium doped fiber laser (Toptica FFS) that is utilized for the RSA measurements, which require high repetition rates. The specifications of the utilized laser systems are summarized in table 2.1.

After the pulse train is emitted by the laser source, it passes through a polarizing beam splitter cube (PBSC) in order to split the pump and probe beams and simultaneously define their linear polarization state. The relative power between the beams can be adjusted by tilting the linear polarization axis of the initial beam in front of the PBSC by using a half-wave plate ($\lambda/2$). In order to manipulate the beam diameter, the pump beam subsequently passes a telescope. In a next step, the pump pulses are circularly polarized by a quarter-wave plate ($\lambda/4$) and are finally focused onto the sample.

With regard to the tunability of the relative time delay between the pump and probe pulses, the probe beam passes a retroreflector on a motorized linear stage. The linearly polarized probe beam is subsequently superimposed with the pump beam onto the sample.

It is favorable to adjust the spot sizes of both beams in the plane of the sample in such a way that the pump spot is at least the same size as the probe spot. Following Gaussian beam optics, the focal spot size and the beam waist in front of a focusing lens are inversely proportional. Therefore, the telescope within the optical path of the pump has to make sure that the pump beam diameter is smaller than the probe beam before they pass the lens in front of the sample. For the experiments presented in this part of the thesis, the spot sizes in the sample plane are adjusted to $\approx 100\mu m - 200\mu m$.

After passing through the sample, the probe beam is again collimated, while the residual pump beam is blocked. The transmitted probe beam is then split by a Wollaston prism (WP). The WP is an optical device that consists of two birefringent prisms cemented together with their optical axes perpendicular to each other. As

---

[2]Further information on the working principles and the configuration of the utilized optical parametric amplifier can be found in [51].
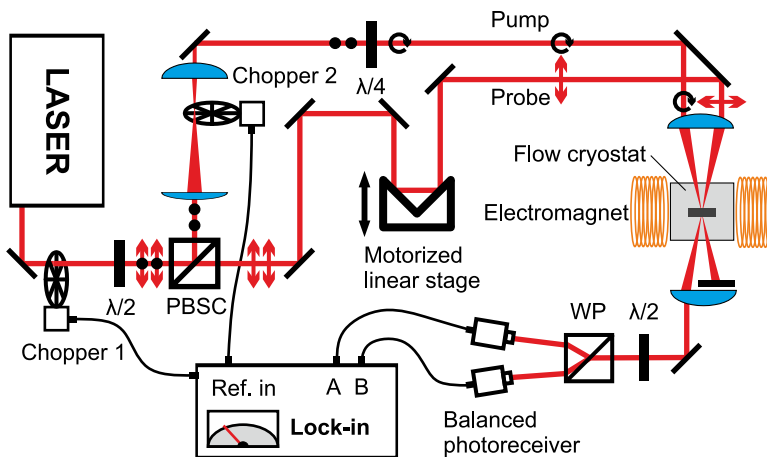
Figure 2.5: Schematic experimental setup for the detection of time-resolved Faraday rotation or resonant spin amplification.

a result, an initial beam with random linear polarization that passes through the Wollaston prism is split into two perpendicularly polarized beams. The intensities of both individual parts of the probe beam are detected with photodiodes, while the intensity distribution can be tuned by rotating a half-wave plate in front of the WP. The signal on each photodiode A and B is monitored with a Lock-in amplifier utilizing mechanical optical choppers to modulate the pump or probe beam[3].

The measurement of TRFR and RSA traces requires an elevated level of noise suppression, especially since the signals are expected to be comparatively low in the present case of indirect semiconductors [24] (c.f. Chap. 1.1). Thus, a balanced photodetection scheme is used. To this end, in a first step, the pump beam is blocked and the photodiode signal is monitored while the beam is modulated using chopper 1 as seen in Fig. 2.5. The half-wave plate in front of the WP is then adjusted such that both signals A and B are of the same magnitude, i.e., the difference signal A-B amounts to zero. Afterwards, chopper 1 is switched off and the pump beam is modulated with the second chopper. By detecting the signal difference A-B with the reference frequency of the chopper in the pump beam, it is then possible to monitor

---

[3]The usage of mechanical choppers is viable as long as the chopping frequency is much smaller than the laser repetition rate, as in this case the pulse train can be treated as a continuous beam.

changes of the polarization axis of the probe beam that are induced by the pump beam.

In principle, this experimental approach rules out most sources of noise that originate from intensity fluctuations of the laser source as they influence both signal components A and B in the same way. In the best case, the noise level is limited to the shot noise, which appears in electric signal processing and in the photon flux emitted by the laser source [52]. As several other sources of noise decrease with higher frequencies, it is instructive to modulate the signal at the highest applicable frequency, within the boundary that the modulation frequency remains much smaller than the laser repetition rate. Therefore, the pump beam is chopped in the focal plane of the telescope, as the minimal spot diameter allows for a minimal slit size of the chopper blade. Ultimately, modulation frequencies up to 3.5 kHz can be applied within the described experimental setup.

For the experimental study, the utilized germanium samples are kept in a flow cryostat at temperatures down to ≈ 5 K. As the probability of phonon scattering usually is inversely proportional to the temperature, low temperatures commonly favor a persistent spin coherence. However, most measurements within this thesis are carried out at around 8 K since this allows for a significantly lower liquid helium consumption and most of the studied physical properties do not change drastically within this temperature range.

As a source for an external magnetic field, two different electromagnets and power supplies are used to deliver either monopolar magnetic fields up to 700 mT or continuously tunable bipolar magnetic fields up to 100 mT.

Laser system	Coherent RegA + OPA	Toptica FFS
Repetition rate f_{rep}	$200\,\mathrm{kHz} - 250\,\mathrm{kHz}$	$90.5\,\mathrm{MHz}$
Repetition period T_{R}	$4\,\mu\mathrm{s} - 5\,\mu\mathrm{s}$	$11.05\,\mathrm{ns}$
Pulse width τ_p	$\approx 60\,\mathrm{fs}$	$\approx 100\,\mathrm{fs}$
Central wavelength λ_c	$1200\,\mathrm{nm} - 1650\,\mathrm{nm}$	$1550\,\mathrm{nm}$
Central photon energy E_{phot}	$0.75\,\mathrm{eV} - 1.03\,\mathrm{eV}$	$0.80\,\mathrm{eV}$
Spectral width ΔE_{phot}	$\approx 30\,\mathrm{meV}$	$25\,\mathrm{meV}$
Pulse energy	$\leq 300\,\mathrm{nJ}$	$2.8\,\mathrm{nJ}$
Average output power P_{avg}	$\leq 80\,\mathrm{mW}$	$250\,\mathrm{mW}$

Table 2.1: Specifications of the utilized laser systems.

2.5   Sample Characterization

As stated earlier in this thesis, direct and indirect semiconductors exhibit different properties in terms of the spin injection and relaxation processes. Therefore, specifics of the indirect semiconductor germanium in general, as well as the properties of the individually utilized specimen are discussed in this section.

Germanium is a group IV semiconductor, which crystallizes in the diamond-structure. The resulting centrosymmetry rules out the Dyakonov-Perel spin relaxation mechanism, as stated in chapter 1.3, and therefore shows promise in providing elevated spin lifetimes, compared to direct, III-IV and II-VI semiconductors, who commonly lack a center of inversion.

As a starting point of the characterization of the material, the band structure, as well as the relevant band gap energies of germanium at cryogenic temperatures are depicted on the left side of figure 2.6. The temperature dependence of the band gap energy at the Γ- and L-points is given by an empirical formula (Varshni-equation) according to [53]:

$$E_g = \left(0.742 - \frac{4.8 \cdot 10^{-4}\, T\,[\mathrm{K}]^{-2}}{T\,[\mathrm{K}] + 235} \right)\ \mathrm{eV} \tag{2.8}$$

$$E_\Gamma = \left(0.89 - \frac{5.82 \cdot 10^{-4}\, T\,[\mathrm{K}]^{-2}}{T\,[\mathrm{K}] + 296} \right)\ \mathrm{eV} \tag{2.9}$$

Here, T denotes the temperature in Kelvin. In the investigated range of photon energies, the refractive index of the material has comparatively high values of ≈ 4 [54].

The utilization of the RegA and OPA laser system allows the pumping and probing of the material at energies ranging from well above the direct band gap energy down to the indirect band gap. In contrast, the RSA measurements, which are carried out with the Toptica FFS, will only address states located between the direct and indirect band gap energy.

It was stated in chapter 1.1 that the excitation of electron hole pairs with photon energies $E_L < \hbar\omega < E_\Gamma$ requires a phonon scattering process to cope for the momentum mismatch. As a consequence, the absorption coefficient in this regime is notably smaller than for energies above the direct band gap energy. Therefore, all-optical experiments in transmission geometry require samples with comparatively high thicknesses in order to ensure a sufficiently high interaction length. Within the experimentally accessible spectral region given by the laser system (c.f. table 2.1), the linear absorption coefficient varies over several orders of magnitude [23, 55]. It

Sample #	Manufacturer	Surface	$n_d\,[\mathrm{cm}^{-3}]$	$\rho\,[\Omega\mathrm{cm}]$	$d\,[\mathrm{mm}]$
1	Edmund	[111]	$(6 \pm 2) \times 10^{13}$	20	1.5
2	Thorlabs	[111]	-	-	5.0
3	MT-Berlin	[100]	$\sim 2 \times 10^{13}$	58.6 ± 2.8	4.7

Table 2.2: Parameters of the utilized germanium samples. For empty cells no information was found. Sample 1 is identical to *sample B* from [25, 52]. The doping concentration n_d for sample 3 is estimated from its resistivity.

is therefore necessary to utilize Ge specimens with different thicknesses since a wide range of photon energies is applied.

A list of samples that are probed within this thesis is given in table 2.2. All utilized samples are nominally undoped, since previous work has shown that undoped Ge samples benefit spin ensemble longevity [25].

It is important to note that samples with different surface orientation can be employed. As the orientation of the external magnetic field along the crystal axes has a major influence on the appearance of the TRFR and RSA traces, the choice of specimens with different surface orientations facilitates the study of those specific dependencies. In this context, a central aspect is the fact that the effective g-factors of the electrons can be different for electrons residing in different L-valleys, which will be discussed in the following section.

g-factor anisotropy

As stated in chapter 1.1, one of the specifics of germanium is that excited conduction band electrons reside in the L-valleys. Since the curvature of the conduction band at the L-point is anisotropic in k-space, the effective mass m^* of residual carriers is a tensor with two distinct components m_l and m_t. In other terms, the surfaces of constant energy in the L-valleys are ellipsoids, as illustrated at the right hand side of Fig. 2.6. While this finding has been theoretically constituted since 1959 by Roth and Lax [57], it has but recently been focused on in all optical experiments studying electron spin decoherence [25, 52]. Given the definition of the effective g-factor as discussed in chapter 2.2, g^* also becomes a tensor and possible g^* values for the ith L-valley are determined by [58]:

$$(g_i^*)^2 = g_l^2 \cos^2(\theta_i) + g_t^2 \sin^2(\theta_i) \tag{2.10}$$

The angle θ gives the orientation of the magnetic field with respect to the half-axes of the above-mentioned ellipsoids. Following the notation of [25], the anisotropy of the
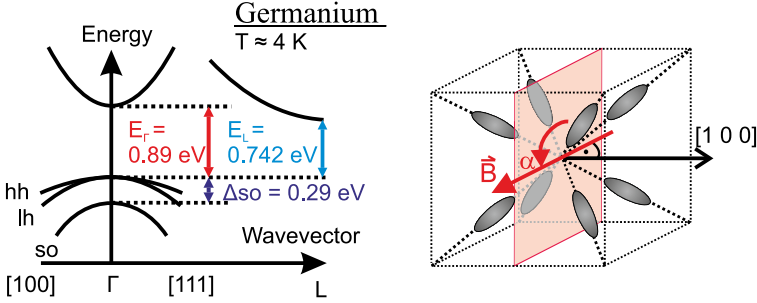
Figure 2.6: Left side: Germanium band structure at cryogenic temperatures. Values for E_Γ, E_g and Δso taken from [53, 56]. Right side: k-space diagram of surfaces of constant energies for L-valley electrons (taken from [25]). An external magnetic field is shown in real space in Voigt-geometry for a sample with [100] surface orientation.

effective g-factor can also be expressed with respect to the main crystallographic axes. To this end, the experimentally more conveniently addressable angle α is introduced, which gives the orientation of the magnetic field within the same plane as the surface of the sample, as shown on the right side of Fig. 2.6.

For the case of a sample with [100] surface orientation (i.e., the surface is oriented normal to [100]) and a magnetic field in Voigt-geometry, as seen on the right side of Fig. 2.6, there are up to two possible orientations of the magnetic field with respect to the half-axes of the ellipsoids of the different L-valleys. For a given angle α, these two angles can be calculated from the relations [25]:

$$\cos(\theta_1) = \frac{2}{\sqrt{6}}\cos(\alpha), \quad \cos(\theta_2) = -\frac{2}{\sqrt{6}}\sin(\alpha) \tag{2.11}$$

The calculated values of θ_i can then be applied to equation (2.10) in order to obtain the corresponding effective g-factors.

Analogously, for the case of a sample with [111] surface orientation and a magnetic field in Voigt-geometry, up to four different θ_i can be identified [25]:

$$\cos(\theta_1) = 0 \qquad\qquad \cos(\theta_2) = \frac{2}{\sqrt{6}}\cos(\alpha) - \frac{2}{3\sqrt{2}}\sin(\alpha)$$

$$\cos(\theta_3) = \frac{4}{3\sqrt{2}}\sin(\alpha) \qquad\qquad \cos(\theta_4) = \frac{2}{\sqrt{6}}\cos(\alpha) + \frac{2}{3\sqrt{2}}\sin(\alpha) \tag{2.12}$$

As a result, the different effective Landé-factors that follow from equations (2.10) to (2.12) allow carriers in different L-valleys to precess with individual Larmor frequencies according to equation 2.2. In figure 2.7, the resulting effective g-factors with
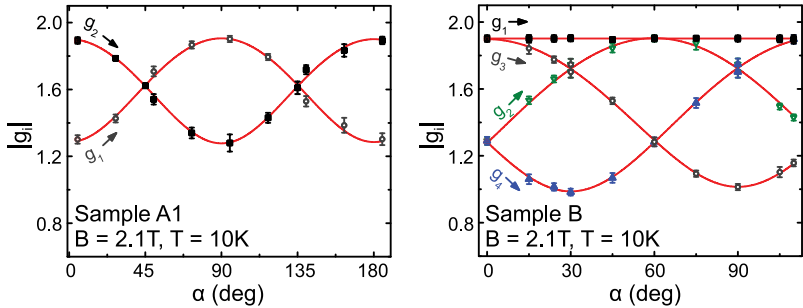
Figure 2.7: Taken from [25]: Anisotropy of the effective g-factors in germanium for a sample with [100] surface orientation (left panel) and [111] surface orientation (right panel). Symbols are experimental values taken from TRFR transients, red solid lines are fitted to the data.

respect to α are depicted for a specimen with [100]-surface orientation (sample A1 [25], left panel) and one with [111]-surface orientation (sample B [25], right panel). Due to the interplay of the different Larmor frequencies, the TRFR transients that are shown in the experimental chapters of this thesis feature beating patterns dependent on the crystal axes and the magnetic field orientation. Analogously, the RSA traces also exhibit a more complex structure than the prototypical signal depicted in figure 2.4. However, as evident from figure 2.7, experimental conditions can be found where the g-factor anisotropy is lifted and only a single effective g-factor remains for electrons in the different L-valleys.

Chapter 3

Spectral Dependence of Spin Injection and Readout

In this chapter, experimental results on the spectral dependence of the optical spin injection and readout process will be discussed. As a starting point, typical TRFR transients are shown in chapter 3.1, which represent the two distinct types of carrier spin ensembles. From these signal traces, the Faraday rotation angle θ_F is extracted in order to provide a quantitative measure for the magnitude of the spin polarization.

Throughout the investigated spectral range of 0.76 eV - 0.94 eV, the absorption coefficient of Ge varies by 5 orders of magnitude [23, 55]. This makes it intrinsically difficult to maintain the same excitation conditions in terms of the number of photoexcited carriers or their density. It is therefore instructive to normalize the FR amplitudes θ_F by the sheet density of the photoexcited carriers $n_{opt,2D}$ within the focal area of the pump beam. By repeating this measurement and evaluating the results for a set of pump and probe photon energies, it is possible to derive the spectral dependence of the combination of the spin injection and readout process.

The utilized pump and probe photon energies are identical as they are derived from the same original pulse. As a consequence of this degenerate pump probe setup, the spectral dependence of the normalized amplitudes can relate to two different effects. One effect is a spectral dependence of the spin injection, i.e., a dependence of the DSP on the the excitation energy, as discussed in chapter 1.1. The other influence would be an intrinsic spectral dependence of the Faraday Rotation amplitude or, in other terms, an energy-dependent readout process. Therefore, the injection and readout process must be discussed as a whole and individual aspects such as the injection efficiency and spectral dependence of the degree of spin polarization cannot be analyzed individually. However, under certain assumptions, the comparison of the

relative amplitudes of both carrier types makes it possible to address the observed dependencies to a spectral dependence of the spin injection process. Furthermore, investigating the ratio of θ_F of hole and electron spin ensembles for each individual measurement allows for a robust study of the relative spectral evolution of both carrier types, as a potential misalignment of the pump and probe beam overlap in each individual measurement should influence both carrier types in a similar way.

If not stated otherwise, the TRFR transients presented in this thesis depict the difference of the traces recorded with right- and left-circularly polarized pump pulses. This approach rules out the influence of slowly varying signal components that do not correspond to spin phenomena, such as heating by the pump beam irradiance or a minor misalignment of the delay stage, as these effects do not exhibit a polarization dependence. For the purpose of achieving relatively high excitation densities, as well as for the benefit of spectral tunability, all measurements in this chapter utilize the RegA and OPA laser system.

3.1   Determination of Electron and Hole Spin Faraday Rotation

In recent studies, conduction band electrons and valence band holes have been shown to precess with distinct Larmor frequencies in germanium, which correspond to effective g-factors of $|g_e^*| \approx 0.9 - 1.9$ (c.f. ch. 2.5) and $|g_h^*| \approx 5.5$, respectively [24, 25]. Furthermore, the coherence times of electrons have been reported to exceed those of holes by up to two orders of magnitude for the case of cryogenic temperatures. Due to these markedly different characteristics, it is possible to extract information of both carrier species from the same TRFR trace. A characteristic TRFR transient is depicted in figure 3.1, showing the temporal evolution of the Faraday rotation angle over the pump-probe delay time, realized by the movement of a linear motorized stage in the probe beam path.

At first, a peak arises at zero delay time, when pump and probe pulse overlap temporally, likely caused by two-photon absorption (not shown in figure 3.1). After the initial peak has decayed, a pronounced precession can be observed, which corresponds to the hole spin ensemble. Shown as a red solid line, this data component can be fitted with a function of the form:

$$\theta_h(\tau) = A_1 \exp\left(-\frac{\tau - \tau_0}{T}\right) + A_h \exp\left(-\frac{\tau}{T_{2,h}^*}\right) \sin\left(\frac{2\pi(\tau - \tau_c)}{\omega_{L,h}}\right) + y_0 \qquad (3.1)$$
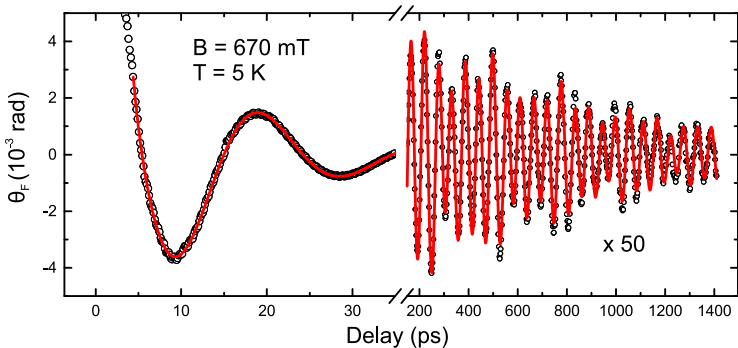
Figure 3.1: A characteristic TRFR transient illustrating the Faraday rotation angle θ_F with respect to the pump-probe delay for an external magnetic field of $B = 670\,\text{mT}$ at $T = 5\,\text{K}$. The signal corresponding to the hole spin polarization relaxes on time scales of $\sim 20\,\text{ps}$, whereas electron spin traces are persistent on time scales of $\sim 1\,\text{ns}$ (please note different axis scale and break). The red solid lines are fit to the data according to Eq. (3.1) and (3.2), respectively. The much smaller signal, which corresponds to the electron spin ensemble, is multiplied by a factor of 50 for better visibility.

In this formula, τ denotes the pump-probe delay, τ_0 is the overlap point in time of pump and probe, and y_0 is a background offset. The time τ_c takes into account that hole spin ensemble starts to precess at a slightly delayed time after the excitation, which could be related to a fast thermalization of the charge carriers.

The first summand in equation (3.1) accounts for the above-mentioned quickly decaying two-photon peak, which is present during the time interval where pump and probe overlap due to their finite pulse duration. The second summand allows the identification of the hole spin coherence time $T_{2,h}^*$, the corresponding Larmor precession frequency $\omega_{L,h}$, and the amplitude factor A_h. The value of A_h characterizes the amplitude of the spin polarization and can be employed as a measure of the Faraday rotation signal for the respective underlying experimental conditions.

After the hole spin polarization has dephased on typical time scales of $\sim 20\,\text{ps}$, a much more persistent Larmor precession signal becomes apparent, which can be addressed to the electron spin ensemble due to its characteristic beating pattern that features various g-factors in the range of $\approx 0.9 - 1.9$. The signal that corresponds to the electron spins is multiplied by a factor of 50 in figure 3.1 for better visibility.

Analogous to equation (3.1), the electron spin precession signal can be fitted according to:

$$\theta_e(\tau) = A \exp\left(-\frac{\tau}{T}\right) + \sum_{i=1}^{4}\left[A_i \exp\left(-\frac{\tau}{T_{2,e}^*}\right)\sin\left(\frac{2\pi(\tau - \tau_c)}{\omega_{L,e,i}}\right)\right] + y_0 \qquad (3.2)$$

In this formula, the first summand incorporates any residual slowly varying background signal that might superimpose the Larmor precession signal. Taking into account the different effective g-factors, a series of exponentially decaying sine functions is fitted to the data in the case of electrons. The sum of the individual Larmor precession amplitudes A_i can then be used to quantify the signal strength of the corresponding TRFR trace for the given excitation and readout conditions.

The experimental study that will be presented in the following founds on the extraction of the amplitudes of the Faraday rotation signals for the respective carrier type, according to equation. (3.1) and (3.2). More specifically, the amplitudes obtained from TRFR traces recorded with different central photon energies of the pump and probe pulses are compared in order to study the spectral dependence of the spin injection and readout efficiency in germanium.

3.2   Excitation Conditions

To clarify the excitation conditions used for the present study, Fig. 3.2 depicts the intensity spectra of the pump and probe pulses as colored, solid lines (left axis) that are used to optically excite and read out the TRFR signals in the context of this chapter. The tuning of the central photon energy is achieved by tuning the output of the OPA. Not all spectra within the applicable range of pump and probe beam photon energies are shown for clarity.

As evident from the indirect band gap energy (E_{L}) and direct band gap energy (E_Γ) of germanium, indicated by dashed lines in Fig. 3.2, excitation and readout photon energies can be tuned from close to E_{L} to energies that exceed the direct band gap E_Γ by up to $60\,\mathrm{meV}$. The spectral widths of the beams range from $\approx 20\,\mathrm{meV}$ for the lowest central photon energy to $\approx 40\,\mathrm{meV}$ for the higher energy boundary.

In addition to the spectra, Fig. 3.2 features the excitation densities that are applied in the complete data set used for the study of the spectral dependence that will be presented in this chapter. In particular, for a given central photon energy on the x-axis, the black triangles indicate the corresponding excitation density with respect to the y-axis on the right hand side of the plot. Each triangle corresponds to one TRFR trace from which the electron and hole spin amplitude can be extracted.
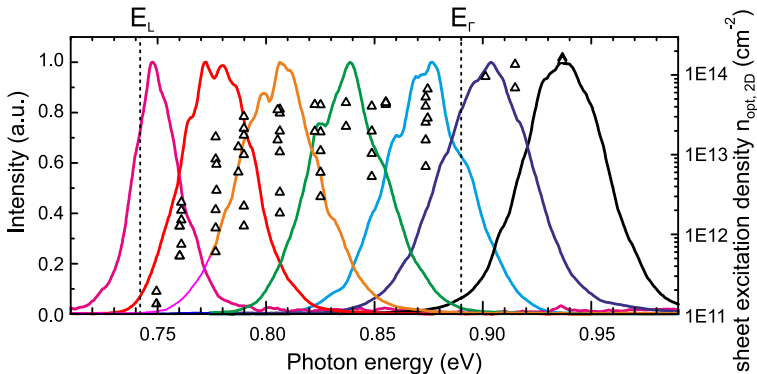
Figure 3.2: Intensity spectra of the pump pulses utilized to investigate the spectral dependence of spin injection and readout, shown as colored solid lines (left y-axis). Not all spectra of the applied pump beams are shown for clarity. The black, open triangles show the correspondingly induced 2D excitation densities (right y-axis, logarithmic scale). The dashed lines mark the indirect (E_L) and direct band gap energy (E_Γ).

However, for identical photon energies the data points will be shown as averaged over the various applied excitation densities for the discussion of spin injection and readout efficiency in the following sections.

The sheet excitation density is chosen over the conventionally addressed 3D optical excitation density in this case in order to compare the results for samples of different thicknesses. The sheet excitation density is calculated by multiplying n_{opt} with the sample thickness: $n_{opt,2D} = dn_{opt}$.

The average 3D excitation density n_{opt} is numerically calculated for each pump spectrum as an average of the induced charge carriers over the volume of a cylinder[1], which is defined by the beam path across the sample. The spectra are therein considered to be Gaussian distributions and only linear absorption is taken into account. As the OPA output is strongly dependent on the output wavelength, the maximum power of the pump beam in front of the sample that corresponds to the optical densities shown in Fig. 3.2 ranges from $\approx 1.9\,\text{mW}$ in the lower energy tail up to $\approx 4\,\text{mW}$ for the highest photon energies.

---

[1]The approximation of a cylinder instead of a Gaussian profile along the direction of propagation is justified by the high values of the refractive index inside the material of ≥ 4 [54], greatly reducing the angle of incidence and the focusing inside the material.

Earlier in this thesis it has already been stated that the linear absorption coefficient α is significantly lowered for indirect transitions with $\Delta k \neq 0$, since a phonon scattering event has to occur [23, 55]. Consequently, the achievable excitation density for a given thickness of the germanium specimen and a given average power of the pump beam spans over several orders of magnitude within the range of applicable photon energies, as seen in Fig. 3.2. In detail, the maximum excitation density amounts to $n_{\text{opt,2D}} = 1.9 \times 10^{11}\,\text{cm}^{-2}$ for the lowest photon energy of $0.75\,\text{eV}$ and goes up to $n_{\text{opt,2D}} = 1.7 \times 10^{14}\,\text{cm}^{-2}$ for the highest photon energy of $0.94\,\text{eV}$.

3.3 Spectral Dependence of Electron and Hole Spin Amplitudes

So far, this chapter has outlined how the amplitudes of the spin polarization can be gauged from the observed Faraday rotation transients and what excitation conditions are applicable within this study. In the following sections of this chapter, experimental results on the obtained FR amplitudes are presented that allow to draw conclusions on the spin injection and readout process for the individual carrier types.

The investigation of the spectral dependence of the Faraday rotation amplitudes of hole and electron spins founds on a data set of TRFR transients for the series of degenerate pump and probe energies shown in figure 3.2. The data are taken at temperatures of $T = 6\,\text{K}$ to ensure a relatively high spin coherence time. The highest applicable magnetic field strength of $B = 0.67\,\text{T}$ is chosen for the study to induce a sufficient amount of Larmor precession cycles for the hole and electron spin ensembles in order to provide robust results from the fit.

Traces of the Larmor precession of the respective spin ensembles are obtained for pump and probe energies ranging from $0.76\,\text{eV}$ to $0.94\,\text{eV}$. In this region, a pronounced spectral dependence of the spin injection and readout process is expected because the interband transition to different energy levels at the L-valley causes a variable number of electron-phonon-scattering events to be necessary in the thermalization process of the electrons to the minimum of the band.

For a given photon energy, transients are recorded for pump powers ranging from the maximum applicable power down to where the signal-to-noise ratio vanishes. The measurements for different excitation powers and their corresponding excitation densities at fixed photon energies were originally performed to also investigate possible dependencies of the g-factor and spin coherence times on the carrier density

(data not shown). However, the amplitude of the spin signal is not dependent on the carrier density but on the total amount of spin-carriers. Therefore, the study benefits from the data set taken for different excitation powers at a given photon energy as these data points can be averaged over, which increases the reliability of the experimental results.

From each transient of the above-mentioned data set, the hole and electron spin amplitude is obtained by fitting the experimental values with functions of the form of (3.1) and (3.2), respectively.

The outlined experiment is carried out in two different germanium samples (sample 1 and sample 2, c.f. 2.2) with thicknesses of 1.5 mm and 5 mm, respectively. The choice of specimens with different thicknesses is motivated by the fact that the different thicknesses allow to extent the range of examinable photon energies for the study: A sample with high thickness is beneficial for the investigation of the spin signals at energies close to the indirect band gap, as the higher thickness counteracts the vanishing absorption coefficient in terms of the total amount of injected spin carriers and the corresponding signal strength. On the other hand, the choice of a thinner sample enables the use of higher photon energies, as it allows a sufficient amount of probe light to pass through the sample for the correspondingly increasing absorption, which is needed to obtain a reliable signal. The comparability of the results obtained from the individual specimen is achieved by normalizing the obtained FR amplitudes on the total amount of induced charge carriers, i.e., on the optical sheet density.

Holes

Starting with the experimental results on the hole spin ensemble, figure 3.3 depicts the values for the Faraday rotation amplitudes $\theta_{F,h}$ normalized on the photoexcited sheet density for the previously outlined range of excitation conditions. Due to this normalization, the depicted values represent the TRFR signal strengths that result from a single photoexcited carrier for a normalized sample thickness of 1 cm.

The data points shown in Fig. 3.3 consist of mean values of $\theta_{F,h}$ for the respective applicable range of excitation densities. Furthermore, error bars are depicted, which represent the standard deviation of the mean values. The uncertainty of the amplitudes points towards a slight misalignment of the pump and probe overlap when the pump power is adjusted. This explanation stands in good agreement with the fact that the standard deviation on average has a higher value in the thicker sample, where misalignment is more critical due to the higher interaction length.
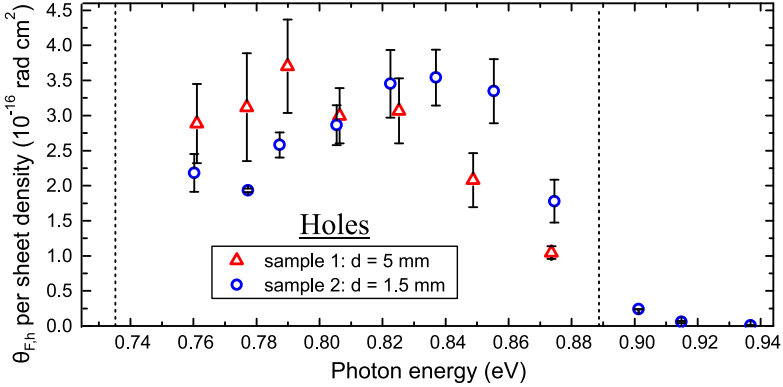
Figure 3.3: Hole spin ensemble Faraday rotation amplitudes normalized on the photoexcited sheet density dependent on the central photon energy of the utilized pump and probe photon energies as shown in Fig. 3.2. The red triangles and blue circles represent data points taken for the samples with 5 mm and 1.5 mm thickness, respectively. Data points are mean values derived from multiple measurements with different excitation densities. Error bars represent the standard deviation of the mean values. Dashed lines mark the energetic position of the indirect and direct band gap energy.

Moreover, the error bars tend to decrease for increasing photon energies where the total amount of photoexcited holes and therefore also the signal-to-noise level is higher (c.f. Fig. 3.2).

Starting the discussion of the data from the lower photon energy boundary, the normalized Faraday rotation angle shows values of $\approx 2.5 \times 10^{-16}$ rad cm^2 for photon energies as low as 0.76 eV. Between 0.76 eV and 0.85 eV, no clear, significant overall trend of the normalized hole spin amplitudes can be observed for sample 1. In the same energetic region, sample 2 exhibits a slight increase of the normalized hole spin Faraday rotation from values of $\sim 2 \times 10^{-16}$ rad cm^2 to $\sim 3 \times 10^{-16}$ rad cm^2.

Moving towards the direct band gap energy of 0.89 eV, the normalized amplitudes slowly decrease for both samples. As the photon energies exceed 0.85 eV, the hole spin amplitudes markedly drop by 1-2 orders of magnitude. For excitation solely across the direct band gap, hole spin signatures are hard to resolve at all. As mentioned above, for photon energies above the direct band gap, the carrier densities are substantially larger than for the excitation across the indirect band gap. However, variations of the excitation density typically reveal no influence on

the normalized Faraday rotation angle but only on the hole spin coherence time. Thus, the elevated carrier densities are likely not the cause of the signal decrease in Fig. 3.3.

Electrons

The presently discussed efficiency of the electron spin injection and read out can be expected to be influenced by the orientations of the applied electromagnetic and magnetic fields with respect to the side valleys that contain the persistent spin-oriented electrons. In other terms, it is thinkable that the injection and readout process is more efficient for certain in-plane orientations of the sample. In order to examine this issue, the two samples studied in this chapter are probed with different orientations that correspond to characteristically different configurations of the L-valleys, which will now be described in more detail.

For sample 1, an orientation of $\alpha \approx 15°$ is chosen (c.f. Chap. 2.5). The TRFR traces that result for this configuration reveal 3 different effective g-factors of $g_{1,2,3}^* = 1.91, 1.53, 1.08$. It is insightful to note that, in principle, four different values for g^* should be present, with the missing value being $g_4^* = 1.87$. However, due to the temporal limitation of the TRFR traces, the different peaks in the FFT amplitude are too wide, such that the peak at $g^* = 1.91$ and $g^* = 1.87$ cannot be distinguished. Correspondingly, for the purpose of mapping the sum of the amplitudes $\sum_i A_i$ (c.f. Eq. (3.2)) that are required for the study of the spin injection and readout efficiency, the fit is sufficiently robust to whether 3 or 4 different g-factors are used.

For the case of sample 2, a markedly different orientation of $\alpha \approx 0°$ is chosen, which corresponds to the case where only two effective g-factors can be deduced from the TRFR transients, which read $g_{1,2}^* = 1.92, 1.29$.

In close relation to the previous section, the spectral dependence of the electron spin amplitudes is now examined in more detail. Analogous to Fig. 3.3, the normalized electron spin ensemble Faraday rotation amplitudes $\theta_{F,e}$ are depicted in figure 3.4. The amplitudes originate from the same Faraday rotation data set as utilized for the discussion of hole spins. Accounting for the different g-factors involved in the electron signals, the data points are the sum of the amplitudes of the respective Larmor precession signals in this case, i.e., $\theta_{F,e} = \sum_i A_i$, according to Eq. (3.2).

Contrary to the results on the hole spin amplitudes, a significant electron spin polarization for excitation with photon energies above the direct band gap energy can be observed. However, the normalized amplitudes are significantly higher for
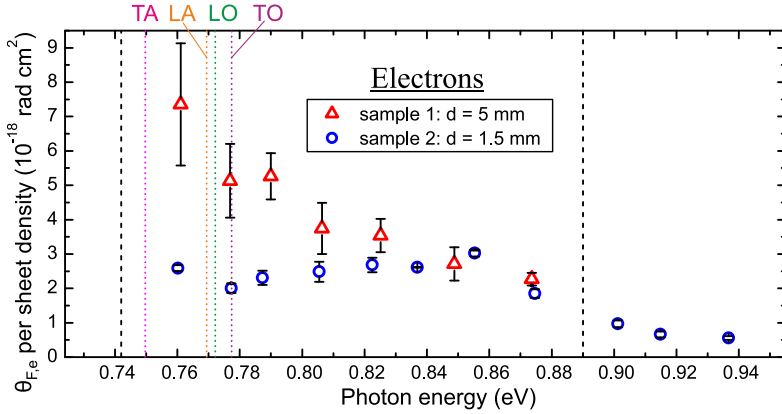
Figure 3.4: Sum of the electron spin ensemble Faraday rotation amplitudes $\theta_{\mathrm{F,e}} = \sum_i A_i$ normalized on the photoexcited sheet density. Amplitudes originate from the same Faraday rotation data set as used for the hole spins in Fig. 3.3. The red triangles and blue circles represent data points taken for the samples with 5 mm and 1.5 mm thickness, respectively. Data points are mean values derived from multiple measurements with different excitation densities. Error bars represent the standard deviation of the mean values. Black dashed lines mark the energetic position of the indirect and direct band gap energy. Colored, dotted lines mark the energetic displacement of a single phonon energy from the indirect band gap.

pump photon energies below the direct band gap energy. In the case of the 5 mm sample, a more pronounced general trend of higher amplitudes for lower photon energies is observable. In contrast, no such general trend is seen for photon energies between the direct and indirect band gap in the case of the 1.5 mm sample.

For the signal amplitudes between 0.78 eV and the indirect band gap energy, a slight enhancement is seen for both samples. In line with theoretical predictions presented in [27], this finding can be explained by the fact that phonon scattering events exhibit a certain probability of a spin-flip. Thus, a multitude of scattering events in the injection process can lead to a reduction of the DSP [27].

For different types of phonons, the displacements of a single phonon energy from the indirect band gap are shown as colored, dotted lines in Fig. 3.4. The values cor-

respond to the phonon branches at the L-point, as reported in [59][2]. Ultimately, in the regime where only a single phonon energy can contribute to the carrier injection over the indirect band gap, only one scattering event occurs, and the obtained value of the normalized $\theta_{\mathrm{F,e}}$ is enhanced for both samples.

The fact that this enhancement cannot be seen for the data points at $\sim 0.78\,\mathrm{eV}$ might be related to the relatively high spectral width of the utilized pulses of $\approx 20\,\mathrm{meV}$, which smears out the effect. This assumption is substantiated by the fact that the majority of the carriers is optically excited by the higher photon energy fraction of the pulses due to the steep spectral dependence of the absorption coefficient.

Relative Amplitudes of Electrons and Holes

While certain precautions can be met to keep the pump and probe overlap stable when varying the photon energies via tuning the OPA output, it is impossible to guarantee that the overlap does not change over the full length of the sample. Even for perfectly realigned beams within the setup, effects like, e.g., the dispersion of the lens in front of the cryostat can alter the exact overlap of the pump and probe spots. It is therefore instructive to analyze the ratio of the electron and hole spin amplitudes. This approach can be justified by the fact that a misalignment of the pump and probe overlap can be expected to have a similar impact on the amplitudes of both carrier types, especially because the excitation densities are comparatively low, ruling out saturation effects or screening by surrounding carriers.

In Fig. 3.5, the ratio of the detected FR amplitudes of electrons and holes is shown, which have been presented in Fig. 3.4 and Fig. 3.3, respectively. The data plot is shown only for photon energies below the direct band gap because of the vanishing hole spin signal in the regime of $\hbar\omega > 0.89\,\mathrm{eV}$. Moreover, the data points at $0.875\,\mathrm{eV}$ photon energy are already largely affected by the decreasing hole spin signal, explaining the increase in $\theta_{\mathrm{F,e}}/\theta_{\mathrm{F,h}}$ for elevated photon energies.

As expected, the analysis of the ratio of electron and hole spin amplitudes is found to be more stable, as evident from the on average smaller error bars [3].

---

[2]In this reference, the values of the phonon energies are given for a temperature of $T = 80\,\mathrm{K}$. However, as the crystal lattice does not drastically change with temperature in the region of $80\,\mathrm{K}$ to $5\,\mathrm{K}$ [60], the phonon energies can be estimated to be equal for the present temperatures.

[3]The error bars represent the deviation of the particular values of $\theta_{\mathrm{F,e}}/\theta_{\mathrm{F,h}}$ within the data subsets for equal photon energies and are not calculated by means of error propagation from the individual values of holes and electrons.
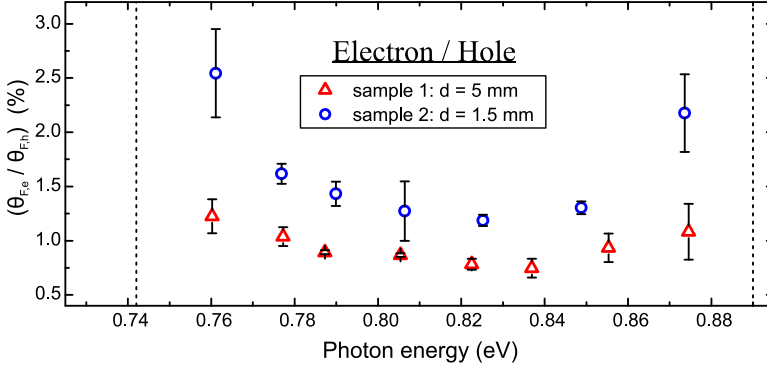
Figure 3.5: Ratio of the Faraday rotation amplitudes of the electron and hole spin amplitudes shown in Fig. 3.4 and 3.3, respectively.

Strikingly, a pronounced increase of the electron to hole ratio towards the indirect band gap can be seen. It is to be expected that the ratio of electron and hole spin signals does not intrinsically depend on the actual probe photon energy. This can be understood by recalling the fact that every photoexcited electron in the conduction band accounts for one hole in the valence band. Moreover, the carrier types represent the initial and the final state of the same transition. Therefore, pump-induced changes to this transition should alter the probe beam in the same way for both carrier types. Ultimately, it is reasonable to assume that the observed enhancement is caused by an increase of the degree of electron spin polarization due to a more efficient spin injection close to the indirect band gap rather than an energy-dependent readout process.

3.4   Discussion and Outlook

The experimental results presented in this chapter provide insight into the spectral dependence of the efficiency of all-optical manipulation of spins in the indirect semiconductor germanium by comparing normalized Faraday rotation amplitudes of electron and hole spin ensembles obtained with different degenerate pump-probe photon energies.

For the case of holes, the experimental study shows that no significant spin polarization can be resolved for photon energies well above the direct band gap

energy. This finding stands in contrast with theoretical predictions for the degree of spin polarization for excitation with $\hbar\omega \geq E_\Gamma$, given by [34]. In particular, the calculated values report a maximum DSP of holes at photon energies of $\hbar\omega = E_\Gamma$ with a value of $\text{DSP}_h = 80\,\%$. A theoretical explanation for this contradiction has not been found to date. Previously reported experimental results on the degree of spin polarization for optical orientation with photon energies above the direct band gap energy point to similar deviations from the theoretical value at the Γ-point [40]. However, these results are strongly influenced by deviations of the excitation profile that result from excitation with different photon energies.

Interestingly, the present thesis shows that results obtained from samples with different in-plane orientations deviate from each other for the case of hole spins. Moreover, no clear spectral dependence can be deduced for the energetic region between the indirect and the direct band gap energy. As the observed hole spin signals are expected to arise from holes located at the highly symmetric Γ-point, the deviations seen for samples with different in-plane orientations are intuitively not expected. As no information is provided for the residual doping concentration of the nominally undoped sample 2, the observed distinctions might result from different doping concentrations or dopants.

The experimental results obtained from the Faraday rotation traces that correspond to the electron ensembles' Larmor precession show a marked overall dependence on the utilized pump and probe photon energies with a trend of increasing Faraday rotation amplitudes for decreasing photon energies. In this context, indications are found that support the theoretical prediction given by [27], which states that the degree of spin polarization of the electrons increases for a decreasing total amount of phonon scattering events that the electrons undergo until they reside in the L-valleys. In line with the explanations given in [40], the utilization of photon energies above the direct band gap energy appears to reduce the electron DSP, which can be explained by the additional scattering from the Γ-point to the L-valley.

While the exact values of the degree of spin polarization cannot be quantified within the experiments outlined above, the spectral trend should be resembled by the data. Based on radio frequency measurements, recent experiments by C. Guite and V. Venkataraman report the electron DSP in Germanium to be $4.8\,\%$ for excitation with photon energies of $0.9239\,\text{eV}$ [61]. In order to integrate this result into the data shown in this chapter, it is instructive to compare values for the normalized electron Faraday amplitudes for the sample with $d = 1.5\,\text{mm}$ shown in Fig. 3.4. The datapoint closest to the value reported in [61] is located at $0.915\,\text{eV}$ with a corresponding value of $\theta_{\text{F,e}} = 0.663 \times 10^{-18}\,\text{rad}\,\text{cm}^2$. The datapoint in closest proximity

to the indirect bandgap reads $0.760\,\mathrm{eV}$ and $\theta_{\mathrm{F,e}} = 2.59 \times 10^{-18}\,\mathrm{rad\,cm^2}$. Assuming a DSP of $4.8\,\%$ for $0.915\,\mathrm{eV}$, the DSP at $0.760\,\mathrm{eV}$ would be $18.8\,\%$. This value lies in good agreement with the theoretical prediction given for silicon in [27], where the maximum DSP reaches $25\,\%$ for photon energies equal to the indirect band gap energy.

As another central result of the study, the experimental data reveals a pronounced dependence of the electron spin Faraday rotation signal on the in-plane orientation of the sample and/or their doping concentrations. Strikingly, the spectral dependencies subside when the relative amplitudes of electrons and holes are compared, and the observed spectral trends tend to be rather uniform for both samples. Thus, the results obtained from the presented study indicate the need for a more systematic study on the dependence of the spin injection and readout efficiency on the sample geometry and the doping concentration as a guideline for future experiments.

From a physics point of view, a more elaborate analysis of the dependence of the sample orientation on the spin injection and readout efficiency would be interesting, as it would allow to take a closer look at the relative amplitudes of the individual electron Larmor precession signals that originate from the different L-valleys. Studying how the carriers in the individual L-valley contribute to the overall signal would greatly help to expand the understanding of the spin injection process in indirect semiconductors and should therefore be a central aspect of ongoing experimental investigations.

As stated before, the presented spectral dependencies can originate either from an energy-dependent spin injection or detection efficiency. To distinguish between both effects, the measurements would have to be performed with a fixed probe and variable pump pulse to solely detect the influence of spin injection efficiency, or vice versa to isolate the effect of an energy-dependent detection. The latter originates from the sensitivity of the Faraday Rotation amplitude on the spectral detuning between the probe pulse and the energy of the states occupied by the spin carriers, i.e., on the exact spectral behavior of the dielectric tensor (c.f. Chap. 1.2). This effect is well understood for the case of resonant absorption and has also been experimentally verified in quantum dot ensembles [62], as well as in bulk GaAs [63]. For more complex spectral dependencies of the absorption coefficient, such as in indirect bulk semiconductors, the theoretical prediction is more difficult and, to best knowledge, no work has been presented on that matter to date. However, following the assumptions made in this chapter, the observed trends can be addressed to the

efficiency of the injection process and to an increase in the DSP for injection close to the indirect band gap.

Besides the above-mentioned proposal to perform the study with a non-degenerate pump-probe setup, future work should aim towards utilizing sharper pump and probe spectra in order to increase the spectral resolution for the study of the increase of the DSP in the vicinity of the indirect band gap. However, due to the time-bandwidth product limitation an increase of the spectral resolution requires significantly longer pulse durations. As the temporal resolution of the performed measurements is not crucial as long as the hole spin precession can be traced, a factor of 10 in pulse width would be manageable. An ideal improvement of the setup would be the utilization of a laser system that delivers picosecond high energy pulses at $0.8\,\text{eV}$. With the help of supercontinuum generation [64], it would then be possible to map the spectral region of interest, while the pump and probe photon energies could be tuned individually, e.g., by tunable band pass filters.

Chapter 4

Resonant Spin Amplification and Electron Spin Lifetimes

Earlier in this thesis, it was already stated that due to certain scattering processes inherent to a semiconductor environment, an optically oriented spin ensemble will revert to its initial, thermal distribution. The time scales on which this process occurs have been defined in chapter 1.3.

As theoretical work predicts elevated spin lifetimes up to several microseconds for germanium at low temperatures [26], it is presumable that suitable Ge specimen can be tailored to possess spin lifetimes that exceed the previously observed spin lifetimes of several nanoseconds [24, 25, 61, 65]. For the present experimental study, commercially available, nominally undoped germanium samples are used. Most importantly, germanium specimens of relatively high purity of 1 ppm can be utilized, which are expected to exhibit elevated spin lifetimes as the effect of impurity scattering can be expected to be reduced in this case.

Indeed, elevated spin ensemble coherence times can be found for these samples, where the TRFR trace does not significantly relax on the whole available range of the linear delay stage utilized in the previous experimental setup.

In the upper panel of Fig. 4.1, an electron spin TRFR transient is shown that is obtained with the RegA and OPA Laser system for a 2.5 mm sample with [111] surface orientation (provided by MTI Corporation, not listed in 2.2) for a sample temperature of $T = 8\,\mathrm{K}$ and an external magnetic field in Voigt geometry of $B = 660\,\mathrm{mT}$. It is evident from the data that besides the apparent beating pattern no significant decrease of the signal amplitude can be seen on the available time frame. Consequently, the spin coherence time cannot be properly extracted from this TRFR

trace. Hence, at this point, it is instructive to conduct the measurements based on the resonant spin amplification scheme (cf. Chap. 2.3).

As the laser system that has been utilized so far provides a comparatively low repetition rate of $f_{\rm rep} = 250\,{\rm kHz}$, spin coherence times would have to be on the order of microseconds to allow for the observation of RSA. In that case, a spin polarization excited by a pump pulse would persist until the next pulse of the cycle hits the sample, which would lead to an observable signal for nominally negative delay times. However, these extremely high coherence times are not present, as no such signal is observed for $\tau < 0$ (corresponding data not shown in Fig. 4.1, upper panel).

For the same experimental conditions, the electron spin TRFR trace is now recorded with the FFS fiber laser system, which delivers a pulse train with $f_{\rm rep} = 90.5\,{\rm MHz}$, corresponding to a pulse repetition period of $T_{\rm rep} = 11.05\,{\rm ns}$. As can be seen from the lower panel in figure 4.1, a persistent Larmor precession can be observed for negative delay times in this case.

Obviously, the signal recorded with the OPA appears to be much better in terms of signal-to-noise ratio, which can be mainly addressed to two issues. Firstly, the already very low optical excitation density is further decreased, as the higher average power of the fiber laser does not make up for the much higher repetition rate. Consequently, the average power per pulse is decreased, which leads to a reduction of the signal strength (note the different scales between the upper and lower panel in figure 4.1). Secondly, as pointed out in chapter 2.3, small fluctuations in the magnetic field strength can shift the spin polarization in and out of resonance, which increases the noise level for TRFR traces when the system is already in the RSA regime.

For clarity, both signals shown in Fig. 4.1 are offset to have their baseline at zero. The reason for a residual non-zero offset in a difference signal of right- and left-circularly polarized pump is most likely caused by an imperfect orientation of the quarter-wave plate that leads to an imperfect circular polarization of the pump beam.

In the following sections, the spin lifetimes and coherence times derived from RSA data are discussed in further detail. In this context, sample 3 of table 2.2 is utilized[1], as it exhibits the highest spin lifetimes observed in the scope of the ex-

---

[1]Due to the difficulties of the TRFR measurement scheme for highly elevated spin coherence times, no TRFR traces of this sample could be recorded with the OPA laser. Therefore, the differences that result from the utilization of the different laser systems were discussed with the aid of the otherwise not mentioned 2.5 mm sample, provided by MTI Corporation.
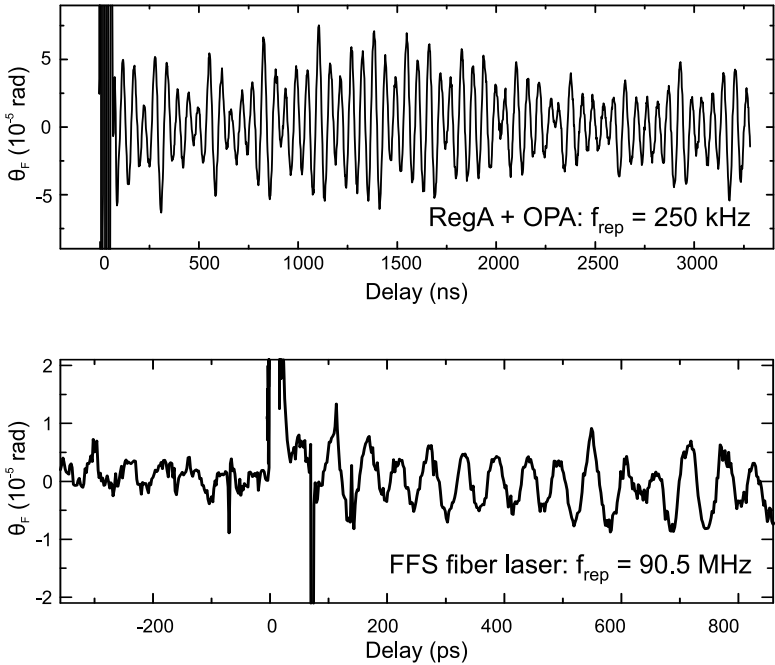
Figure 4.1: TRFR traces of the electron spin ensemble's Larmor precession in a 2.5 mm sample with [111] surface orientation, an external magnetic field of $B = 660$ mT, and a temperature of $T = 8$ K. Both signals are recorded with a degenerate pump-probe configuration with photon energies of 0.8 eV, corresponding to wavelengths of 1550 nm. The data are obtained with the Coherent RegA and OPA laser system (upper panel) and the FFS fiber laser (lower panel). Graphs are offset for clarity.

perimental study. In addition, the [100] surface orientation allows for the reduction of the number of different g-factors to a point where only one effective g-factor is present. It will be shown in chapter 4.3 that this circumstance greatly simplifies the interpretation of the resonant spin amplification signals. Furthermore, the comparatively high sample thickness of 4.7 mm facilitates a better signal-to-noise ratio at the fixed pump and probe photon energy of 0.8 eV. If not stated otherwise, the experiments shown in the following chapters use the Toptica FFS fiber laser system and magnetic fields in Voigt geometry.

4.1   Spin Lifetimes

In order to investigate the highly elevated spin lifetimes, now, the RSA traces are recorded instead of the time-resolved Faraday rotation. To do so, the Faraday rotation angle is measured at a fixed negative delay of $\Delta t = -15\,\text{ps}$ while sweeping the magnetic field. Such an RSA trace is shown in figure 4.2 with the experimental data for the 4.7 mm sample with [100] surface orientation shown as a black solid line.

As mentioned earlier, the highly symmetric [100] sample determines the amount of different values of g^* for the different L-valley electrons to be at most two. The magnetic field is applied in pure Voigt geometry, and the in-plane orientation of the sample is chosen such that only one effective g-factor remains, resembling the case of $\alpha = 45°$ (c.f. Fig. 2.7). In other terms, the magnetic field is aligned along the [010] axis of the crystal, which hereafter will be denoted as $\beta = 0°$. Later in this chapter, the dependence of the exact orientation of the magnetic field will be discussed in more detail.

The RSA trace depicted in figure 4.2 shows a spacing of $\Delta B = 3.98\,\text{mT}$. This value corresponds to an effective g-factor of $g^* = 1.62$ derived from Eq. (2.5), in agreement with the predicted value (c.f. Chap. 2.5). The red solid line in Fig. 4.2 is a fit to the data according to Eq. (2.7). As explained in chapter 2.3, a fit of this form permits the investigation the effective g-factors inherent in the RSA trace, but is insufficient to investigate the spin lifetimes or coherence times from each peak due to their dependence on the magnetic field. Instead, each peak has to be fitted separately with a Lorentzian peak function for such an analysis.

In the data shown in Fig. 4.2, the width of the central resonance peak around $B = 0$ yields a spin lifetime of $T_s \approx 28\,\text{ns}$ according to Eq. (2.6). This value is already much higher than lifetimes that have been reported in previous, all-optical studies in germanium [25].
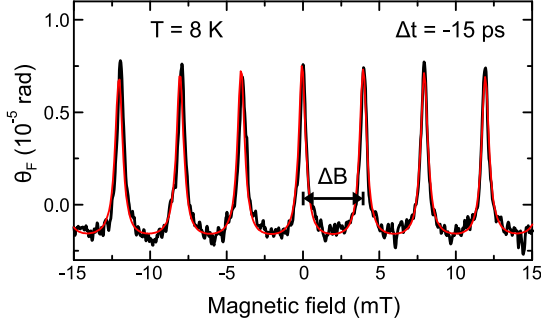
Figure 4.2: FR at a fixed negative delay of $\Delta t = -15\,\text{ps}$ for a variable magnetic field between $-15\,\text{mT}$ and $15\,\text{mT}$. The 4.7 mm thick, [100]-oriented Ge sample is kept at a temperature of T = 8 K. The red solid line is a fit to the data according to Eq. (2.7) with an effective g-factor of $g^* = 1.62$. A slowly varying background fluctuation is subtracted from the data with the help of a FFT high pass.

As stated in Chap. 1.3, the widths of RSA peaks that occur at different magnetic fields are related to different relaxation mechanisms. The peak around zero magnetic field is insensitive to decoherence effects such that its width points to the spin lifetime T_s. For resonance peaks with $B \neq 0$ (in the following denoted as *side peaks*) spin ensemble decoherence must be taken into account and the width is consequently determined by the decoherence time T_2. As the study is insensitive to whether or not the spin ensemble undergoes a reversible dephasing, the time constant T_2^* will be addressed in the context of this chapter (c.f. Chap. 1.3).

Since the scattering mechanisms that lead to spin dephasing and relaxation generally possess a marked temperature dependence [33], it is to be expected that the spin lifetimes feature a strong dependence on the temperature, as well.

Compared to conventional TRFR measurements, a major improvement of the detection of spin lifetimes with the RSA technique lies in the fact that the data acquisition time is significantly reduced. Hence, it is possible to continuously detect the spin lifetime of the system by rapidly scanning a single peak. When this rapid scanning is performed while heating up the cryostat, this technique permits to evaluate the temperature dependence of the spin lifetimes for temperatures ranging from $T \approx 6\,\text{K}$ up to room temperature (or beyond, if an active heating is applied).
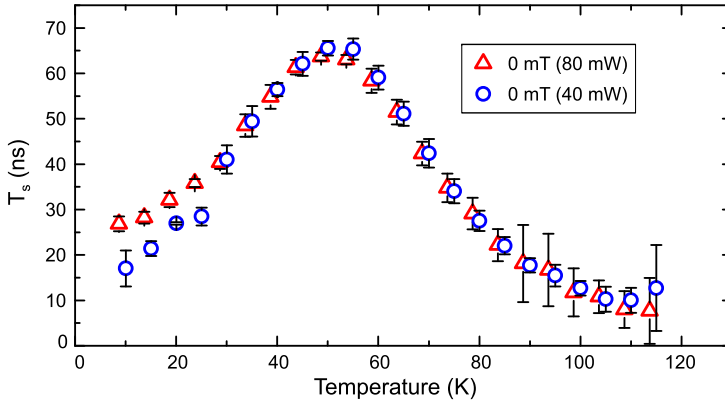
Figure 4.3: Temperature dependence of the electron spin lifetime T_s for zero magnetic field. The data are extracted from fits to individual RSA peaks such as the ones shown in Fig 4.2. Error bars represent the standard deviation of measurements within a temperature interval of $\Delta T = 5K$. The results for T_s are compared between two different excitation levels of 80 mW (red triangles) and 40 mW (blue circles).

In particular, this permits the detection of spin lifetimes in regions of $T \approx 50\,\mathrm{K}$ to $T \approx 297\,\mathrm{K}$ where it is usually difficult to operate a flow cryostat in a stable working state.

It is worth mentioning that the magnetic field amplitudes that are required for the RSA technique are somewhat lower compared to the TRFR measurements, as evident from the data seen in Fig. 4.2. However, in order to resolve the resonance peaks, the power supply of the electromagnet needs to have a higher precision.

In figure 4.3, the temperature dependence of the electron spin lifetimes is shown for two different pump powers of 80 mW and 40 mW, corresponding to densities of optically excited carriers of $5.6 \times 10^{12}\,\mathrm{cm^{-3}}$ and $2.8 \times 10^{12}\,\mathrm{cm^{-3}}$, respectively. Or, to put the carrier densities in context with the previous chapter, sheet excitation densities of $2.6 \times 10^{12}\,\mathrm{cm^{-2}}$ and $1.3 \times 10^{12}\,\mathrm{cm^{-2}}$.

For better visibility, the data taken from the numerous rapidly scanned RSA peaks is binned in intervals of 5 K, with the error bars representing the standard deviation of the respective bin[2].

---

[2]The initial x-value of the temperature within the cryostat differs for both data sets, which explains the different onset on the x-axis.

A marked temperature dependence of the spin lifetimes is evident for both excitation densities, with a trend to lower spin lifetimes towards both the lower and the higher boundary of the investigated temperature range. Most notably, maximum spin lifetimes of $\approx 65\,\text{ns}$ are found at intermediate temperatures of $50\,\text{K}$.

For the range of applicable excitation densities, the electron spin lifetimes appear to differ only for temperatures below $\sim 30\,\text{K}$, where a higher excitation power leads to a slight enhancement of the spin lifetime.

At temperatures of $116\,\text{K}$, the spin lifetimes are found to be still as long as $5\,\text{ns}$, consistent with a previous report [65]. In this regime, the deviations significantly increase for each bin, as evident from the larger error bars. The reason for this issue is explained by a constant lower boundary of the achievable noise level: When the temperature is raised, the absorption coefficient increases [23], which leads to a reduction of the power of the probe beam behind the sample. Ordinarily, a reduction of probe power lowers both the signal and the noise level in the photodiode, such that the signal-to-noise ratio remains unaffected. However, as the noise level is in this case limited by shot noise, a reduced probe power results in the reduction of the signal-to-noise ratio. Ultimately, the fitting algorithm increasingly often converges in peaks that correspond to noise rather than a resonance peak.

The results for $T \geq 60\,\text{K}$ agree very well with theoretical predictions for T_s that model inter- and intra-valley phonon scattering in germanium [26]. As this model founds on Elliott-Yafet type mechanisms, the inherent temperature dependence is of the form $\tau_\text{S} \propto \frac{1}{T}$ for high temperatures [4, 46, 47]. Although it was stated in [4, 66] that this $\frac{1}{T}$ dependence of the Elliott-Yafet relaxation should also apply to low temperatures in nondegenerate[3] semiconductors, no such trend is observed in the experimental data. The discrepancy between the theoretical predictions and the experimental data presumably lies in the fact that in detail the temperature dependence of the carrier mobilty depends on the exact doping or impurity concentration [67, 68] and on which dopants are inherent in the material. Therefore, as the above-mentioned model neglects a detailed analysis of the impurity scattering, it fails to explain the decrease of T_s for lower temperatures.

Since the curves in Fig. 4.3 resemble temperature dependencies that are typical of carrier mobilities for relatively high doping concentrations [67, 68], it is still reasonable to address the observed temperature trend to dominant Elliott-Yafet relaxation. Indeed, several groups have reported a similar temperature trend for spin lifetimes at low temperatures in different experimental approaches [69, 70].

---

[3]The term *degenerate* refers to semiconductors that contain such elevated doping concentrations that the semiconductor acts as a conductor or metal.
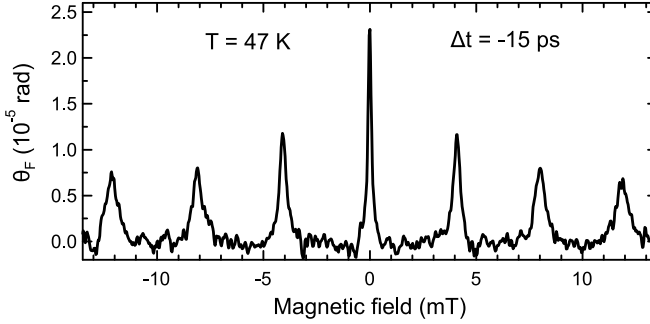
Figure 4.4: RSA trace at $\Delta t = -15\,\mathrm{ps}$ for a variable magnetic field between $-15\,\mathrm{mT}$ and $15\,\mathrm{mT}$ at an elevated temperature of T = 47 K. At this temperature, the peak widths show a pronounced dependence on the absolute value of the magnetic field. A slowly varying background fluctuation is subtracted from the data with the help of a FFT high pass.

In line with the discussed results and the theoretical model of [26], the utilization of ultrapure Ge specimens should facilitate even higher spin lifetimes. This assumption is substantiated by the fact that ultrapure Germanium (with residual doping concentrations on the order of down to $2 \times 10^{12}\,\mathrm{cm}^{-3}$) have been proven to exhibit significantly higher carrier mobilities [71]. The finding of decreased spin lifetimes for lower excitation densities at low temperatures is further indicative of a dominant ionized impurity scattering, as a higher excitation density results in a screening of the impurities and consequently in an increase in carrier mobility [68].

4.2   Spin Coherence Times

At low temperatures, the observed RSA peaks do not reveal a specific dependence on the exact magnetic field strength (c.f. Fig. 4.2). However, as the temperature rises, the differences between peaks at different values of $|B|$ tend to increase.

In figure 4.4, an RSA trace is depicted for a sample temperature of $\approx 47\,\mathrm{K}$, showing the Faraday rotation angle θ_F for a variable magnetic field of $\approx -15\,\mathrm{mT}$ to $15\,\mathrm{mT}$. Again, the magnetic field is applied in Voigt geometry. The central peak at $B = 0\,\mathrm{mT}$ has a small width, corresponding to the enhanced spin lifetimes in this temperature region (c.f. Fig. 4.3). However, the side peaks broaden for increasing magnetic field strengths.
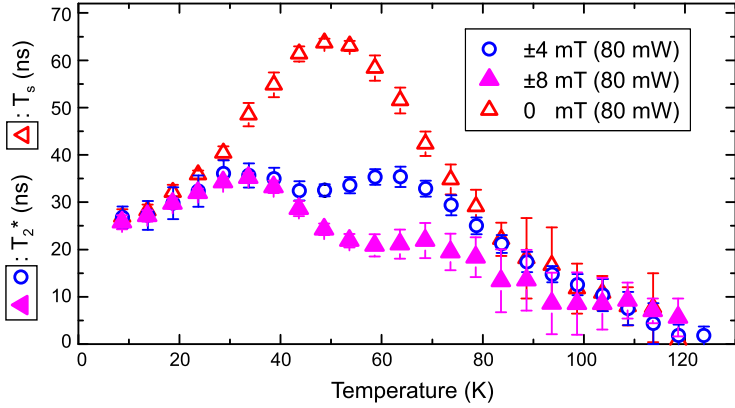
Figure 4.5: Temperature dependence of the electron spin coherence times T_2^*, corresponding to the first and second side peaks of the RSA trace at $\pm 4\,\mathrm{mT}$ and $\pm 8\,\mathrm{mT}$, respectively. Error bars represent the standard deviation of measurements within a temperature interval $\Delta T = 5K$. The results are compared with the values for the spin lifetime T_s (red open triangles, c.f. 4.1).

As the peaks to the sides of the center represent the resonances after integer multiples of one full Larmor precession cycle within the laser repetition period, this finding points to an ongoing decoherence of the spin ensemble. In order to study this decoherence effect in more detail, the temperature dependence of the peak widths is investigated for the first and second side peaks at $\approx \pm 4\,\mathrm{mT}$ and $\approx \pm 8\,\mathrm{mT}$, respectively.

In figure 4.5, the temperature dependence of the coherence times is depicted for these peaks. The experimental data for the first sidepeak are shown as blue circles, while the T_2^* times for the second side peaks are shown as magenta triangles. For better comparability, the previous results on the spin lifetimes are laid on top of the coherence times. Analogous to the results shown in the previous chapter, the data are binned to $\Delta T = 5\,\mathrm{K}$ and the error bars show the variation within the bins. All corresponding RSA peaks are recorded with pump beam average powers of $80\,\mathrm{mW}$. In the context of this evaluation, the results for the peaks at nominally positive and negative magnetic fields are treated as equal.

Similar to the findings for the spin lifetimes, the coherence times tend to decrease for the lowest temperatures. The spin ensemble coherence times show a markedly

different behavior compared to the pure spin lifetimes T_s at zero magnetic field for temperatures of $30\,\text{K} < T < 90\,\text{K}$. In this region, the coherence times stay at a relatively constant value of $\approx 34\,\text{ns}$ for $B = \pm 4\,\text{mT}$, which means a reduction by a factor of up to ~ 2 caused by the magnetic field. At temperatures of $T > 80\,\text{K}$, the decoherence incurred within one Larmor precession does no longer significantly reduce the persistence of the spin polarization.

In general, coherence times tend to decrease for increasing magnetic fields. Phenomenologically, this trend is explained by the circumstance that the faster an ensemble of spin precesses around the magnetic field, the faster the relative orientation of the individual spin carriers is randomized by momentum scattering events. Therefore, the decoherence should play an enhanced role for the second side peaks at $B = \pm 8\,\text{mT}$, compared to the case of $B = 0\,\text{mT}$ or $B = \pm 4\,\text{mT}$.

This trend has also been previously reported in experimental studies in germanium [24]. However, the reported magnetic fields on which this decrease in T_2^* is observed are at least one order of magnitude stronger than the applied $4\,\text{mT} - 8\,\text{mT}$. Indeed, as evident from Fig 4.5, no such reduced coherence times of the spin ensemble are seen for these low magnetic fields for $T \leq 30\,\text{K}$.

Generally, it can be stated that in this temperature range the decoherence times that correspond to $B = \pm 8\,\text{mT}$ behave very similar to those at the first side peaks and to the lifetimes at the central peaks. Furthermore, the T_2^* times at $B = \pm 8\,\text{mT}$ first appear to have a similar temperature dependence as for the case of $B = \pm 4\,\text{mT}$ for increasing temperatures of $30\,\text{K} < T < 40\,\text{K}$. It is not until the temperature exceeds $\sim 40\,\text{K}$, where a further reduction of the T_2^* times becomes apparent, with the maximum difference of the coherence times being $14\,\text{ns}$ at a temperature $T = 60\,\text{K}$. A further increase in temperature diminishes the difference between the individual lifetimes and coherence times, until no significant difference remains at $T \geq 90\,\text{K}$.

The presented experimental results of the T_s and T_2^* times reveal a very interesting dependence on the temperature, as well as the magnetic field. Owing to the reliable results for low magnetic fields accessible with the RSA method, a detailed structure of the spin ensemble decoherence can be mapped. The temperature trend of the electron spin ensemble's coherence time shows a strikingly pronounced structure for the different numbers of full Larmor precession cycles, owing to the onset of spin decoherence.

4.3   Signatures of g-Factor Anisotropy in RSA

So far, the resonant spin amplification technique has been performed in Voigt geometry, with a surface orientation of the sample normal to the [100] direction and a magnetic field along the [010] orientation of the germanium crystal. This has been done in order to be able to analyze the spin lifetimes and coherence times without having to take the g-factor anisotropy into account, as for this specific configuration only one effective g-factor remains.

Referring to the studies conducted by C. Hautmann [25], chapter 2.5 discussed the influence of the magnetic field orientation on the g-factor splitting for samples with [111] and [100] surface orientation. In the present chapter, the impact of the g-factor anisotropy on the RSA signal is investigated for the more simple case of the [100]-oriented specimen.

When the g-factor anisotropy was introduced in this thesis, a notation was used that utilized the angle α to define the orientation of the magnetic field within the sample plane. It is advantageous to use α when discussing the spin coherence times, as a manipulation of this angle does not change the underlying relaxation mechanisms, i.e., if T_1 or T_2^* is addressed (c.f. Chap. 1.3). Unfortunately, the manipulation of α is experimentally inconvenient, as it requires to either rotate the sample within the cryostat, the cryostat itself, or the magnetic field along the direction of gravity. Therefore, another angle β is introduced, which denotes the magnetic field orientation with respect to the [010] axis, i.e., $\beta = 0° \,\widehat{=}\, \mathbf{B} \parallel [010]$ and $\beta = 90° \,\widehat{=}\, \mathbf{B} \parallel [\bar{1}00]$. While a manipulation of this angle of the magnetic field would mess up the discussion of spin coherence times, it does not cause any issues when only the influence on the g-factors is discussed, and the magnetic field can be conveniently manipulated when the electromagnet is placed on a rotational stage. Moreover, the angle-dependence of the g-factor splitting is equal for a manipulation of α or β.

In Fig. 4.6, the TRFR of the electron spin ensemble in the 4.7 mm [100]-oriented sample (sample 3, c.f. Tab.2.2) is shown for two values of α. In the upper panel of the figure, the magnetic field is aligned along the [010] crystallographic axis, corresponding to $\alpha = 45°$ or $\beta = 0°$. It shows a well-resolved Larmor precession signal, which corresponds to an effective g-factor of $g^* = 1.62$, resembling the case that has been discussed in the previous chapter (c.f. Fig. 4.1). For the results in the lower panel of Fig. 4.6, the in-plane orientation of the sample is rotated such that the magnetic field is tilted to $\alpha \approx 9.5°$ towards the [001] axis. In this case, two different g-factors can be derived from the TRFR data, revealing $g_{1,2}^* = 1.72, 1.52$.

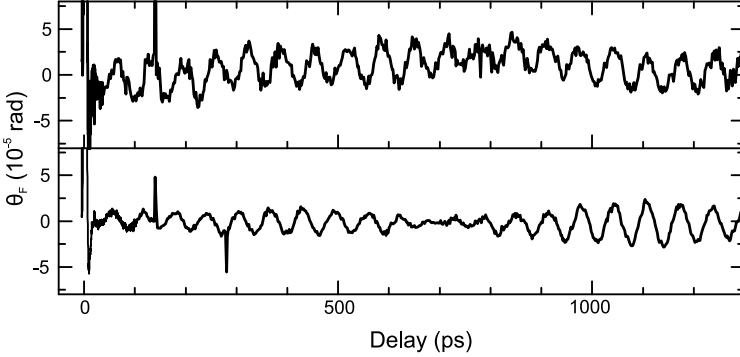**Figure 4.6:** TRFR transients observed in Ge sample 3 at $T = 8\,\text{K}$ and $B = 670\,\text{mT}$. Upper panel: Magnetic field oriented along the [010] crystallographic axis ($\alpha = 0°$, $\beta = 0°$). For the lower panel, the Ge piece is rotated such that the in-plane magnetic field is tilted by 9.5° towards the [001] axis ($\alpha = 9.5°$, $\beta = 0°$). A time-independent offset is subtracted for clarity.

For the data in the upper panel only one circular polarization of the pump is used (σ^+), while for the lower panel both circular polarization states are utilized ($\sigma^+ - \sigma^-$), explaining the deviation in the signal-to-noise ratio [4].

For the above-mentioned reasons, the manipulation of the magnetic field orientation is now performed by the angle β. Similar to the TRFR transients depicted in Fig. 4.6, now, RSA traces are recorded for different orientations of the magnetic field. All measurements are carried out at a fixed negative delay time of $\Delta t = -15\,\text{ps}$. The experiments are carried out at a constant, low temperature of $T \approx 8\,\text{K}$. RSA traces at this temperature do not yield the maximum achievable spin lifetimes, but show the least pronounced magnetic field dependence of the individual peaks, which makes it possible to disregard the magnetic field dependence of the peak widths in the model function given by Eq. (2.7).

On the left hand side of Fig. 4.7, RSA traces are depicted for three different orientations of the magnetic field. To the right of each panel, sketches are provided that

---

[4]Initially, no close attention was paid to the recording of this data, as these measurements were initially intended to be carried out in order to solely find out the sample's in-plane orientation of $\alpha = 0°$
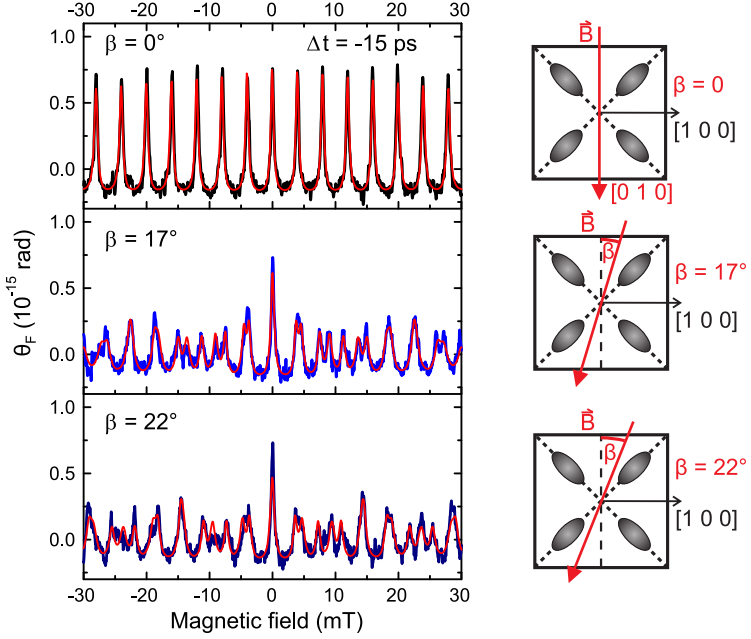
Figure 4.7: RSA at a fixed negative delay of $\Delta t = -15$ ps for a magnetic field between -30 mT and 30 mT. The 4.7 mm thick, [100]-oriented Ge sample is kept at a temperature of $T = 8$ K. The upper panel shows an RSA trace for pure Voigt geometry ($\beta = 0°$). The central and bottom panel show the RSA traces for magnetic field orientations of $\beta = 17°$ and $\beta = 22°$, respectively. The red solid line in the top panel is a fit to the data according to Eq. (2.7). For the central and the bottom panel, the red solid lines are fits to the data using a superposition of the function from Eq. (2.7) with two distinct g-factors. The fitted values of the effective g-factors are summarized in table 4.1. The sketches on the right side of each panel illustrate projections of the real-space and k-space geometrical arrangements onto the x-y plane.

	g_1^* (theory)	g_1^* (fit)	g_2^* (theory)	g_2^* (fit)
$\beta = 0°$	1.62	1.62	-	-
$\beta = 17°$	1.44	1.43	1.78	1.73
$\beta = 22°$	1.39	1.37	1.82	1.78

Table 4.1: Summary of the g-factors present in Ge for the different geometrical arrangements depicted on the right side in Fig. 4.7. Theoretical values are obtained from Eqs. (2.10), (2.11). The other columns contain the values used to achieve the best overall agreement between the red solid lines in Fig. 4.7 and the experimental data.

illustrate the corresponding projections of the real-space and k-space geometrical arrangements onto the x-y plane.

As shown exemplarily for $\beta = 17°$ and $22°$, the resonance pattern becomes more complicated since the electrons in the different L-valleys precess with two different frequencies. To model this situation, the data are fit with the superposition of two RSA shapes from Eq. (2.7) with two different g factors. The red lines on the left panel of the figure show the result of this procedure using $\tau = 26$ ns for $\beta = 0°$, $\tau = 22$ ns for $\beta = 17°$, as well as $\tau = 18$ ns for $\beta = 22°$. The g-factors deduced from the fit are summarized in Tab. 4.1. As evident from the table, the values are in fair agreement with the theoretical expectations given by Eqs. (2.10) and (2.11).

The fitting curves are in good overall agreement with the experiment and are capable of reproducing the complex beating pattern of the RSA traces. Residual differences are likely related to a small misalignment of the orientation of the magnetic field. It is worth mentioning that the choice of slightly smaller values of τ for the cases of $\beta \neq 0$ mainly improves the agreement between the simulation and the beating pattern at $B \neq 0$. The mere peak width around $B = 0$ points to very similar values for τ for all β. However, as pointed out in Chap. 2.3, the applied model function fails to provide a good measure of the involved lifetimes or coherence times. Due to the complex structure of the RSA traces, the impact of the magnetic field orientation on the spin ensemble decoherence cannot be studied for the cases of $\beta \neq 0$.

4.4 Discussion and Outlook

The study presented in this chapter has provided experimental results on the spin ensemble lifetimes and coherence times in the semiconductor germanium based on the resonant spin amplification technique. Highly elevated spin coherence times on the order of several nanoseconds were found with a low repetition rate, high power laser system. By switching to a laser system with repetition periods on the order of the spin coherence time, the necessary condition for RSA measurements could be met: a persisting spin ensemble coherence for nominally negative pump-probe delay times.

The RSA measurement technique has subsequently been carried out on a [100]-surface oriented sample of high purity. A viable signal-to-noise ratio of ~ 10 is achieved, despite the fact that the excited carrier densities are as low as $\approx 6 \times 10^{12}\,\mathrm{cm}^{-3}$.

Most strikingly, a simultaneous heating of the cryostat during the recording of the RSA traces has been proven to allow the tracking of a detailed temperature dependence of the spin lifetimes around zero magnetic field. As a result, the observed lineshape of the temperature dependence points towards a dominant Elliott-Yafet relaxation. In comparison with theoretical predictions [26], a good agreement is found for temperatures of $T \geq 50\,\mathrm{K}$. Deviations from the theory can only be seen for low temperatures and are found to be attributable to the lack of ionized-impurity scattering in the theoretical model.

The experimental study reveals maximum spin lifetimes at intermediate temperatures of $T \approx 50\,\mathrm{K}$ with a remarkably high value of $T_s \approx 65\,\mathrm{ns}$. In contrast, results on electron spin lifetimes at zero magnetic field in bulk, direct semiconductors commonly report values as low as several tens to hundreds of picoseconds, depending on the doping concentration and temperature. In particular, values of $\sim 15\,\mathrm{ps}$ have been reported for GaSb [72] and $\sim 200\,\mathrm{ps}$ for InGaAs [52], respectively. Electron spin lifetimes of bulk, direct semiconductors comparable to the ones obtained in this thesis for germanium have been reported in n-type GaAs. However, these elevated spin lifetimes correspond to donor-bound electrons and can only be observed for certain doping concentrations and excitation conditions [13, 14, 52].

Astonishingly, the presented experiments reveal that for the given specimen the spin lifetimes at temperatures that are achieved with liquid helium ($\sim 5\,\mathrm{K}$) cooling yield the same value as for temperatures that can be achieved by cooling with the much more widely available liquid nitrogen ($77\,\mathrm{K}$). With regard to the experimental

results reported by other groups, it is probable that the utilization of high purity germanium samples might allow to achieve even higher spin lifetimes [69].

By tracking the temperature dependence of the first and second side peaks of the RSA trace, a detailed analysis of the onset of spin ensemble decoherence is given. A central result of this study is the insight on the temperature dependence of the spin ensemble decoherence: While the low magnetic fields do not alter the spin ensemble coherence for temperatures below 30 K, coherence times for increasing magnetic fields begin to strongly deviate from the spin lifetimes at zero magnetic field, once the temperature exceeds this value.

It is remarkable that the RSA technique enables the study of the spin ensemble decoherence for magnetic fields as low as equivalent to one full Larmor precession over the laser repetition period. In contrast, conventional TRFR-based experiments require magnetic fields with at least two orders of magnitude higher strengths. The presented experimental results based on RSA therefore provide novel fundamental insight on the process of spin ensemble decoherence in the indirect semiconductor germanium for realistic conditions of collateral magnetic fields of low field strengths with respect to possible future systems of quantum computing or spintronic devices.

A theoretical description for the complex temperature trends of the spin coherence times for $|B| > 0$ does not yet exist. This issue is partially related to the fact that, to best knowledge, no study on the magnetic field dependence of the Elliott-Yafet type relaxation has been carried out to date [4]. Future experiments should therefore aim to provide an increasingly wide-ranging study of the magnetic field dependence of the spin lifetimes in indirect semiconductors in order to further elucidate this fundamental correlation. As in detail the EY-relaxation depends on the carrier mobility, such a study would need to imply an analysis of the impact of different doping materials and concentrations.

In an additional experimental approach, it was possible to show the influence of g-factor anisotropy on the shape of the RSA traces. A simple model based on the superposition of two RSA traces of the form of Eq. (2.7) that utilizes different g-factors was introduced and it was shown to agree well with the experimental data. From a physics point of view, this result indicates that electrons from different L-valleys precess independently from each other and do not intricately interact for the given parameters of the magnetic field and temperature. Moreover, this part of the experiment demonstrated that the decoherence studies could only be carried out with the RSA method by carefully orientating the magnetic field with respect to the crystallographic axes. For alignments of $\beta \neq 0°$, it is apparent that the RSA trace

is rapidly gaining complexity, obstructing a possible analysis of the side peaks that has been necessary for the decoherence studies.

Owing to the comparatively high spin lifetimes and coherence times at an intermediate temperature range, especially in the temperature region accessible with liquid nitrogen cooling, the results reported in this chapter open up interesting perspectives for spin-optoelectronics in indirect group IV materials. In order to achieve even higher spin-lifetimes, future experiments should aim towards utilizing ultrapure Ge specimens, such as the ones as reported in [73]. Improvements in terms of spin lifetime [26] and efficiency by the degree of spin polarization [74] are also predicted for strained Ge epilayers. Therein, the L-valley degeneracy is partially lifted such that intervalley scattering is reduced.

Many of the aspects observed in the presented study should be directly transferable to silicon, where even longer lifetimes of optically injected electron spins can be expected due to its less pronounced spin-orbit coupling, which mitigates the Elliot-Yafet relaxation process. Additional to the already mentioned improvements, optical orientation efficiencies and spin coherence times could be further enhanced by using SiGe alloy crystals [75, 76], as these have already been proven to show promising applicability in the field of quantum-computing [77]. Moreover, in structures of reduced dimensionality such as Ge/SiGe quantum wells [78], a further increase of the robustness of the electron spin is to be expected. However, as the present study has shown that the indirect semiconductor samples are required to have a considerably high thickness in order to obtain a satisfactory level of signal strengths, it is questionable whether magneto-optical studies can be applied to these structures in the future.

Part II

Dynamical Response of the Lower Exciton-Polariton Branch in CdZnTe

Introduction

Analogous to the well-known rule of thumb for the number of transistors in integrated circuits to double every two years and thus continuously increasing their capability, known as Moore's law [79], similar trends can be observed for the rate of data transfer. Most astonishingly, due to the continuous development of novel techniques such as space division multiplexing, the transmission capacity of single optical fibers has been reported to increase by a factor of 10 every four years [80], recently achieving rates of 10^{15} bits per second [81]. However, contemporary data transfer with optical fibers partially relies on electro-optical conversion, which is accompanied by an undesirable increase in latency, as well as heating. The substitution of electrical processing and switching can therefore be identified as one of the key aspects of roadmaps for future improvements of communication based on fiber optics [82, 83].

It is hardly surprising that, due to the interest driven by information technology, a variety of concepts have emerged in order to supersede the electronics based manipulation and switching. Besides rather exceptional concepts such as digital processing with molecular switches [84], a more obvious approach is given by all-optical methods. Therein, a central goal is to fabricate logic gates that can be exclusively operated by photons or macroscopic light beams. As all applications of optics in this context will still require the use of electronics to some extent [82], it is highly desirable to implement novel optical techniques in the well-known semiconductor foundation [85].

Although concepts of optical control of light in semiconductors have been addressed by researchers since more than a decade [85], the scientific interest in this topic and the consequential amount of related publications is continuously increasing [86]. In this context, the field of plasmonics provides great improvements by means of all-passive simple optical logic gates and interconnects utilizing nanostructure waveguides grown on semiconductors [87, 88]. Yet, a need for actively controlled elements such as transistors remains. Ultra-efficient single-photon transistors have been demonstrated just recently [89, 90], although their applicability is more likely

to be seen in the field of quantum computing [91]. Other concepts suggest the exploitation of the characteristic dynamics and the strong nonlinear interaction of polaritons for optical manipulation purposes, identifying the potential cascadability of these systems as one of the key advantages [92].

Due to their nature of being a superimposed state of photons who couple strongly to the polarization in a material, the quasi-particles called polaritons do indeed feature very distinct propagation dynamics. First described by S. I. Pekar [93] and J. J. Hopfield [94], an exciton, itself being a quasi-particle formed by a bound electron-hole pair inside a semiconductor, can strongly couple to a photon from an incident field of light. More specifically, the coupling of the excitonic polarization of the material to the photonic field leads to the formation of yet another kind of quasi-particle, called exciton-polariton.

As a result of the consequential anticrossing of the excitonic and photonic dispersion, the polariton dispersion is divided into two branches called upper and lower polariton branch. Most interestingly from a physics point of view, these dispersion curves feature a comparatively shallow slope. In combination with the identity of the group velocity $v_g = \frac{\partial \omega}{\partial k}$, a substantial delay of light passing through the semiconductor material can be deduced for photon energies close to the exciton resonance [95]. Recent studies have proven the slow light propagation related to the lower-polariton branch dispersion experimentally, reporting delays up to 1 ns even in submillimeter-thick crystals [96, 97].

While the substantial time delays arising from the exciton-polariton propagation have been studied in various materials, less attention has been paid by the scientific community to achieve a dynamical control of such resonances, although advances in this field might offer interesting possibilities from a technological perspective. In particular, an ultrafast manipulation of the light delay arising from the exciton-polariton propagation may provide options for a major downscaling, compared to present concepts for tunable optical delays, such as in optical fibers [98], where comparatively high interaction lengths are necessary.

Studies on the dynamic optical manipulation of such a system have so far mainly utilized photon energies right at the exciton resonance [99] or slightly higher energies [100]. In this energetic regime, the dynamics of the exciton-polariton are mostly resembling those of the bare exciton, thus often being referred to as exciton-like. Consequently, the material exhibits a marked nonlinear optical response at these energies and the dynamics related to the exciton-polariton are strongly susceptible to perturbations of the exciton resonance, such as excitation-induced dephasing (EID) [101] or exciation induced shift (EIS) [102]. While this also holds true for the

lower polariton branch, i.e., for energies slightly below the exciton resonance, the associated substantially lower absorption further below the band gap of the material enables the utilization of higher crystal lengths in transmission geometry. In combination with the slow light propagation, the interaction times of light with the material can therefore be increased compared to the utilization of photon energies above the resonance. As a result, an induced excitation of the sample can be expected to have an increasing impact on light propagating on the lower polariton branch.

Motivated by these expectations, the present second part of this thesis aims to provide insight on the ultrafast dynamics of light propagating on the lower polariton branch. The utilized specimens are two slabs of $Cd_{0.88}Zn_{0.12}Te$ with thicknesses of $208\,\mu m$ and $75\,\mu m$. The choice of this material is motivated by the fact that CdZnTe is expected to show highly pronounced exciton-polariton effects that can be addressed with photon energies at around $1.67\,eV$, which are conventiently accessible. In particular, the longitudinal-transversal splitting energy of the exciton-polariton, which is commonly addressed as a measure for the importance of polariton effects [99], was found to be as high as $\Delta_{LT} = 0.65\,meV$ for $Cd_{0.88}Zn_{0.12}Te$ [103], while in GaAs a value of $\Delta_{LT} = 0.08\,meV$ has been reported [95]. Another beneficial trait of the selected material is the fact that CdZnTe of similar admixtures is well studied and widely available due to its advantageous properties for high-energy photodetectors [104] and solar cells [105].

A substantial slow-light propagation related to the lower polariton branch has been proven in $Cd_{0.88}Zn_{0.12}Te$ in a specimen of the same wafer [103]. Furthermore, the studies conducted in this thesis may benefit from photoluminescence data on the present material published jointly with the time-of flight studies on the slow-light propagation.

In an experimental approach, the dynamical response of the system to external photoexcitation is analyzed in a spectrally resolved pump-probe measurement scheme with the help of femtosecond laser pulses. While the results obtained from this study may provide interesting insight into the dynamics of the fundamental physical processes involved, a distinct focus of the second part of this thesis is to answer, to what extent the enhanced nonlinear interaction can be exploited to achieve a macroscopic suppression of the probe beam transmission on ultrafast time scales. From a technological perspective, the latter might open up interesting possibilities of all-optical manipulation and switching in semiconductors on time scales as low as several picoseconds.

This part of the thesis is composed of three different chapters: Chapter 1 serves as a first introduction to the topic in order to provide a theoretical background on excitons in the Lorentz oscillator model. Furthermore, the concept of exciton-polaritons is introduced along with fundamentals of optical manipulation of these quasi-particles. Subsequently, the experimental setup is outlined in Chap. 2, which founds on the laser system that has already been utilized in the first part of this thesis. In addition, more information is given on the investigated $Cd_{0.88}Zn_{0.12}Te$ sample. In this context, also the energetic configuration of the all-optical study is clarified, relating the pump and probe photon energies to the characteristic resonance positions of the material. Finally, chapter 3 reviews the experimental study starting with spectrally integrated differential transmission transients obtained from pump-probe measurements that give rise to the involved time scales and excitation conditions. In a following, more profound study, the differential transmission dynamics are spectrally resolved by detecting the probe spectrum with a monochromator. With the help of a theoretical model provided by the group of T. Meier [106] from the University of Paderborn, individual contributions to the overall signal are identified for different pump-probe delay times in order to gain insight on the involved fundamental processes.

Regarding the potential feasibility of the induced transmission changes in terms of optical switching, the experimental investigation will address the issue, to what extent the nonlinear interaction can be enhanced by increasing the pump irradiance. Therein, a particular focus is set on the impact of heat deposition into the sample.

Parts of the results presented in this part of the thesis have been published in [106] and [107].

Chapter 1

Theoretical Background

As stated in the first part of the thesis at hand, the excitation of an electron from the valence band to the conduction band leaves a positively charged hole in the valence band. The Coulomb interaction then allows for a new quasi-particle to be formed, which is called exciton. If an electromagnetic field is present in the same semiconductor, the strong coupling of the photons with the excitons once again creates a superimposed state that can be treated as a quasi-particle. This new particle called exciton-polariton shares the characteristics of both individual particles.

The present chapter aims to provide an overview of the fundamental physics of excitons and exciton-polaritons. To this end, the Lorentz oscillator model is introduced, which allows for a qualitative explanation of the dynamics of the excitonic resonances. Following this introduction, the polariton concept is outlined for the present case of exciton-polaritons together with the corresponding dynamics and principles of their optical manipulation.

1.1   Wannier-Mott Excitons

Most commonly, one differentiates between two different types of excitons: Wannier-Mott [108] and Frenkel [109] excitons. The term *Frenkel exciton* denotes excitons that are confined within one or two unit cells. They predominantly appear in ionic crystals, where the Coulomb interaction between the electron and hole is comparatively strong. However, in most semiconductors the valence band electrons contribute to a screening of the Coulomb potential of the electron and hole involved in the excitonic bond. Due to this screening, the coupling of the electron and hole is weaker than for the Frenkel exciton. In this case, excitonic wave functions can
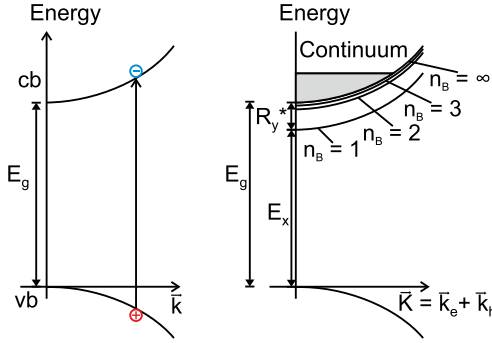
Figure 1.1: Left side: Schematic of the excitation of an electron-hole pair in a band structure model of a direct semiconductor. Right side: Energetic position of bound excitonic states in a direct semiconductor, schematically adopted from [31].

span over numerous unit cells [110] and the excitons are called *Wannier-Mott excitons*. Since the Frenkel exciton plays no important role for the sample material investigated in this thesis, the term *exciton* will followingly denote Wannier-Mott excitons.

Similar to the hydrogen atom, in the parabolic band approximation in a direct semiconductor, the movement of electron and hole can be separated into a centroid and a relative movement. Consequently, the energy of the exciton reads [31]:

$$E_{\text{ex}} = E_g - E_{\text{Ryd}}^* \frac{1}{n_B^2} + \frac{\hbar^2 \mathbf{K}^2}{2M} \tag{1.1}$$

Here, the following abbreviations and constants are included:

$$n_B = 1,2,3,\ldots \qquad\qquad \text{Excitation quantum number}$$
$$E_{\text{Ryd}}^* = 13.6\,\text{eV}\,\frac{\mu}{m_0 \epsilon_r^2} \qquad\qquad \text{Excitonic Rydberg energy}$$
$$M = m_e + m_h \qquad\qquad \text{Total mass of electron and hole}$$
$$\mathbf{K} = \mathbf{k_e} + \mathbf{k_h} \qquad\qquad \text{Total wave vector}$$
$$\mu = \frac{m_e m_h}{m_e + m_h} \qquad\qquad \text{Reduced mass of the exciton}$$
$$\epsilon_r = \qquad\qquad \text{Relative dielectric constant of the semiconductor}$$

The energetic displacement of the exciton compared to the band gap energy is correspondingly given by a modified Rydberg energy R_y^*. Adding the excitonic states

to the conventional semiconductor band structure scheme leads to a picture as seen in Fig. 1.1, right side. Due to this energetically more favorable configuration of electrons and holes that leads to the formation of states below the band edge, it is also possible to directly inject bound excitons by exciting a valence band electron with photon energies of $\hbar\omega = E_g - R_y^*$. Typically, R_y^* is on the order of $\sim 10\,\text{meV}$ [111]. In bulk[1] semiconductors, excitonic effects can only be observed for low temperatures, as the thermal energy $k_B T$, given by the Boltzmann constant and the temperature, exceeds the binding energy of the exciton for temperatures of $T > 100\,\text{K}$.

1.2 The Lorentz Oscillator Model

As the results given in the following chapters can partially be related to the manipulation of a Lorentzian function, this section aims to provide the corresponding mathematical background. The theoretical descriptions that are carried out in this section can be found in common literature, such as [112].

The Lorentzian model assumes that electrons are independent harmonic oscillators that oscillate relative to their equilibrium position with their respective eigenfrequencies ω_1. As excitons can be treated as particles on their own, it is also possible to describe excitons in the oscillator model. In particular, the oscillator model assumes that the response of the system towards excitation with external fields is linear and consequently does not cover any nonlinear optical effects. If the oscillators are driven by an external electromagnetic field with the optical frequency ω, the response of the system is of the form of a resonance curve, which is sensitive to the frequency mismatch $\omega - \omega_1$. Due to scattering processes and the dipole radiation of the oscillator, the resonance is damped. As a result of this model, the dielectric function of the Lorentz oscillator reads:

$$\epsilon(\omega) = \epsilon_b + \frac{f}{\omega_0^2 - \omega^2 - \mathrm{i}\gamma\omega} \tag{1.2}$$

Here, $f = \frac{N_V e^2}{\epsilon_0 m}$ is the oscillator strength with the volume density N_V of the number of oscillators in the medium, m is the mass of the oscillator, and ϵ_0 is the dielectric constant. The term γ accounts for the damping, and i is the imaginary unit. The eigenfrequency ω_1 corresponds to a resonance in the electronic polarizability α of the medium. However, when the dielectric function is calculated from the polarizability (Clausius-Mossotti relation), a nominal shift of the resonance frequency is induced,

---

[1]The term *bulk* is commonly used to refer to materials or samples with macroscopic dimensions, which do not involve structures on the nanoscale
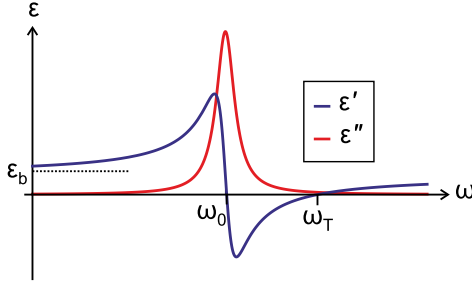
Figure 1.2: Schematic curve shape of the real (ϵ') and imaginary part (ϵ'') of the dielectric function of a Lorentz oscillator for non-zero damping.

which is incorporated by $\omega_0^2 = \omega_1^2 + \frac{1}{3}f$ in Eq. (1.2). Lastly, the constant ϵ_b takes care of the dielectric function of the surrounding matter, which is given by the semiconductor material in the present case.

As the complex refractive index is given by $\tilde{n}^2(\omega) = \epsilon(\omega)$, the real and imaginary part of the dielectric function (in the following indexed by ' and '') are related to the refractive index n_0 and the absorption κ, via:

$$\tilde{n}^2(\omega) = (n_0 + i\kappa)^2 = \epsilon' + i\epsilon'' \tag{1.3}$$

$$n_0^2 - \kappa^2 = \epsilon' \tag{1.4}$$

$$2n_0\kappa = \epsilon'' \tag{1.5}$$

According to 1.2, the real and imaginary part of the dielectric function consequently read:

$$\epsilon' = \epsilon_b + \frac{f(\omega_0^2 - \omega^2)}{\gamma^2\omega^2 + (\omega_0^2 - \omega^2)^2} \tag{1.6}$$

$$\epsilon'' = \frac{f\gamma\omega}{\gamma^2\omega^2 + (\omega_0^2 - \omega^2)^2} \tag{1.7}$$

The characteristic plot of these functions is depicted in Fig. 1.2, revealing the well-known Kramers-Kronig type picture of the real and imaginary part of a resonance. In this graph, two important frequencies can be identified: the already mentioned resonance frequency ω_0 as well as the frequency ω_T, which are the two solutions for the equation $\epsilon'(\omega) = 0$.

The refractive index n_0 and the absorption κ can now be separated in order to obtain the influence of a Lorentzian resonance on the external electromagnetic field:

$$n_0 = \sqrt{\frac{1}{2}\left(\epsilon' + \sqrt{\epsilon'^2 + \epsilon''^2}\right)} \tag{1.8}$$

$$\kappa = \sqrt{\frac{1}{2}\left(-\epsilon' + \sqrt{\epsilon'^2 + \epsilon''^2}\right)} \tag{1.9}$$

In particular, this result can be used to describe how an electromagnetic wave is altered when it passes through the medium in proximity of the resonance, for example by applying Eq. (1.8) and (1.9) to the function of a plane wave propagating in the z direction, which is given by:

$$E(\omega,t) = E_0(\omega)\mathrm{e}^{\mathrm{i}\left[(n_0 + \mathrm{i}\kappa)\frac{\omega}{c}z - \omega t\right]} = E_0(\omega)\mathrm{e}^{-\kappa\frac{\omega}{c}z}\mathrm{e}^{\mathrm{i}(n_0\frac{\omega}{c}z - \omega t)} \tag{1.10}$$

1.3 The Polariton Concept

So far, when light-matter interaction was discussed in this thesis, the excitation with external electromagnetic fields was treated as a weak perturbation of the system, leading to a certain amount of optically excited carriers. This treatment was justified, since the light-matter interaction that leads to transitions from the continuum of valence band states to the conduction band states was sufficiently weak, especially in the case of indirect transitions. However, for a strong coupling of the electromagnetic field to the matter, e.g., at the vicinity of an isolated optical resonance, one has to give a closer look at the way light and matter interact [31].

In general, an external electromagnetic field $\mathbf{E}$ that travels through a medium induces a polarization that is given by its dielectric function:

$$\mathbf{P} = \epsilon_0[\epsilon(\omega) - 1]\mathbf{E} \tag{1.11}$$

Consequently, an oscillating electric field also leads to an oscillating polarization in the medium, which then again emits an electric field and so on. In a quantum-mechanical picture, this interaction can be treated as a quasi-particle, when the photon energies from the electromagnetic field are close to a resonance, where $\epsilon(\omega)$ is increased. Due to their nature of being an admixture of photons with the material's polarization, these type of quasi-particles were given the name *polaritons* [31, 93, 94, 113].

Depending on the (quasi-) particle(s) involved, there are several different types of polaritons, for example, plasmon-polaritons [114] or phonon-polaritons. Generally
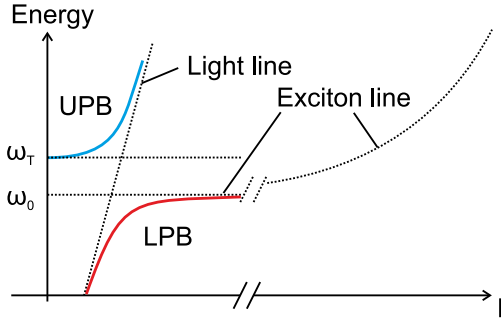
Figure 1.3: Anticrossing of the photon and exciton dispersion, leading to the formation of two exciton-polariton branches. For $\hbar\omega < \hbar\omega_0$: Lower Polariton branch (*LPB*). For $\hbar\omega > \hbar\omega_T$: Upper polariton branch (*UPB*). Between $\hbar\omega_0$ and $\hbar\omega_T$, light-propagation is forbidden, as the real part of the dielectric function is < 0 in this region. The parabolic function of the exciton dispersion can be estimated to be a constant for small values of k.

speaking, which type of particle can couple to the light field depends on the optical frequency ω of the field, as well as the response of the polarization of the material, mediated by the dielectric function $\epsilon(\omega)$.

For the case of light passing through a semiconductor, photons can couple to an exciton if the photon energy lies in energetic proximity of the exciton resonance (c.f. Chap. 1.1), which results in the formation of exciton-polaritons [94, 113]. The consequences of this coupling for the optical properties of a semiconductor can be calculated qualitatively from a simple classical physics approach [31]: The relation of the wave vector of an electromagnetic field in matter ($\mathbf{k}$) and vacuum ($\mathbf{k_v}$) is given by:

$$\mathbf{k}^2 = \tilde{n}^2(\omega)\mathbf{k_v}^2 \quad \text{or} \quad k^2 = \tilde{n}^2(\omega)k_v^2 \tag{1.12}$$

Here, $\tilde{n}$ is the previously introduced complex index of refraction, given by Eq. (1.3). Eq. (1.12) consequently reads:

$$\epsilon(\omega) = \frac{c^2 k^2}{\omega^2} \tag{1.13}$$

This equation is commonly referred to as the polariton-equation [31].

With the help of this identity, it is possible to derive the dispersion $\omega(k)$ of the system in energetic proximity of the polariton, once the dielectric function of the participating quasi-particles is known. For the case of exciton-polaritons, the dispersion can be calculated by inserting the dielectric function of the exciton resonance,

given by Eq. (1.2), into the polariton-equation:

$$\epsilon(\omega) = \epsilon_b + \frac{f}{\omega_0^2 - \omega^2 - i\gamma\omega} = \frac{c^2 k^2}{\omega^2} \tag{1.14}$$

This finding can now be used to plot the influence of the strong light-matter coupling on the exciton dispersion in a band structure picture, which is qualitatively shown in Fig. 1.3. In this graph, the steep dotted line represents the linear dispersion of photons, with the slope being equivalent to the speed of light in the semiconductor. The horizontal dotted line at ω_0 marks the exciton dispersion. The exciton dispersion is parabolic (c.f. Eq. (1.1)) but can be treated as a constant for the small value of k that is related to the photon dispersion. Due to the strong coupling of the photon and the exciton, the dispersion relations cannot cross. Correspondingly, an anticrossing is seen, which involves the formation of two distinct branches of the exciton-polariton dispersion, denoted as upper polariton branch (UPB) and lower polariton branch (LPB).

Between the two frequencies ω_T and ω_0, light propagation is suppressed, since the real part of the dielectric function has a negative sign in this region that corresponds to an absorption of the light as a consequence of the resonance at ω_0 (c.f. Fig. 1.2). The initial splitting of ω_0 and ω_T can be calculated, if sufficient information on the dielectric function is given, following the Lyddane-Sachs-Teller relation [31, 115]:

$$\frac{\epsilon_s}{\epsilon_b} = \frac{\omega_L^2}{\omega_0^2} > 1 \tag{1.15}$$

Here, the constant ϵ_s is introduced, which denotes the approximately static value of the dielectric function $\epsilon(\omega)$ well below ω_0.

One particularly interesting consequence of the anticrossing that accompanies the exciton-polariton formation is the fact that the dispersion relations are considerably flat in energetic proximity of the resonances. Accordingly, the exciton-polariton dispersion is dominated by the excitonic part of the quasi-particle in this region. As the group velocity of a wave-packet that passes through a medium is given by $v_g = \frac{\partial \omega}{\partial k}$, the flat dispersion can reduce the group velocity by several orders of magnitude [95, 116, 117] down to typical speeds of sound [118]. Consequently, a light pulse with a photon energy close to $\hbar\omega_0$ or $\hbar\omega_T$ that propagates through the semiconductor material experiences a significant delay of up to 1 ns even for samples with thicknesses on the order of hundreds of micrometers or below [96, 97, 103].

While this slow light propagation is not the primary matter of interest, it is still beneficial for the experiments regarded in this thesis, as it enhances the interaction

time of a laser pulse with the semiconductor material that it passes through. There-
fore, the influence of certain exciton-polariton-related effects on a probe pulse in a
pump-probe scheme is enhanced.

The next section aims to discuss which mechanisms are involved when the exciton
resonance is manipulated in all-optical experiments.

1.4   Optical Manipulation of the Exciton-Polariton

As stated above, the dispersion of the exciton-polariton has two distinct branches.
However, only the lower polariton branch will be addressed in the experiment. Due
to the exciton-likeness of the LPB in the energetic proximity of the resonance, it
will be sufficient for most of the discussion to treat the exciton-polariton resonance
as an exciton resonance with the addition of having higher interaction times due to
the slow-light propagation of the exciton-polariton.

As the experiment aims to exploit the related highly nonlinear interaction in
order to manipulate a weak ultrafast pulse that passes through the material with a
pulse of much higher intensity in a pump-probe kind configuration (c.f. Chap. 2.1),
it is instructive to describe the temporal dynamics of the exciton-polariton in more
detail.

As a starting point, it may be helpful to recall the general time-dependence of
an optically excited polarization in a medium. If an ultrafast laser pulse is incident
on a semiconductor with a central photon energy ω_0 that matches, e.g., an excitonic
resonance energy, the light will be resonantly absorbed. Each absorbed photon will
then create an exciton, which followingly results in an oscillating polarization P of
the sample. If the system will be left to itself, the polarization will subside because
the excitons that add to the polarization undergo various scattering events or the
electron and hole will eventually recombine. The decay of the polarization can be
characterized by the dephasing time T_2:

$$P(\tau) = A \exp\left(-\frac{\tau}{T_2}\right) \sin(\omega_0 \tau) \tag{1.16}$$

This dephasing process is also called free induction decay (FID). Here, $\tau = 0$ denotes
the moment of excitation of the polarization, i.e., the time when the pump pulse hits
the surface of the sample. When the Fourier transform of Eq. (1.16) is calculated,
the resulting function is of the form of a Lorentzian resonance curve similar to
Eq. (1.2). Consequently, the width of the curve after the Fourier transform is given
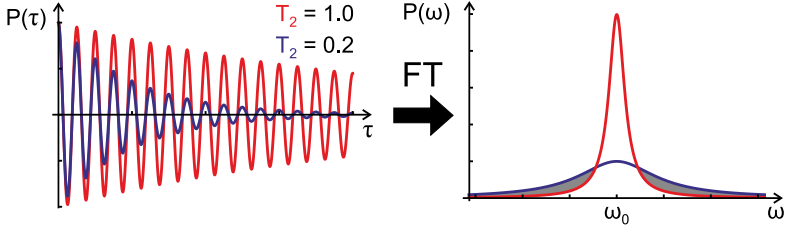by the dephasing time T_2.

Figure 1.4: Left side: Time-dependent oscillating polarization according to Eq. (1.16) for long and short coherence times T_2, shown as red and blue solid lines, respectively. Here, the blue line represents the case of an elevated excitation density. Right side: Corresponding polarization in the frequency domain, obtained by Fourier transformation. The grey area marks the regime, where the resonance broadening for shorter coherence time leads to an increase in absorption.

Attention should be paid to the fact that the terminology of lifetimes, coherence times, and dephasing times, which has been introduced in the first part of this thesis, does not apply to the exciton polarization. Related to the hierarchy of the different time constants (c.f. Eq. 1.11), in the present context, the dephasing time T_2 is addressed as it implicitly covers any equilibration process that leads to a loss of the observable polarization. Correspondingly, the term *dephasing* will be used to refer to the loss of an oriented polarization inside the material irrespective of the underlying microscopic processes.

Excitation Induced Dephasing (EID) and Excitation Induced Shift (EIS)

For the experimental configuration used in the present study, an increase in pump power leads to an increased optical injection of free hot carriers into the semiconductor material by means of two-photon absorption. These additional carriers will consequently influence the behavior of the initial exciton resonance, while mainly two effects can be distinguished, which are called excitation induced dephasing (EID) and excitation induced shift (EIS).

Excitation induced dephasing is the effect that the increased excitation density of bound or unbound electron-hole pairs leads to an enhancement of the dephasing rate or, in other terms, to a shorter dephasing time T_2 [101]. Owing to the interplay

of the increased scattering rates due to the higher amount of carriers, as well as dynamical screening of the Coulomb potential caused by the charged carriers, an initially oriented polarization will dephase on a shorter time scale.

Looking at this change of the dynamics of the polarization function in the time-domain yields a picture as shown in Fig. 1.4, left side. Here, the blue curve represents the case of higher excitation densities and a consequential decrease of the coherence time T_2, compared to the case of lower excitation densities, shown as a red solid line. In this model graph, the difference in the dephasing times is chosen to be a factor of five.

Calculating the Fourier transform of these functions now directly allows for the observation of changes of the corresponding resonance in the frequency domain, as depicted on the right hand side of Fig. 1.4. As intuitively expected, the increased dephasing of the resonance leads to a flattening of the resonance curve and consequently to a reduced absorption at the resonance frequency ω_0, since the polarization determines how the light-field can couple to the semiconductor. However, to the sides of the resonance frequency, the increased spread of the blue curve leads to the formation of areas, where the coupling of the electromagnetic field to the material is increased. Therefore, the excitation of free carriers can lead to an increased absorption in an experimental configuration where the probe beam of a pump-probe measurement is situated on the low-energy flank of the exciton resonance.

It is noteworthy that this picture is of course insufficient to fully explain the influence of EID on the absorption, since the actual dependence of the absorption on the dielectric function of the resonance is more complicated (c.f. Eq. (1.8)). However, this approach should suffice as a proof-of-principle kind of explanation in order to interpret the experimental data in the later chapters of this thesis.

Excitation induced shift   is another effect that can result from an enhanced optical excitation. While the process of EID is relatively easy to understand by means of Fourier transform, EIS is less intuitive to describe in this simple picture, although the effect originates from the same sources [102]. Phenomenologically, the increase of scattering between the carriers leads to an alteration of the Coulomb potential of the electron and hole in the exciton, which induces a change of the exciton binding energy and consequently also a shift of the resonance energy. Typically, the resonance frequency is reduced for increasing excitation densities, which is in detail, however, also a question of the sample temperature [119]. As will be shown later, no clear indication of EIS is found within the experimental investigation carried out

in this thesis. Therefore, the effect is treated as a side note in the present chapter and is not discussed in further detail.

Perturbed Free Induction Decay (PFID)

So far, the dependence of the free induction decay on the manipulation of the de-phasing time T_2 has been discussed primarily. Now, the influence of an abrupt perturbation to the amplitude of the oscillating polarization is addressed, such as in the case where an intense laser pulse interacts with a previously oriented polarization. This effect, called perturbed free induction decay (PFID), can be observed in pump-probe measurements at negative delays when a resonance, such as an exciton resonance, is probed [120].

Again, this effect can be treated phenomenologically in a simple way by comparing the temporal evolution of the polarization $P(\tau)$ with the resonance spectrum in the frequency domain $P(\omega)$. To model the perturbation, a Heaviside function is introduced to Eq. (1.16), which corresponds to a complete truncation of the polarization due to the perturbation at a certain time τ_p:

$$P(\tau) = A \exp\left(-\frac{\tau}{T_2}\right) \sin(\omega_0 \tau) \Theta(\tau - \tau_p) \tag{1.17}$$

In figure 1.5, left side, this function is shown graphically. Analogous to the discussion of the EID, the right-hand side of Fig. 1.5 shows the corresponding Fourier transform and therefore the resonance lineshape in the frequency domain. Here, the red curve depicts the unperturbed case, as in Eq. (1.16). For the blue curve, which corresponds to the perturbed case, the initial peak amplitude is lowered. Most strikingly, oscillations occur to the sides of the resonance frequency. In general, these fringes exhibit a trend of decreasing interfringe spacing for increasing τ_p. However, the effect simultaneously vanishes in amplitude, as the initially oriented polarization dephases with T_2.

In a pump-probe kind of experiment, however, the pump pulse usually induces the initial oscillating polarization at $\tau = 0$, which is then ideally only probed by the much weaker probe pulse. In order to understand the appearance of pump-probe signals at negative delays, one has to consider the polarization of the sample that is induced by the absorption of the probe pulse itself: When the probe beam passes through the sample, it gets partially absorbed and excites a polarization, which starts to oscillate. Subsequently, this oscillating polarization again adds up to the electric field of the probe beam after a certain time delay by means of dipole radiation. At negative delay times τ, when the pump hits the sample subsequent
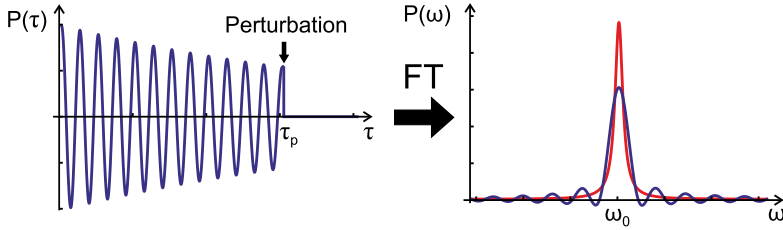
Figure 1.5: Left side: Time-dependent oscillating polarization according to Eq. (1.17), with a perturbation occurring at $\tau = \tau_p$. Right side: Corresponding polarization in the frequency domain, obtained from Fourier transform. The red solid line marks the case for an unperturbed free induction decay as shown in Fig. 1.4. The blue curve exhibits oscillations to the sides of the resonance frequency due to the perturbation of the oscillating polarization.

to the probe, the pump beam can interfere with the electric field created by the polarization that originates from the absorption of the probe beam.

It is also possible to explain the PFID in the picture of quasi-particles: A slowly propagating exciton-polariton, which is initially launched by the probe beam, gets surpassed by a much faster pump photon[2] and both quasi-particles interact. Since the pump photon then indirectly influences the probe signal compared to the case when no pump photon is present, this interaction induces a pump-probe signal at negative delay times.

This effect can also be seen in the spectrally resolved phase of the pulse and can be observed experimentally by using field-resolved spectroscopy techniques [121]. In such a case, the real part of the dielectric function exhibits oscillations similar to those of the imaginary part (c.f. Fig. 1.5, right side).

---

[2]This case can occur for an experimental configuration, where, e.g., the probe photon energy is close to the exciton resonance and the pump photon energy is located well below this energy.

Chapter 2

Experimental Methods and Sample Characterization

The experiments conducted in the present second part of this thesis once more rely on ultrafast laser pulses to observe transient phenomena. The time-resolution is again realized with a pump-probe measurement scheme, as has been presented in Chap. 2.3. In addition to spectrally integrated time-resolved measurements, a monochromator is included in the setup to study the transient behavior of individual spectral components. In detail, the ultrafast dynamics of the lower exciton-polariton branch is studied for two specimens of a $Cd_{0.88}Zn_{0.12}Te$ crystal with varied thicknesses of $208\,\mu$m and $75\,\mu$m. The following chapter aims to provide detailed insight into the experimental configuration in Chap. 2.1 and how the experimental results are obtained from the raw data (Chap. 2.2). A characterization of the utilized samples is given in Chap. 2.3.

2.1   Experimental Setup

In order to study the ultrafast dynamics of the lower polariton branch in CdZnTe, a conventional pump-probe setup is used, as depicted in Fig. 2.1. In the present case the optical source is given by the Ti:sapphire regenerative amplifier as noted in Chap. 2.4, which possesses the parameters summarized in Tab. 2.1. The laser source delivers $\sim 40\,$fs pulses centered at $1.55\,$eV photon energy. The RegA is adjusted to a repetition rate of $230\,$kHz in order to obtain a slightly higher pulse energy.

In contrast to the previous measurements of part I, no degenerate pump-probe configuration is used here: A fraction of the pulse train emitted by the regenerative amplifier serves as a pump pulse. The remainder is fed into the optical parametric
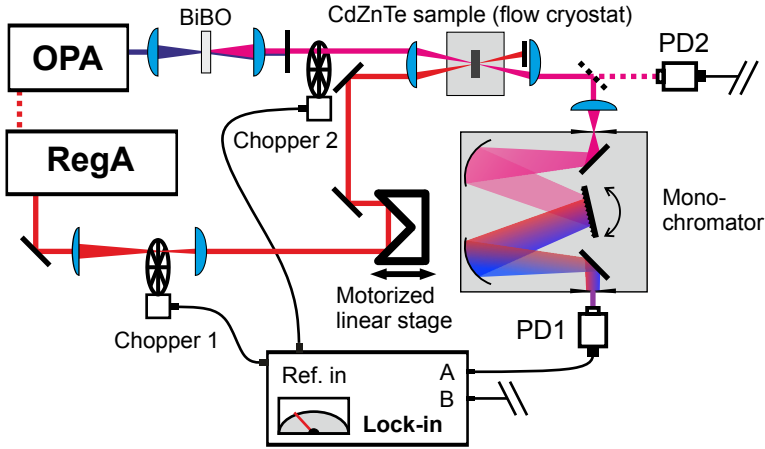
Figure 2.1: Schematic experimental setup for the detection of ultrafast transient phenomena in CdZnTe. The time-resolved pump-probe study can be performed in a spectrally integrated or spectrally resolved manner by solely utilizing a photodiode, or combining the photodiode with a monochromator, respectively.

amplifier (OPA) to generate near-infrared pulses of 60 fs duration and 0.8 eV central photon energy, which serve as broadband probe pulses. In order to probe the lower polariton branch of the $Cd_{0.88}Zn_{0.12}Te$ sample, the OPA output is focused into a BiBO (Bismuth Barium Borate) crystal to obtain the second harmonic frequency. Subsequently, the remaining fraction of the fundamental pulse is blocked with a low-pass wavelength filter. The pump beam passes an additional optical path to compensate the elongated beam path in the OPA, which the probe pulses have to undergo.

Analogous to the experiments outlined earlier in this thesis, a motorized linear stage is used to fine-tune the pump-probe delay. Both pump and probe are focused onto the sample in a non-collinear way, which allows for an easy blocking the pump beam after the excitation of the sample. Relatively large focal diameters of the pump and probe beams are chosen, which both possess values of $\sim 200\,\mu$m in the sample plane. The transmission of the probe beam is subsequently analyzed either in a spectrally integrated manner or spectrally dispersed in a monochromator of ~ 1 meV resolution.

The analysis of transient transmission changes relies on lock-in analysis utilizing two lock-in amplifiers referenced to a $\sim 2.4\,\mathrm{kHz}$ modulation of the excitation beam, as well as a modulation of the probe beam with frequencies of $\sim 400\,\mathrm{Hz}$. This configuration facilitates the simultaneous monitoring of the absolute transmission of the probe beam, as well as the relative transmission changes induced by the pump beam. This concurrent measurement technique will be described in more detail in Chap. 2.2. The investigated samples are $208\,\mu\mathrm{m}$ and $75\,\mu\mathrm{m}$ thick slabs of a [100]-oriented $Cd_{0.88}Zn_{0.12}Te$ crystal with a background p-type doping on the order of $10^{15}\,\mathrm{cm}^{-3}$, which is kept in a flow cryostat at T $\sim 8\,\mathrm{K}$. Further details on the investigated sample will be given in Chap. 2.3.

2.2 Measurement Scheme

As has been pointed out in the previous section, the present experimental configuration allows for a simultaneous measurement of the absolute transmission T of the probe beam, as well as relative transmission changes ΔT induced by the pump beam. The advantage of doing so lies in the fact that instabilities of the laser power can be synchronously monitored and subtracted from the signal. As a consequence, data recorded at different dates can be compared more consistently. A parallel measurement of T and ΔT from the same photodiode signal requires the use of two lock-in amplifiers, which correspondingly requires the use of two distinct modulation frequencies. One therefore has to pay close attention to the evaluation of the data.

Two optical choppers are used for the individual beams, with a lower modulation frequency for the probe beam and a faster modulation of the pump beam. As a result, the time dependence of the diode voltage U shows a behavior as schematically shown in Fig. 2.2.

As evident from the picture, the pump induces a small change in the probe transmission from the level U_2 to U_1. The first lock-in amplifier, which works with the faster frequency $f_{\Delta T}$, detects the difference between the voltage levels U_2 and U_1. However, as the integration time of the lock-in is on the order of hundreds of milliseconds, the signal is also averaged over the probe modulation cycles. As a consequence, the corresponding signal detected by the first lock-in amplifier is reduced by a factor of two:

$$U_{\mathrm{LI1}} = \frac{U_2 - U_1}{2} \propto \frac{1}{2}\Delta T \tag{2.1}$$
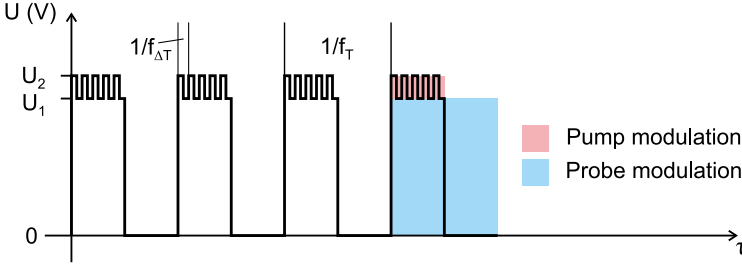
Figure 2.2: Schematic time dependence of the diode voltage in a pump-probe configuration with two modulation frequencies f_T and $f_{\Delta T}$. The modulation frequencies are chosen to be a factor of ten apart from each other for this schematic description.

Simultaneously, the second lock-in amplifier detects the difference of the signal levels that correspond to the on- and off-state of the slower frequency modulation of the probe beam. However, as evident from the schematic in Fig. 2.2, during the on-phase of the probe modulation, the voltage level at the photo diode is periodically altered by the simultaneously chopped pump beam. Consequently, the signal at the second lock-in reads:

$$U_{\text{LI2}} = \frac{U_2 + U_1}{2} \propto T + \frac{1}{2}\Delta T \tag{2.2}$$

To obtain the relative changes in transmission, one therefore has convert the lock-in signals in the following way:

$$\frac{\Delta T}{T} = \frac{2U_{\text{LI1}}}{U_{\text{LI2}} - U_{\text{LI1}}} \tag{2.3}$$

Ideally, the modulation frequencies are chosen to fulfill $f_T \ll f_{\Delta T}$. In this approximation, the obtained data are not influenced by interference effects that can be caused by the different modulation frequencies.

2.3   Sample Characterization

The investigated semiconductor material, $Cd_{0.88}Zn_{0.12}Te$, is a direct semiconductor, which crystallizes in a zinc-blende structure. The samples were fabricated by H. Mariette at the Université Grenoble-Alpes in Grenoble, France. In particular, the samples originate from a bulk ingot of $Cd_{0.88}Zn_{0.12}Te$ grown by the Bridgman technique at high temperatures of $1200\,°C$. The crystal specimens were cut to the respective

thicknesses along a [100] surface. Afterwards they were chemical-mechanically polished, resulting in specimens with two different thicknesses of $208\,\mu$m and $75\,\mu$m, respectively. The sample material is not intentionally doped but exhibits a background p-type doping concentration of $10^{15}\,\mathrm{cm}^{-3}$ [103]. The specimens are of the form of small slabs, which are individually clamped into a sample holder. This configuration and the brass material of the sample holder should ensure a reasonable heat transport in order to suppress an unwanted heating of the sample.

In order to classify the experimental configuration energetically, the photon energy spectra of the pump and probe beams are shown in Fig. 2.3. Furthermore, the normalized transmission curve of the material at a temperature of $T = 8\,\mathrm{K}$ is shown as a black, dotted line. The values are obtained experimentally from transmission measurements, utilizing a white-light source and a CCD camera.

On the high energy tail of the probe energy, the nominal energetic positions of the lower and upper polariton resonance are marked with vertical lines. The position of the resonances are extracted from the linear transmission spectrum of the sample and are consistent with previous work on a $745\,\mu$m-thick specimen [103] from the same wafer as the ones used in this thesis.

The probe pulse is centered at $1.594\,\mathrm{eV}$ and covers the entire spectral region from $\sim 1.54\,\mathrm{eV}$ to beyond the lower (LP) and upper (UP) polariton resonances, which are located at $1.6637\,\mathrm{eV}$ and $1.657\,\mathrm{eV}$, respectively. However, as the transmission is negligible for photon energies $> 1.66\,\mathrm{eV}$ (cf. dotted line in Fig. 2.3), no information about the optical transmission can be recorded beyond this photon energy.

The pump pulse is centered at around $1.550\,\mathrm{eV}$ and is therefore clearly located below the excitonic resonance energy of $1.6638\,\mathrm{eV}$ at cryogenic temperatures. Hence, excitation of the sample occurs exclusively via two-photon absorption of the pump pulses. The choice of this excitation scheme also ensures a rather uniform excitation throughout the entire sample depth.

With the help of the formula for two-photon absorption, the resulting excitation density that corresponds to a given average power of the pump beam can be calculated via:

$$I(x) = \frac{I_0}{1 + \beta x I_0} \tag{2.4}$$

Here, I_0 is the initial pump intensity, and $I(x)$ denotes the intensity after a certain pathway x through the material. The parameter β is called the two-photon absorption coefficient. Obviously, from the difference of the residual and the initial intensity $I(x) - I_0$, the excitation density can be calculated, taking into account the repetition rate and the photon energy of the laser.
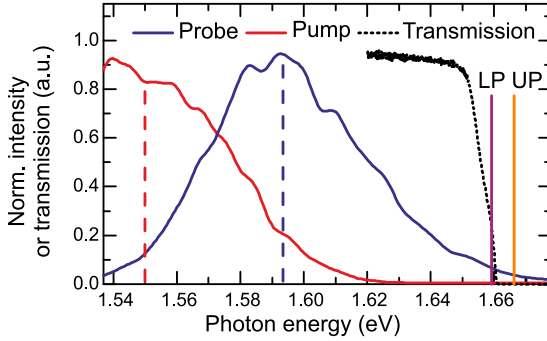
Figure 2.3: Spectra of the utilized pump and probe pulses shown as a red and blue solid line, respectively. The normalized transmission of the $208\,\mu\mathrm{m}$ $\mathrm{Cd}_{0.88}\mathrm{Zn}_{0.12}\mathrm{Te}$ sample is shown as a black, dotted line. Energetic positions of the lower (LP) and upper (UP) polariton resonance are indicated by vertical lines at $\hbar\omega_{\mathrm{LP}} = 1.657\,\mathrm{eV}$ and $\hbar\omega_{\mathrm{UP}} = 1.6637\,\mathrm{eV}$, respectively [103].

Finding exact values for the parameter β can turn out to be difficult, as they depend on the photon energy, as well as the orientation of the crystallographic axes with respect to the excitation beam [122]. From z-scan experiments that use photon energies of $1.165\,\mathrm{eV}$ and laser pulse durations of $40\,\mathrm{ps}$, values for CdTe and ZnTe have been reported to be $\beta = 22\,\mathrm{cmGW}^{-1} - 26\,\mathrm{cmGW}^{-1}$ and $\beta = 4.2\,\mathrm{cmGW}^{-1} - 4.5\,\mathrm{cmGW}^{-1}$, respectively [123, 124]. In the present case of a compound of both of the above-mentioned semiconductors, it is reasonable to assume that the two-photon absorption coefficient lies between the values of the individual materials. However, together with a deviating photon energy and pulse duration, estimating the correct value of β turns out to be difficult. To overcome this uncertainty, β is calculated from a short series of measurements of the pump beam power in front of and behind the cryostat that contains the sample. Consistent with the values reported in [123], the value of β is found to be $\sim 23\,\mathrm{cmGW}^{-1}$ for the present compound material and the given experimental conditions.

Chapter 3

Experimental Results

Within the present chapter, the experimental results on the dynamical response of the lower polariton branch in $Cd_{0.88}Zn_{0.12}Te$ will be discussed. Starting from conventional pump-probe measurements, Chap. 3.1 shows the spectrally integrated time dependence of the differential transmission. In particular, the probe beam located in the energetic vicinity of the lower polariton branch senses the influence of the electron-hole pairs on the exciton-polariton resonance, which are excited by two-photon absorption of the pump beam.

In this context, a power dependence of these measurements can be used to determine which regime of nonlinear interaction is addressed by the excitation. Furthermore, the pivotal pump-probe experiments give insight into the time scales that are involved. With regard to a potential applicability of the material in the context of ultrafast all-optical switching, the latter is of major interest, as it gives rise to the achievable minimal times of the operation.

In a more profound study, Chap. 3.2 provides an analysis of the spectral and temporal dependence of the differential transmission. To gain insight on which fundamental processes are involved in the ultrafast dynamical response of the material, the obtained experimental results are compared with a theoretical model, which is provided by the group of T. Meier in Paderborn [106].

Subsequently, chapter 3.3 aims to analyze the influence of thermal effects on the differential transmission data for high excitation powers. Potential influences of the sample thickness on the induced transmission changes will be addressed in Chap. 3.3.

If not stated otherwise, the presented data originate from measurements performed on the $208\,\mu m$ specimen.

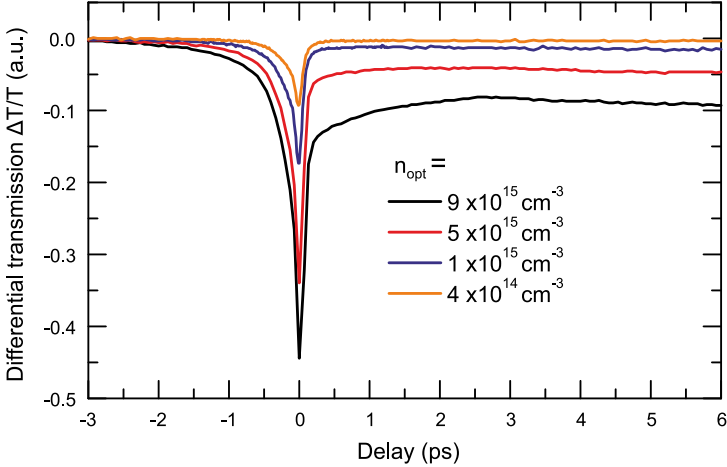## 3.1   Time-Resolved Differential Transmission

Figure 3.1: Spectrally integrated, normalized differential transmission transients for various excitation densities. Signal values at negative delay times are subtracted from the data.

With the help of the setup shown in Chap. 2.1, the differential pump-probe transmission $\Delta T/T$ is recorded, using the $208\,\mu$m-thick $Cd_{0.88}Zn_{0.12}Te$ sample. In the present case, data are recorded with a single photodiode (PD2 in Fig. 2.1), i.e., in a spectrally integrated manner.

Figure 3.1 depicts the differential transmission with respect to the pump-probe delay τ_d for a series of pump excitation densities ranging from $4 \times 10^{14}\,cm^{-3}$ to $9 \times 10^{15}\,cm^{-3}$, corresponding to a pump beam irradiance of $30\,\mu J\,cm^{-2}$ to $190\,\mu J\,cm^{-2}$. Constant values at far negative delays are subtracted from the original data in order to yield the presented curves, accounting for a thermally induced shift, which will be discussed in detail in Chap. 3.3.

In general, the $\Delta T/T$ transients show a pronounced induced absorption for positive delays, as well as a sharp peak in proximity of the pump-probe overlap around $\tau_d = 0$. A substantial suppression of the optical transmission is found even for moderate carrier densities.

For negative pump-probe delays, the pump pulse initially succeeds the probe pulse, where conventionally no effects can be seen that would result from the carrier

injection by the pump beam. However, the signal in Fig. 3.1 at $\tau_d < 0$ occurs due to the slow light propagation of a fraction of the probe beam. In detail, the pump beam does not couple strongly to the exciton resonance, and is therefore transmitted through the material without significant delay. Consequentially, the pump beam passes by a fraction of the probe beam at some point for short negative delays, which creates the signal at these delay times.

In the region of temporal overlap of the pump and probe beam, the simultaneous presence of both beams increases the probability of a probe photon to be absorbed in a two-photon absorption process that includes one pump and one probe photon. Accordingly, the additional absorption probability leads to a reduction of the probe beam transmission.

It is important to note that due to the slow light propagation in the lower polariton branch, the temporal overlap can only be defined at a single position of the sample. Within this study, the temporal overlap at $\tau_d = 0$ is chosen to be at the maximum of the differential transmission transient. As only a small fraction of the probe beam is significantly delayed by the polariton propagation (c.f. Fig. 2.3), it is reasonable to assume that this maximum accords to the situation, when pump and probe beam overlap in time at the sample's front surface.

For increasing positive delay times, a long-lived reduction of the differential transmission can be observed, which can be addressed to a persisting elevated amount of photoexcited carriers. This assumption founds on the involved time scales: the signal does not significantly decay over the temporal region of $\sim 30\,\mathrm{ps}$. Furthermore, the negative differential transmission is not seen for far negative delays, thus indicating a lifetime of the effect smaller than the laser repetition period of $T_{\mathrm{rep}} \sim 4\,\mu\mathrm{s}$. Therefore, the signal decay at positive delays can likely be addressed to carrier recombination.

In order to quantify the dependence of the signal on the excitation conditions in more detail, Fig. 3.2 depicts the dependence of differential transmission $\Delta T/T$ on the excitation density for a fixed positive delay of $\tau_d = 6\,\mathrm{ps}$. The optical excitation densities are calculated from the average power of the pump beam incident on the semiconductor by solely taking into account two-photon absorption with the empirically obtained value of β as discussed in Chap. 2.3. Evident from the linear fit shown as a red solid line in Fig. 3.2, the transient signals scale linearly with the calculated excitation density n_{opt}. As this finding indicates a linear relation of the pump beam intensity and the observed signal, this response can be classed as a $\chi^{(3)}$ process in the terminology of nonlinear optics.
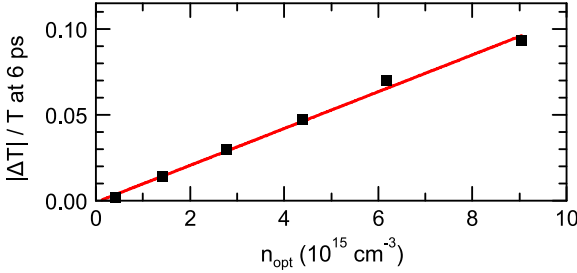
Figure 3.2: Differential transmission detected at a fixed positive pump-probe delay of $\tau_d = 6\,\text{ps}$, as a function of the optical excitation intensity n_{opt}. The black squares indicate data points taken from the same transients as shown in Fig. 3.1. Red solid line is a linear fit to the data.

3.2 Spectrally Resolved Differential Transmission

For a more detailed discussion of the different signal components, the differential transmission spectra are investigated. The present section serves as an overview of the different components that contribute to the overall signal. Each individual aspect will be investigated in more detail in the following sections.

Incorporating the deviations that are caused by heat deposition with high pump powers, the results discussed now are recorded for a fixed, comparatively low excitation density of $1 \times 10^{15}\,\text{cm}^{-3}$, corresponding to a pump average power of $7.6\,\text{mW}$ and an irradiance of $55\,\mu\text{J}\,\text{cm}^{-2}$. The impact of high excitation densities and the consequential heating of the sample is reviewed in Chap. 3.3. As stated before, the nominal temperature of the sample is set to $T = 8\,\text{K}$ by liquid helium cooling inside a flow cryostat.

Figure 3.3 depicts the differential transmission spectra for a series of pump-probe delays ranging from $\approx -20\,\text{ps}$ to $66\,\text{ps}$ for a total of 47 different, non-equidistant pump-probe delays. In particular, the graph depicts the pump-induced transmission changes ΔT normalized on the initial probe transmission T on the z-axis as a colored contour, with respect to the photon energy, given on the x-axis and to the varying pump-probe delay over the span of the y-axis.

On the lower energy tail of the spectra, an area is seen, which seems to show an increasing positive differential transmission. This effect can be attributed to the influence of stray light from the pump beam: Obviously, due to the normalization in order to obtain the differential transmission $\Delta T/T$, these stray light effects get
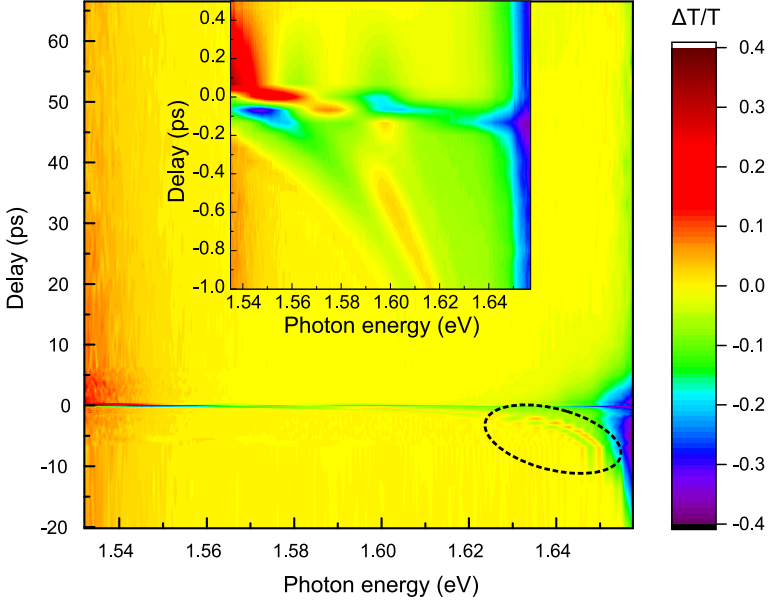
Figure 3.3: Differential transmission spectra for delay times ranging from $-20\,\text{ps}$ to $66\,\text{ps}$ for the $208\,\mu\text{m}$-thick specimen and a pump power of $P_{\text{pump}} \approx 8\,\text{mW}$ ($n = 1 \times 10^{15}\,\text{cm}^{-3}$). The inset depicts the differential transmission in the vicinity of the pump-probe overlap at zero delay for the same spectral range. The encircled area marks the spectral oscillations for negative delay times for clarity.

enhanced in the regions, where the probe spectrum vanishes. Therefore, the persistent increase in $\Delta T/T$ for $\hbar\omega < 1.55\,\text{eV}$ does not originate from the pump-probe measurement, but is an artifact of the data acquisition. The higher energy boundary of the plot, on the other hand, is given by the absorption edge of the material, where no more probe light can pass through the sample (c.f. transmission spectrum in Fig. 2.3).

In the spectral vicinity of the lower polariton resonance at $\sim 1.65\,\text{eV}$, the optical transmission of the probe beam is strongly attenuated by up to $\sim 40\,\%$ within a narrow time frame around the pump beam excitation. This is the case for both positive and negative delays, as already evident from the spectrally integrated results given in 3.1.

For short negative delays, spectral oscillations arise in the region around $1.63\,\mathrm{eV} - 1.65\,\mathrm{eV}$ (encircled area in Fig. 3.3), which show the typical trend of a decreasing interfringe spacing for increasing negative delay. Consequently, these oscillations can be attributed to the perturbed free induction decay (c.f. Chap. 1.4). The majority of the decrease in probe transmission relaxes on a time scale of $\approx 3\,\mathrm{ps}$ and only a minor, residual effect persists on longer time scales owing to the carrier recombination on subnanosecond time scales, visible as a light green trail on the higher energy boundary.

For better visibility, the inset in Fig. 3.3 depicts the differential transmission spectra in a narrow range around the temporal pump-probe overlap, ranging from $-1.0\,\mathrm{ps}$ to $0.5\,\mathrm{ps}$ for the same spectral boundaries. A closer look at the effects around zero delay reveals a complex behavior of the transmission changes on very short time scales of $\sim 200\,\mathrm{fs}$. It is therefore reasonable to assume that these highly pronounced effects relate to the temporal overlap of the pump and probe pulses at the sample surface. An explanatory approach to these effects can be given by cross-phase modulation of both pulses. Due to the co-propagation of both pulses in the regime where the pump and probe spectra overlap (c.f. Fig. 2.3), the individual pulses sense each others influence of the electric field on the nonlinear refractive index of the sample [125]. Eventually, portions of the pump beam can be scattered into the path of the probe beam and vice versa in four-wave mixing type contributions.

In the following, the individual signal components near the lower polariton resonance will be discussed in further detail for positive and negative delays. Moreover, a theoretical approach is presented, which can be used to qualitatively model the observed temporal behavior of the differential transmission spectra.

Theoretical Model

In order to model the experimental data of the differential transmission spectra, A. Trautmann and M. Reichelt from the group of T. Meier in Paderborn provided a theoretical simulation. For the purpose of integrity, this section aims to give insight to the principles of this model as it is presented in [106].

The model itself is based on a χ^3 perturbation expansion [126] of the incoming fields, taking into account excitation-induced dephasing [101] as the dominant optical nonlinearity (c.f. Chap. 1.4). In a simple model, the perturbation of a two-level system results in two linked rate equations (hierarchically structured iterative

equations), which read:

$$\frac{\partial}{\partial t}p_{\text{probe}}^{(1)}(t) = (-i\omega_R - \gamma)p_{\text{probe}}^{(1)}(t) + i\frac{\mu}{\hbar}E_{\text{probe}}(t) \tag{3.1}$$

$$\frac{\partial}{\partial t}\delta p^{(3)}(t) = (-i\omega_R - \gamma)\delta p^{(3)}(t) - \alpha n_{\text{pump}}^{(2)}(t)p_{\text{probe}}^{(1)}(t) \tag{3.2}$$

Here, ω_R is the Rabi-frequency, γ is the dephasing rate, and μ denotes the dipole matrix element. The linear polarization $p_{\text{probe}}^{(1)}(t)$ is driven by the electric field of the probe pulse $E_{\text{probe}}^{(1)}(t)$. Due to the slow light propagation related to the lower exciton-polariton dispersion [103], the linear polarization inside the semiconductor exists for several picoseconds. At a given time τ_p, the pump pulse injects a population of hot carriers via two-photon absorption, which then relaxes or thermalizes exponentially with the time constant T_1 via scattering processes. Consequently, the time-dependence of this non-equilibrium carrier density can be modeled with a function of the form:

$$n_{\text{pump}}^{(2)}(t) = \Theta(t - \tau_p)\exp\left(\frac{t - \tau_p}{T_1}\right) \tag{3.3}$$

Or, to incorporate the finite time δt of the absorption process:

$$n_{\text{pump}}^{(2)}(t) = \frac{1}{2}\left[1 + \tanh\left(\frac{t - \tau_p}{\delta t}\right)\right]\exp\left(\frac{t - \tau_p}{T_1}\right) \tag{3.4}$$

One can now identify the second term in Eq. (3.2) as the EID, which implies the interaction of the excited carrier density on the polarization $\delta p^{(3)}(t)$. Therein, the strength of the nonlinear interaction is mediated via the parameter α. In order to obtain the differential transmission $\delta T(\omega) \propto -\text{Im}\left(\frac{\delta p^{(3)}(t)}{E_{\text{probe}}(\omega)}\right)$, Eq. (3.1) and (3.2) have to be solved numerically.

Due to its energetic positioning far from the lower polariton resonance, the pump beam is treated as to propagate dispersion-free through the sample. However, the probe beam's propagation through the material must be treated numerically in order to include the slow light propagation close to the resonance. In particular, this numerical approach is handled utilizing the finite-difference time-domain (FDTD) method based on the auxiliary differential equation technique [127, 128]. With this model, first the probe field E_{probe} at the rear end of the $208\,\mu$m-thick $\text{Cd}_{0.88}\text{Zn}_{0.12}\text{Te}$ sample is calculated. The resulting, modified field is subsequently applied to Eq. (3.1) and (3.2). Although the interaction along the full length of the crystal is neglected in this approach, it will followingly be seen that the model is able to achieve a good qualitative agreement with the most important aspects of the experimentally observed data.

Differential transmission spectra at positive delay times

As chapter 3.2 has only given a broad overview of the differential transmission spectra, the effects related to the lower polariton resonance are now examined in more detail. Starting with positive pump-probe delay times, the upper panel in Fig. 3.4 provides a selection of differential transmission spectra for different pump-probe delays τ_d, which are horizontal cuts of the data shown in Fig. 3.3.

Shortly after photoexcitation, the optical transmission in the vicinity of the lower polariton resonance is massively attenuated by up to 30 %. This finding can be intuitively attributed to EID. In particular, the resonance gets broadened due to photoexcitation and the absorption extends to lower photon energies, as has been sketched in Fig. 1.4. Consequently, a bigger fraction of the probe beam gets absorbed in this spectral regime compared to the situation when no excitation is present, which leads to the negative differential transmission pump-probe signal.

The black, dashed lines are Lorentzian fits to the data with a central photon energy at the center of the photoluminesence of the lower polariton of 1.657 eV, as it has been reported in [103]. It is important to note that signals related to the upper polariton resonance are not expected to appear in the data because of the high absorption of the material at this energy (c.f. sample transmission in Fig. 2.3). The Lorentzian fits agree well with the experimental values. As an example, at $\tau_d = 0.5$ ps a width parameter of $w_{\mathrm{FWHM}} = 19$ meV is obtained from the fit. For the present experimental data, the central photon energy of the individual fits reveals a negligible influence of excitation induced shift. However, as the experimental values do not cover the maximum of the function, the fit does not feature a high resolution of the exact resonance position.

The induced absorption features in the upper panel in Fig. 3.4 decay on time scales as short as several picoseconds. In particular, exponential fits for individual photon energies reveal decay times ranging from 4.9 ps at 1.65 eV to 1.9 ps at 1.62 eV.

Owing to the timescales involved, the experimentally observed relaxation of the EID-related absorption changes are more likely to result from a thermalization of the highly energetic photogenerated carriers than to a recombination of electron-hole pairs: As typical thermalization times of hot carriers are on the order of hundreds of femtoseconds [129], and the slow-light propagation in the material stretches the effective interaction timespan of the pump and probe beam, it is reasonable to assume that the timescales observed in the present study are in line with carrier thermalization. On the other hand, carrier lifetimes commonly occupy values of several nanoseconds or more in CdTe [130].
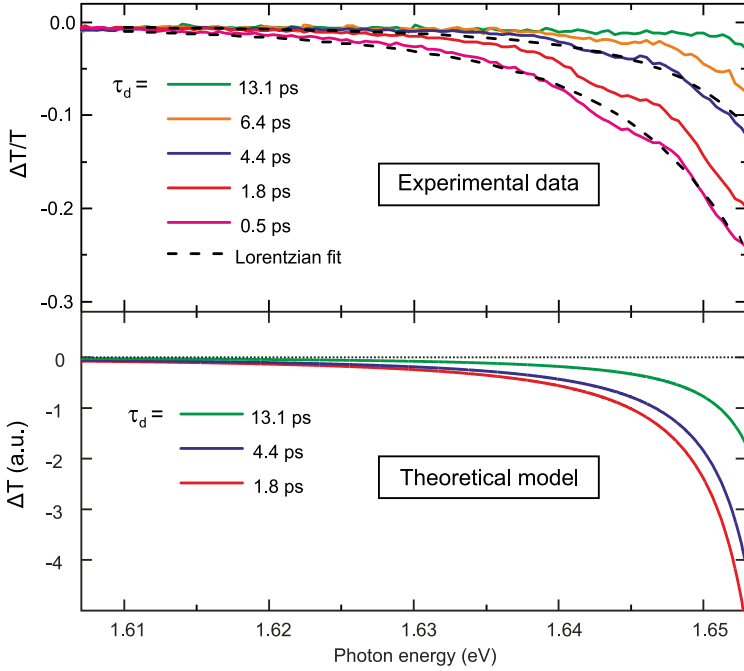
Figure 3.4: Upper panel: Differential transmission spectra for a variety of positive pump-probe delay times $\tau_d > 0$. The depicted data are cuts of the colored contour plot shown in Fig. 3.3. An average pump power of $8\,\mathrm{mW}$ is applied, corresponding to densities of $n = 1 \times 10^{15}\,\mathrm{cm}^{-3}$, or $55\,\mu\mathrm{J\,cm}^{-2}$ irradiance. The dashed lines are Lorentzian fits to the data. Lower panel: Theoretical simulations of the data for a selection of 3 different pump-probe delays, based on the theoretical model depicted in Chap. 3.2, utilizing a lifetime T_1 of $10\,\mathrm{ps}$ (taken from [106]).

The lower panel in Fig. 3.4 shows the results of the theoretical calculations for three different pump-probe delays $\tau_d > 0$. For the present calculated graphs, the relaxation time introduced in Eq. (3.3) is chosen to be $T_1 = 10\,\mathrm{ps}$. While the theoretical model does not provide an exact quantitative measure of the signal amplitudes, it achieves a good qualitative agreement of experiment and theory. Evidently, the induced absorption for higher energies is recovered by the model. The negative sign of the differential transmission underlines the assumption of excitation induced dephasing to be the dominant mechanism. As expected, the overall trend of a most pronounced effect at the smallest pump-probe delay is reproduced by the model, too. In the simulation, this fact is mainly governed by the time T_1, as for increasing τ_d the induced absorption vanishes due to the thermalization of hot carriers, which cause the excitation-induced dephasing.

Differential transmission spectra at negative delay times

Analogous to the discussion on the differential transmission spectra at positive delay times, the corresponding spectra for nominally negative delay times are depicted in Fig. 3.5. Here, the individual plots are successively offset by a value of 0.05 for better visibility.

Starting with the experimental data in the upper panel of the figure, these signals feature spectral oscillations with a period that increases as the delay approaches zero. This finding is indicative of a perturbed free induction decay of the exciton polarization, as discussed in Chap. 1.4.

Moreover, the influence of the EID of the lower polariton resonance is also seen for negative delays, arising at the higher photon energy boundary of the graph. In particular, the spectra change their behavior rather abruptly for increasing photon energies, turning from an oscillating shape to a marked induced absorption.

The time scales on which the oscillations are visible for increasing negative delays point to the coherence time T_2 of the excitonic polarization [120]. However, fitting the closed formula for the PFID to the data is difficult, as the experimental values deviate from the sole PFID behavior due to the excitation induced dephasing, i.e., the onset of the absorption on the photon energy scale. Consequently, for the present case one can only estimate the coherence time from the exponential temporal decay of the transmission changes. For the given temperature and excitation density a value of $T_2 \sim 10\,\mathrm{ps}$ can be estimated for photon energies close to the lower polariton resonance. In detail, however, the value of T_2 that is obtained from the data varies when it is derived from the transients at different photon energies. Nevertheless,
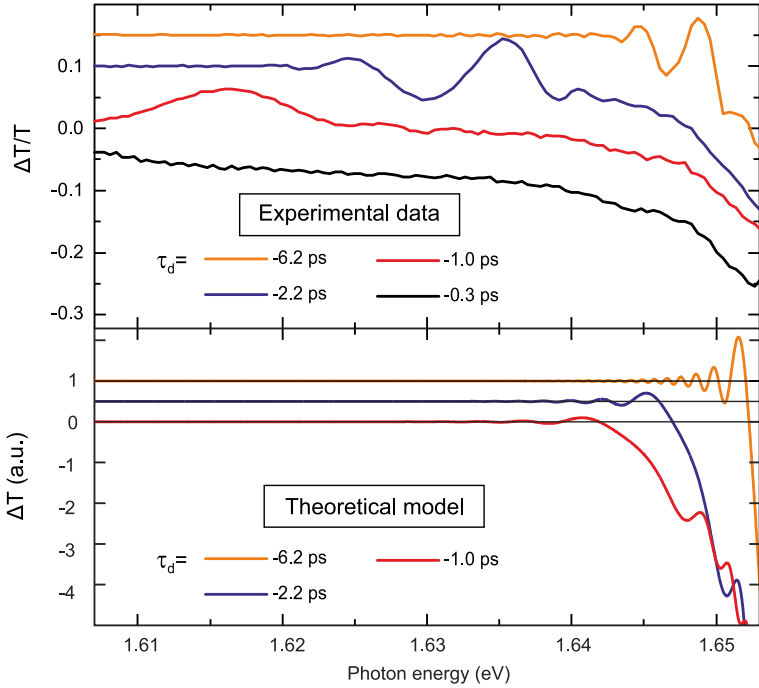
Figure 3.5: Upper panel: Differential transmission spectra for a variety of negative pump-probe delay times $\tau_d < 0$. The depicted data are cuts of the colored contour plot shown in Fig. 3.3. Excitation densities are $n = 1 \times 10^{15}\,\mathrm{cm}^{-3}$, corresponding to $8\,\mathrm{mW}$ average pump power or $55\,\mu\mathrm{J\,cm}^{-2}$ irradiance. Lower panel: Resembling theoretical simulations of the data for a selection of 3 different pump-probe delays, based on the theoretical model outlined in Chap. 3.2, utilizing a lifetime T_1 of $10\,\mathrm{ps}$ (taken from [106]).

the estimation of $T_2 \sim 10\,\mathrm{ps}$ appears to be reasonable, as it corresponds to an inhomogeneous linewidth of $\frac{\hbar}{T_2} = 66\,\mu\mathrm{eV}$, in reasonable agreement with the value of $4\,\mu\mathrm{eV}$ for the homogeneous linewidth, which has been estimated from transmission spectra at lower temperatures ($T = 2\,\mathrm{K}$) [103].

The bottom panel in Fig. 3.5 depicts the corresponding simulations that are obtained from the theoretical model. First of all, the model achieves to reproduce the trend of faster oscillations for increasing $|\tau_d|$. However, the values that are obtained from the experimental data and from the theoretical calculations are considerably larger, compared to the case when only the effect of PFID is considered, where the oscillation period should be $\frac{\hbar}{\tau_d}$.

Another aspect that is covered by the simulations is the marked change from oscillating behavior to induced absorption for high photon energies. In line with the experimental data, the photon energy, at which the transition from one regime to the other occurs, shifts to lower energies for decreasing absolute delays $|\tau_d|$. This shift of the tipping point can be understood considering the slow-light propagation of the probe beam in the proximity of the lower polariton resonance:

As the time that the probe pulse needs to pass through the sample is a function of the photon energy, different frequency components of the broad probe pulse are stretched along the span of the sample. As a consequence, the faster pump beam catches up on different frequency components of the probe beam at different times. This can also be interpreted as an effective frequency-dependent pump-probe delay $\tau_d(\omega)$. Ultimately, the transition from the regime of PFID for nominally negative delay times to the regime of induced absorption by EID for nominally positive delays occurs at different τ_d for the respective frequency components. In other terms, a nominal delay $\tau_d < 0$ at the face of the sample can effectively switch sign after a certain propagation distance, depending on the photon energy.

The effective frequency-dependent $\tau_d(\omega)$ also influences the differential transmission for nominally positive delays in a way that the pump-probe delay becomes effectively larger. Furthermore, the highly pronounced dependence of the group velocity on the photon energy can also explain the much larger oscillation periods in the frequency domain, compared to the intuitively expected case for a single resonance [120].

3.3   Impact of Strong Excitation

So far, the results have already shown that a drastic change of absorption on the order of $\sim 40\,\%$ can be applied to the probe beam by means of excitation induced
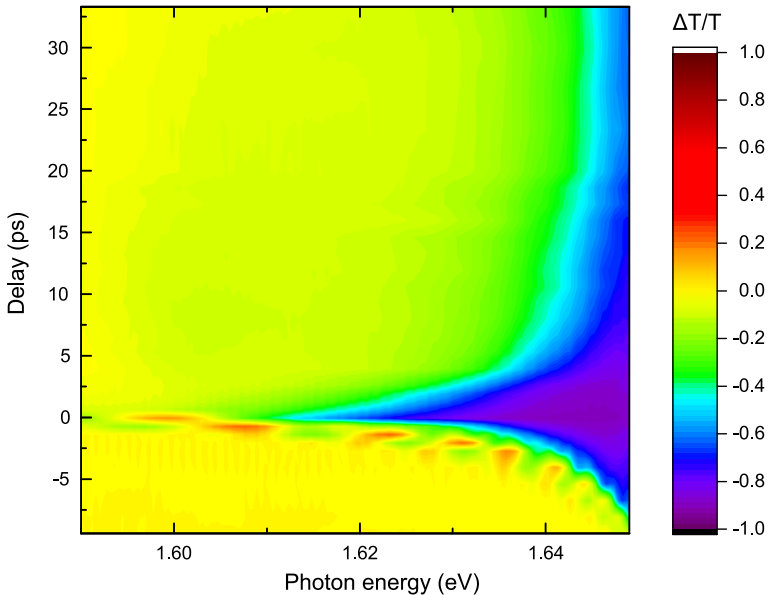
Figure 3.6: Differential transmission spectra for delay times ranging from $-9\,\mathrm{ps}$ to $33\,\mathrm{ps}$ for the $208\,\mu\mathrm{m}$-thick $\mathrm{Cd}_{0.88}\mathrm{Zn}_{0.12}\mathrm{Te}$ specimen and a pump power of $P_{\mathrm{pump}} \approx 26\,\mathrm{mW}$ ($n = 9 \times 10^{15}\,\mathrm{cm}^{-3}$).

dephasing of an exciton-polariton resonance. As outlined in the introduction, from a technological point of view the induced ultrafast absorption changes shown in the previous section might be interesting for the perspective of utilizing the effect for ultrafast all-optical switches. Consequently, the question arises to what extent the effect of induced absorption can be enhanced by driving the excitation conditions to higher levels.

In Fig. 3.6, the differential transmission spectra are shown as a colored contour plot for a data set that contains 32 different pump-probe delay times τ_d ranging from $-9\,\mathrm{ps}$ to $33\,\mathrm{ps}$. The results are again discussed for the $208\,\mu\mathrm{m}$ $\mathrm{Cd}_{0.88}\mathrm{Zn}_{0.12}\mathrm{Te}$ sample. In this case, however, an increased pump beam power of $26\,\mathrm{mW}$ is used, corresponding to a photoexcited density of hot carriers of $9 \times 10^{15}\,\mathrm{cm}^{-3}$ and an irradiance of $190\,\mu\mathrm{J}\,\mathrm{cm}^{-2}$.
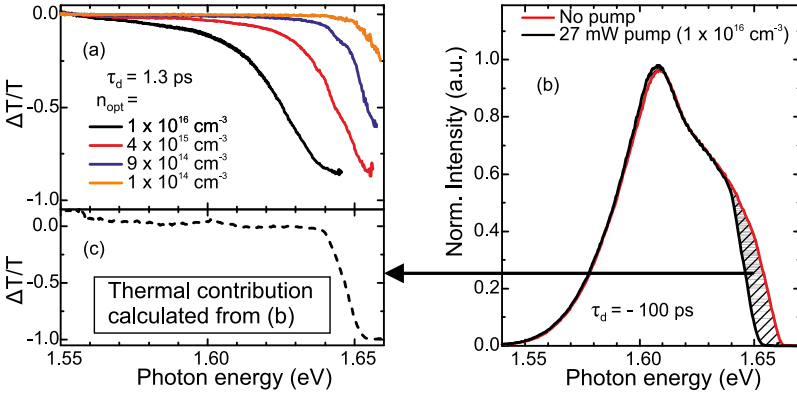
Figure 3.7: (a) Differential transmission spectra for various excitation densities and a fixed delay of $\tau_d = 1.3$ ps. (b) Normalized transmitted probe spectra taken with (red curve) and without (black curve) an excitation of $200\,\mu\mathrm{J\,cm^{-2}}$ irradiance at a negative delay of $\tau_d = -100$ ps. (c) Thermal contribution to the differential transmission calculated from the difference of the transmitted spectra in panel (b).

At first glance, the picture features the same effects and looks very similar to the data shown for the case of the lower excitation power of 7.6 mW in Fig. 3.3. Yet, in the present case the induced absorption related to the lower polariton resonance is seen to be much stronger, nearly fully depleting the probe beam transmission around $\tau_d = 0$ (mind the different z-scales in Fig. 3.3 and Fig. 3.6). This finding is intuitively expected, since an increasing amount of hot carriers increases the effect of EID. Most remarkably, spectral regions around 1.63 eV can be identified, where a switching of the probe beam absorption on the order of 90 % takes place on ultrashort time scales as short as several picoseconds.

On the high energy boundary of the plot, however, the involved time scales turn out to be much longer, as evident from the persistent increase in absorption for the whole range of pump-probe delays. The long-lived effects likely relate to a shift of the lower polariton resonance frequency, which does not significantly relax on the given range of delay times. From the involved time scales it is reasonable to assume that the origin of this occurrence is to some extent given by thermal effects, i.e., a resonance shift caused by heating of the sample due to the pump beam irradiation, rather than an a purely excitation induced shift.

In order to study the how the presumably thermal effects that cause the persistent suppression of the optical transmission seen in Fig. 3.6 influence the overall response of the material, the transmission spectra are now probed for a series of different excitation powers at a fixed positive delay of $\tau_d = 1.3\,\mathrm{ps}$. The corresponding experimental data of $\Delta T/T$ are shown in Fig. 3.7 for four different excitation powers ranging from $2\,\mathrm{mW}$ to $27\,\mathrm{mW}$, corresponding to a density range of $1 \times 10^{14}\,\mathrm{cm}^{-3}$ to $1 \times 10^{16}\,\mathrm{cm}^{-3}$, and an irradiance of $15\,\mu\mathrm{J\,cm}^{-2}$ to $200\,\mu\mathrm{J\,cm}^{-2}$.

As already evident from the data for high excitation densities seen in Fig. 3.6, large transmission changes up to a virtually complete suppression of the optical transmission can be observed. The shift of the resonance frequency and the corresponding cut-off at the high energy boundary appears to commence at excitation densities of $\approx 9 \times 10^{14}\,\mathrm{cm}^{-3}$ ($\approx 8\,\mathrm{mW}$ pump). For the highest utilized pump power, already a $\sim 20\,\mathrm{meV}$ broad range of the probe beam transmission is entirely suppressed.

In order to validate the assumption that the persistent signal components of Fig. 3.6 originate from thermal effects, the absolute probe transmission is detected at a far negative delay time, where the imprints of the PFID have subsided, and only the effects caused by the previous pump pulse(s) persist. In this case, the nominal negative delay corresponds to an effective pump-probe delay on the order of the laser repetition period of $\approx 4\,\mu\mathrm{s}$.

The experimental result of this study is depicted in panel (b) of Fig. 3.7, showing the absolute probe spectrum detected with and without excitation as a black and red solid line, respectively. The relaxation from the black to the red solid line, which corresponds to the switching from the excited to the non-excited operational state, can manually be observed to occur on time scales of several seconds.

By analyzing the difference between the two spectra, shown as a hatched gray area, it is now possible to extract the thermal contribution to the differential transmission. The result of this calculation is depicted in panel (c) and shows that even for the present moderate excitation densities, thermally induced band-gap shifts of $\sim 10\,\mathrm{meV}$ and corresponding transmission changes are observed. Therein, the residual changes in differential transmission in the whole observable spectral range are likely caused by a slight shift of the laser spectrum during the time of the two measurements that are depicted in panel (b).

The findings of this study point towards a poor thermal contact in the flow cryostat of the setup. Partially evident from the data, a critical pump power for the influence of thermal effects is observed, which can be identified to be $\sim 8\,\mathrm{mW}$. As

indicated earlier, the pump power of 7.6 mW was therefore chosen for the study of the PFID and EID effects in Chap. 3.2.

Assuming a thermal shift of the fundamental band gap of the semiconductor to be the dominant underlying mechanism of the shift of the absorption edge, the corresponding actual sample temperature could be derived from the temperature dependence of the band gap, given by the Varshni equation [131]:

$$E_g(T) = E_g(T = 0) - \alpha \frac{T[K]^2}{T[K] + \beta}(eV) \tag{3.5}$$

Literature values of the Varshni parameters $E_g(T = 0) = 1.668\,\text{eV}$, $\alpha = 6.48 \times 10^{-4}\,\text{eV/K}$, and $\beta = 264\,\text{K}$ can be found for $Cd_{0.9}Zn_{0.1}Te$ [132, 133]. As only relative shifts of the band gap are discussed here, and the parameters α and β do not strongly depend on the exact composition, the deviations caused by the difference of 2% compared to $Cd_{0.88}Zn_{0.12}Te$ can be neglected. According to Eq. (3.5), a thermal shift of the resonance of $10\,\text{meV} - 20\,\text{meV}$ corresponds to an effective increase in sample temperature of $\Delta T = 75\,\text{K}$ to $110\,\text{K}$. This is of course a rough estimate, as the energetic shift observed in this study could be altered by thermal effects on the exciton binding energy and by a thermal broadening of the resonance.

Evident from the data depicted in Fig. 3.3 and Fig. 3.6, not only a thermally induced increase in absorption occurs for higher excitation powers, but also a shift of the region of the ultrafast dynamical response towards lower photon energies. As the limits of achievable excitation powers have been covered by the data, the question arises if the shift of the dynamical response can also be achieved by increasing the temperatures inside the flow cryostat. From a technological perspective, this concept is interesting, as it may give rise to a spectral tunability of the switching functionality of the material. However, a comprehensive measurement of the differential transmission's dependence on the photon energy, time delay, and temperature is difficult to realize because of the vast increase in the time needed for the data acquisition. Therefore, the sole probe transmission spectra are recorded for varying sample temperatures as a test of a potential spectral tunability.

In Fig. 3.8, normalized probe transmission spectra are shown for temperatures ranging from $\approx 10\,\text{K}$ to $110\,\text{K}$. More specifically, the high energy flanks of the spectra are depicted, with a dashed line indicating where $10\,\%$ of the maximum intensity is reached.

As evident from the data, the absorption edge of the probe spectrum undergoes a pronounced red-shift of $\approx 60\,\text{meV}$ for an increase in temperature of $100\,\text{K}$. A straight-forward analysis of the intersection points of the dashed line with the spectra gives rise to the temperature dependence of the shift. In Fig. 3.9, the obtained results
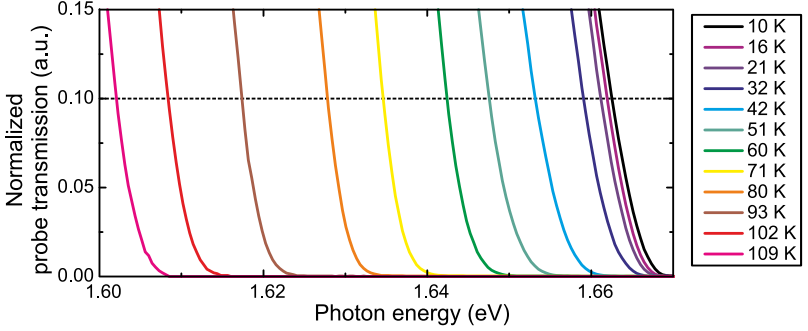
Figure 3.8: Normalized probe transmission spectra after passing through the 208 μm-thick $Cd_{0.88}Zn_{0.12}Te$ sample for a range of temperatures of 10 K to 109 K. High energy flanks of the probe beam transmission are shown to indicate the absorption edge of the sample. The dashed line marks the 10 % level of the normalized transmission as a guide to the eye.

are shown as black circles, marking the individual 10 % levels of the absorption edge for the range of available temperatures. The red solid line is a fit to the data according to the Varshni equation (3.5).

The Varshni parameters that are obtained from the fit are summarized in Tab. 3.3. In order to compare the obtained parameters with the literature values for the band gap shift, the table also features the Varshni parameters for $Cd_{0.9}Zn_{0.1}Te$, given by [132]. Apparently, the Varshni parameters for the shift of the absorption edge significantly differ from the ones that are given for the shift of the band gap of $Cd_{0.9}Zn_{0.1}Te$. This finding is indicative of an additional effect adding to the contribution of the band gap on the thermal shift of the absorption edge. Such a contribution could emerge from a broadening of the linewidth of the exciton resonance, i.e., from a thermally induced dephasing. However, the clarification of this matter requires further investigation.

Ultimately, from the experimental results it is now possible to give a better estimate of the effective temperature for the case of high excitation powers, as discussed in the context of Fig. 3.7. Using the experimental results on the temperature dependence of the absorption edge, as seen in Fig. 3.9, a shift of 10 meV to 20 meV corresponds to an increase of the initial temperature from $T = 8$ K to $T = 42$ K $- 60$ K.
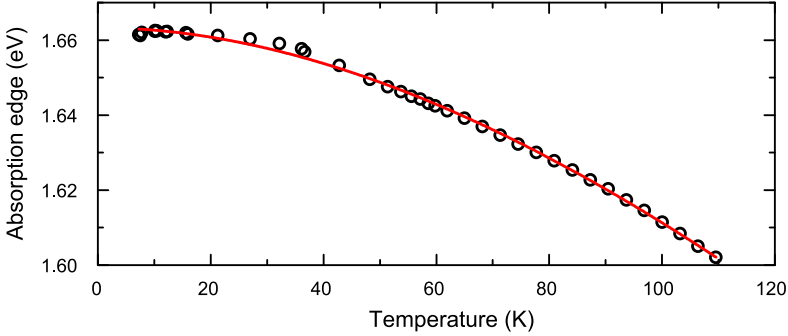
Figure 3.9: Temperature dependence of the absorption edge, derived from probe transmission spectra (c.f. Fig. 3.8), shown as black circles. The red solid line is a fit to the data according to the Varshni formula, given in Eq. (3.5), relating the observed shift in absorption to a shift of the band gap.

	E_0 [eV]	α [meV K^{-1}]	β [K]
$Cd_{0.88}Zn_{0.12}Te$ absorption edge (fit)	1.6633 ± 0.0003	2.5 ± 0.4	374 ± 77
$Cd_{0.9}Zn_{0.1}Te$ band gap [132]	1.668	0.648	264

Table 3.1: Fit parameters obtained from a fit of the Varshni formula (Eq. (3.5)) to the temperature shift of the absorption edge of the $Cd_{0.88}Zn_{0.12}Te$ sample, as seen in Fig. 3.9. Results of the fit are compared with literature values for the Varshni parameters of the band gap for $Cd_{0.9}Zn_{0.1}Te$, according to [132].

3.4   Influence of the Sample Thickness

In order to evaluate the potential scalability of the ultrafast switching that has been shown in the previous sections, the influence of the sample thickness on the signal strength of the pump-probe signals is studied. To this end, the differential transmission spectra are probed for both of the available $Cd_{0.88}Zn_{0.12}Te$ specimens with respective thicknesses of $75\,\mu m$ and $208\,\mu m$.

To rule out the influence of heating from the pump beam irradiance, the pump powers are chosen to be as low as $\approx 2.5\,mW$, taking into account the expected lower threshold power for heat deposition in the thinner sample. In particular, the powers and corresponding excitation densities are $P_{75} = 2.24\,mW$, $n_{75} = 1.5 \times 10^{14}\,cm^{-3}$, and $P_{208} = 2.14\,mW$, $n_{208} = 1.3 \times 10^{14}\,cm^{-3}$. Therefore, differences of
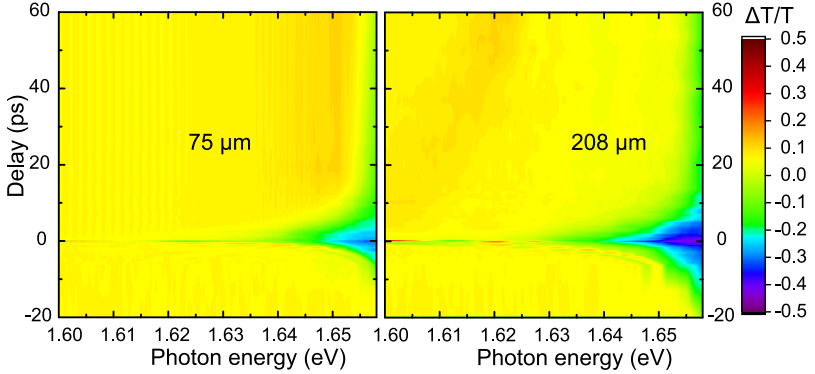
Figure 3.10: Differential transmission spectra for delay times ranging from $-20\,\text{ps}$ to $60\,\text{ps}$ for the $75\,\mu\text{m}$-thick (left side) and $208\,\mu\text{m}$-thick specimen (right side). Both data sets are taken with comparable, low pump powers of $P_{\text{pump}} \approx 2.5\,\text{mW}$ at a nominal temperature of $T = 8\,\text{K}$.

the excitation conditions are negligible. The experimental data obtained from the differential transmission pump-probe study are depicted in Fig. 3.10.

The results of the individual specimen both exhibit the main features that have already been discussed in the previous sections, e.g., EID close to the lower polariton resonance, as well as PFID for negative delay times. In detail, the maximum values of $\Delta T/T$ are found to be ≈ 0.32 for the $75\,\mu\text{m}$ sample, and ≈ 0.46 for the case of the $208\,\mu\text{m}$ sample, respectively.

As intuitively expected, in the sample with higher thickness the suppression of the transmission can be seen to be slightly stronger, owing to the higher interaction length. This finding further confirms the uniformity of the induced carrier excitation along the crystal length, as for a non-uniform excitation, where the major fraction of carriers is induced in the vicinity of the sample's surface, the sample thickness should have a much less pronounced influence on the differential transmission.

In the depiction of the experimental data on the differential transmission of the $75\,\mu\text{m}$ sample, two additional, subsidiary signal components become apparent: Firstly, a spectrally oscillating feature can be observed for the whole range of positive delays on the left side of Fig. 3.10 for photon energies of $1.60\,\text{eV} - 1.645\,\text{eV}$. In fact, these oscillations have already influenced the differential transmission spectra in Fig. 3.6 at negative delays. From an analysis of the respective oscillation peri-

ods, these features can be identified to be Fabry-Pérot oscillations occurring in the sample.

Secondly, a minor positive differential transmission of the probe beam can be seen occurring for energies slightly below the region, where the induced absorption takes place. This signal component is seen for elevated pump-probe delays τ_d, as evident from the arising patch of orange color around $\sim 1.65\,\mathrm{eV}$ in Fig. 3.10, left side. The occurrence of this positive signal component might be related to Pauli-blocking of the phonon replica of the exciton-polariton resonances (c.f. [103]). However, for an undoubted explanation of this subsidiary effect, an experimental study in reflection geometry would be needed in order to map the contribution of the upper-polariton branch.

Other discrepancies of the experimental findings for the different sample thicknesses might be related to varying heat contact, as well as a different diffusion of the heat deposited on the surface of the sample. Moreover, the cooling of the samples with different thicknesses inside the cryostat might lead to a different strain of the crystals that consequently might alter the optical properties.

3.5   Conclusion and Outlook

Within the second part of this thesis, the dynamics of the ultrafast nonlinear optical response of the lower exciton-polariton branch in $Cd_{0.88}Zn_{0.12}Te$ are investigated, based on a pump-probe type all-optical study utilizing non-degenerate femtosecond laser pulses. As a sample material, two specimen with thicknesses of $208\,\mu m$ and $75\,\mu m$ from the same crystal of the II-VI compound semiconductor are utilized.

By means of two-photon absorption of the pump pulse train located at $1.55\,eV$, rather uniform excitation conditions are achieved with a maximum excitation density of $n_{opt} \approx 1 \times 10^{16}\,cm^{-3}$.

In a first, spectrally integrated study of the time-dependent differential transmission $\Delta T/T$, the overall probe beam transmission is found to be suppressed down to $\sim 40\,\%$ for the highest excitation density. In a more profound analysis, the spectral dependence of the transient data is recorded, giving insight to the ultrafast dynamics related to the lower polariton branch in a spectral window of $\sim 1.54\,eV$ to $1.66\,eV$ with a maximum pump-probe delay ranging from $\tau_d = -20\,ps$ to $60\,ps$.

Markedly different features of the differential transmission data are experimentally observed at positive and nominally negative delay times. By comparing the experimental results with model simulations provided by M. Reichelt et al. [106], the observed signal components can be addressed to their respective underlying mechanisms. In particular, for positive delay times, the signal is dominated by an excitation induced dephasing of the lower polariton resonance, which is found to relax on time scales of several picoseconds. For nominally negative pump-probe delays, spectrally oscillating features are identified, originating from a perturbed free induction decay of the exciton-polariton resonance.

As another result from the comparison of experiment and theory, the pump beam is found to surpass certain spectral components of the probe beam for nominally negative delay times, owing to the reduction of the group velocity in the vicinity of the lower polariton as reported in [103]. Ultimately, the features seen for $\tau_d < 0$ can be attributed to result from an interplay of PFID and EID. On the contrary, no excitation induced shift of the polariton resonance is found to influence the dynamic response.

A central issue of the experimental study was to find out to what extent and under which conditions the ultrafast dynamic response of the lower-polariton resonance can be used to achieve an all-optical switching functionality. Even at intermediate excitation densities of $n_{opt} \approx 1 \times 10^{15}\,cm^{-3}$, the excitation induced dephasing can be used to severely manipulate the probe beam transmission for spectral components

close to the LP resonance, leading to a suppression of $\sim 40\,\%$ of the initial transmission. Most remarkably, increasing the excitation density to $n_{\mathrm{opt}} \approx 1 \times 10^{16}\,\mathrm{cm}^{-3}$ drives the suppression of the probe beam up to a complete shut-off of a spectral window of $\sim 20\,\mathrm{meV}$ that relaxes on several picoseconds.

In the regime of high excitation conditions, a component of the differential transmission signal is seen to add up to the overall signal, which persists on much longer time scales of several seconds and is thus identified to originate from heat deposition of the pump beam onto the sample. While the corresponding signal component does not directly improve the potential ultrafast switching functionality of the material, it opens up the perspective to tune the spectral position of the resonance and therefore also the ultrafast response of the material by means of temperature.

To test the potential tunability of the resonance by a variation of the temperature, the shift of the absorption edge of the material is observed for a sole temperature increase inside the cryostat with no pump beam excitation. As a result, a spectral shift of $\approx -60\,\mathrm{meV}$ for a temperature variation of $6\,\mathrm{K}$ to $100\,\mathrm{K}$ is found. While this already points to a spectral tunability of the ultrafast switching, ongoing experiments need to provide a comprehensive analysis of the temperature dependence of the transient differential transmission spectra in order to fully varify this assumption.

In order to investigate the physical origin of the observed temperature shift, a Varshni function is fit to the temperature dependence of the absorption edge of the material. By comparing the obtained Varshni parameters for $Cd_{0.88}Zn_{0.12}Te$ to those corresponding to the band gap shift of $Cd_{0.9}Zn_{0.1}Te$, indications are found that the thermal shift is not solely related to the shift of the band gap energy of the material but may contain contributions of a spectral broadening of the exciton-polariton resonance.

Studying the scaling of the dynamic response of the material for varying sample thicknesses and similar excitation densities, the differential transmission changes are revealed to be more pronounced in the sample with higher thickness, as intuitively expected due to the higher interaction pathway. However, for a functioning logical device the thickness of the material must be chosen as a compromise of desired effect amplitude, excitation powers and heat transfer, as well as miniaturization capability.

The results obtained from the experiments in this part of the thesis open up interesting possibilities regarding potential all-optical switching methods. It has been demonstrated that it is indeed possible to macroscopically switch the transmission of a probe beam on picosecond time scales, up to a full depletion of the transmission in a spectral window of $\sim 20\,\mathrm{meV}$ at cryogenic temperatures.

So far, relatively high laser pulse powers were used that are not featured in commercially applicable lasers. Consecutive studies towards this topic are therefore likely to focus on finding optimized configurations of the utilized energy spectra of the pump and probe beams with respect to the sample material in order to enhance the efficiency of the ultrafast switching process. Moreover, the temporal pulse widths and the thickness of the material offer room for optimization, which is ought to be addressed in ongoing experiments.

Further investigations on the choice of the utilized semiconductor structures should also focus to drive the presented optical manipulation scheme to be feasible on room temperatures. It is thinkable that this approach could be potentially realized in future studies by applying the presented method to strongly confining or low-dimensional structures, which allow for a non-vanishing room-temperature exciton-polariton polarization. In this context, the implementation of the presented optical manipulation scheme on a nanostructure platform might as well help to realize elevated effective interaction lengths, possibly allowing to achieve a macroscopic all-optical manipulation with the utilization of less complex laser systems.

The experiments conducted within this thesis have not covered the impact of the excitation and heating on the time delay related to the reduction of group velocity on the lower polariton branch. Future experiments should therefore aim to combine time-of-flight measurements with the pump-probe technique at varying external pump conditions. As an induced ultrafast shift of the polariton resonance leads to a spectrally dependent alteration of the delay of light passing through the semiconductor material, such a study might help to provide a novel technique of all-optical tuning of optical delays. As a long-term perspective, the concurrent manipulation of a spectral shift together with the dephasing of the resonance offers the possibility to achieve switching and delay-tuning functionality within the same component. To this end, configurations need to be found that allow to address both aspects individually, i.e., heating and carrier injection need to be proven to be separately approachable.

Summary

Within this thesis, two markedly different aspects of ultrafast carrier dynamics in semiconductors are addressed in all-optical studies based on pump-probe measurements with femtosecond laser pulses. Both parts of the presented study aim to contribute to the fundamental understanding of the respective physical processes and to foster the applicability of the corresponding semiconductor systems in the context of spintronics and quantum computing or all-optical switching, respectively.

With regard to a potential future applicability of indirect semiconductors in the context of spintronics or quantum computing, the first part of the present work provides an in-depth analysis of spin dynamics in the indirect semiconductor material germanium. Founding on previously published work, the present study provides contributions to the understanding of the efficiency of the spin injection and readout process and their spectral dependencies, as well as the temporal limitations of the carrier spin ensemble coherence.

By comparing Faraday rotation amplitudes normalized on the sheet density of photoexcited carriers, an analysis of the spectral dependence of Faraday Rotation measurements for holes and electrons in germanium is given for a spectral range of $0.75\,\mathrm{eV}$ to $1.03\,\mathrm{eV}$. The interpretation of the empirical study identifies two possible mechanisms for the dependencies on the pump and probe photon energies. By comparing the individual results of the different carrier types, however, indications are found that allow to attribute the observed trends to a spectral dependence of the spin injection process rather than to a spectral dependence of the spin detection via the Faraday effect. Within this context, improvements of the experimental configuration are proposed for future studies that might dissolve this ambiguity.

Additionally, in a separate approach that addresses the temporal limitations of the spin ensemble lifetimes T_s and coherence times T_2^* in bulk Ge, this thesis provides experimental results based on the resonant spin amplification technique. In contrast to conventional time-resolved Faraday rotation, this method facilitates the indirect detection of spin lifetimes for comparatively low magnetic fields of several millitesla by measuring the linewidth of resonance peaks arising from the interfer-

ence of spin ensembles induced by subsequent pump pulses. By rapidly scanning these resonance peaks occurring at different amplitudes of the magnetic field, the experimental findings reveal a detailed temperature trend of these time constants and contribute to the understanding of the onset of spin-ensemble decoherence effects for low magnetic fields.

Addressing one of the central aspects of the present work that aims to elucidate to what extent the spin lifetimes in indirect semiconductors can be enhanced, elevated spin lifetimes of up to 65 ns are found at intermediate temperatures of 50 K. Based on the empirical observations, this study suggests Elliott-Yafet relaxation as the dominant relaxation mechanism and identifies the trends observed for lower temperatures to result from impurity scattering. In line with theoretical predictions [26], the utilization of ultrapure germanium is therefore identified as a key improvement towards even more elevated spin lifetimes. Ultimately, a discussion is given towards other future improvements and the observed experimental findings are classified in the context of comparable studies of actual research.

The second part of this thesis investigates the dynamical nonlinear optical response of the lower exciton-polariton resonance. Motivated by the prospect of all-optical switching functionality, the question is addressed, to what extent the accompanying highly nonlinear interaction induced by a high power pump pulse can be utilized to macroscopically manipulate the transmission of a second probe pulse on ultrashort time scales. The compound II-VI semiconductor $Cd_{0.88}Zn_{0.12}Te$ is used as sample material with two specimens of varying sample thicknesses on the order of $100\,\mu m$.

With the assistance of an externally provided theoretical model and model calculations, different fundamental contributions to the experimentally observed dynamic response of the system are identified in a spectrally resolved, time-dependent study. As a result, contributions of excitation induced dephasing and the perturbed free induction decay are demonstrated to dominate the transient dynamics for positive, and nominally negative delay times, respectively. As expected, traces of the spectrally dependent slow-light propagation related to the reduced group velocity dispersion in vicinity of the lower polariton resonance energy are found to further contribute to the differential transmission changes of the probe beam.

Investigating the all-optical switching functionality, a marked induced suppression of the probe beam transmission is seen even for comparatively low excitation conditions. In detail, the optically induced excitation densities of $n_{opt} \approx 1 \times 10^{15}\,cm^{-3}$ lead to a reduction of the probe transmission by 40 % for spectral components in the vicinity of the lower-polariton resonance. As a key result of the

study, a complete optically induced shut-off of a spectral window of $\sim 20\,\mathrm{meV}$ of the probe beam that subsides on tens of picoseconds is achieved by increasing the optical excitation density to $n_{\mathrm{opt}} \approx 1 \times 10^{16}\,\mathrm{cm}^{-3}$.

For the elevated excitation conditions, the study provides an analysis of contributions from heat deposition onto the sample. In a more profound temperature-dependent study, shifts of the absorption edge of the sample are monitored, which point towards a potential spectral tunability of the optical switching by means of temperature.

Regarding potential future applicability, the thesis proposes objectives of succeeding research. Therein, the combination of time-of-flight measurements with a pump-probe scheme is pointed out to be vital for a most profound understanding of the involved dynamics.

Bibliography

[1] E. G. Uhlenbeck and S. Goudsmit, "Ersetzung der Hypothese vom un-mechanischen Zwang durch eine Forderung bezüglich des inneren Verhaltens jedes einzelnen Elektrons", *Die Naturwissenschaften* **13** (1925), 953–954, DOI: `10.1007/BF01558878`

[2] W. Gerlach and O. Stern, "Der experimentelle Nachweis der Richtungsquantelung im Magnetfeld", *Zeitschrift für Physik* **9** (1922), 349–352, DOI: `10.1007/BF01326983`

[3] M. Julliere, "Tunneling between ferromagnetic films", *Physics Letters A* **54** (1975), 225–226, DOI: `10.1016/0375-9601(75)90174-7`

[4] I. Žutić, J. Fabian, and S. Das Sarma, "Spintronics: Fundamentals and applications", *Rev. Mod. Phys.* **76** (2004), 323–410, DOI: `10.1103/RevModPhys.76.323`

[5] A. Fert, "Nobel Lecture: Origin, development, and future of spintronics", *Rev. Mod. Phys.* **80** (2008), 1517–1530, DOI: `10.1103/RevModPhys.80.1517`

[6] S. A. Wolf et al., "Spintronics: A Spin-Based Electronics Vision for the Future", *Science* **294** (2001), 1488–1495, DOI: `10.1126/science.1065389`

[7] B. Schumacher, "Quantum coding", *Phys. Rev. A* **51** (1995), 2738–2747, DOI: `10.1103/PhysRevA.51.2738`

[8] D. P. DiVincenzo, "The Physical Implementation of Quantum Computation", *Fortschritte der Physik* **48** (2000), 771–783

[9] V. M. Agranovich et al., eds., *Optical Orientation*, **8**, Elsevier Science Publishers B.V., 1984

[10] W. Happer, "Optical Pumping", *Rev. Mod. Phys.* **44** (1972), 169–249, DOI: `10.1103/RevModPhys.44.169`

[11] A. Kastler, "Optical Methods of Atomic Orientation and of Magnetic Resonance", *J. Opt. Soc. Am.* **47** (1957), 460–465, DOI: 10.1364/JOSA.47.000460

[12] J. Shah, *Ultrafast Spectroscopy of Semiconductors and Semiconductor Nanostructures*, ed. by Manuel Cardona et al., **115**, Springer Berlin Heidelberg, 1999

[13] J. M. Kikkawa and D. D. Awschalom, "Resonant Spin Amplification in n-Type GaAs", *Phys. Rev. Lett.* **80** (1998), 4313–4316, DOI: 10.1103/PhysRevLett.80.4313

[14] R. I. Dzhioev et al., "Low-temperature spin relaxation in n -type GaAs", *Phys. Rev. B* **66** (2002), 245204, DOI: 10.1103/PhysRevB.66.245204

[15] S. Ghosh et al., "Room-temperature spin coherence in ZnO", *Applied Physics Letters* **86**, 232507 (2005), DOI: 10.1063/1.1946204

[16] M. Althammer et al., "Spin transport and spin dephasing in zinc oxide", *Applied Physics Letters* **101**, 082404 (2012), DOI: 10.1063/1.4747321

[17] J. M. Kikkawa et al., "Room-Temperature Spin Memory in Two-Dimensional Electron Gases", *Science* **277** (1997), 1284–1287, DOI: 10.1126/science.277.5330.1284

[18] T. Guettler et al., "Optical polarization relaxation in $In_xGa_{1-x}As$-based quantum wells: Evidence of the interface symmetry-reduction effect", *Phys. Rev. B* **58** (1998), R10179–R10182, DOI: 10.1103/PhysRevB.58.R10179

[19] J. A. Gupta et al., "Spin coherence in semiconductor quantum dots", *Phys. Rev. B* **59** (1999), R10421–R10424, DOI: 10.1103/PhysRevB.59.R10421

[20] M. Paillard et al., "Spin Relaxation Quenching in Semiconductor Quantum Dots", *Phys. Rev. Lett.* **86** (2001), 1634–1637, DOI: 10.1103/PhysRevLett.86.1634

[21] A. Greilich et al., "Mode Locking of Electron Spin Coherences in Singly Charged Quantum Dots", *Science* **313** (2006), 341–345, DOI: 10.1126/science.1128215

[22] G. Lampel, "Nuclear Dynamic Polarization by Optical Electronic Saturation and Optical Pumping in Semiconductors", *Phys. Rev. Lett.* **20** (1968), 491–493, DOI: 10.1103/PhysRevLett.20.491

[23] G. G. Macfarlane et al., "Fine Structure in the Absorption-Edge Spectrum of Ge", *Phys. Rev.* **108** (1957), 1377–1383, DOI: 10.1103/PhysRev.108.1377

[24] C. Hautmann, B. Surrer, and M. Betz, "Ultrafast optical orientation and coherent Larmor precession of electron and hole spins in bulk germanium", *Phys. Rev. B* **83** (2011), 161203, DOI: `10.1103/PhysRevB.83.161203`

[25] C. Hautmann and M. Betz, "Magneto-optical analysis of the effective *g* tensor and electron spin decoherence in the multivalley conduction band of bulk germanium", *Phys. Rev. B* **85** (2012), 121203, DOI: `10.1103/PhysRevB.85.121203`

[26] P. Li, Y. Song, and H. Dery, "Intrinsic spin lifetime of conduction electrons in germanium", *Phys. Rev. B* **86** (2012), 085202, DOI: `10.1103/PhysRevB.86.085202`

[27] J. L. Cheng et al., "Theory of optical spin orientation in silicon", *Phys. Rev. B* **83** (2011), 165211, DOI: `10.1103/PhysRevB.83.165211`

[28] T. Paschen, "Ultraschnelle Spindynamik in Germanium", MA thesis, Technische Universität Dortmund, 2013

[29] J. Lohrenz et al., "Optical tailoring of electron and hole spin polarization in bulk germanium", *Proc. SPIE* **8984** (2014), 898418, DOI: `10.1117/12.2037597`

[30] J. Lohrenz, T. Paschen, and M. Betz, "Resonant spin amplification in intrinsic bulk germanium: Evidence for electron spin lifetimes exceeding 50 ns", *Phys. Rev. B* **89** (2014), 121201, DOI: `10.1103/PhysRevB.89.121201`

[31] C. Klingshirn, *Semiconductor Optics*, Springer Berlin Heidelberg, 2005

[32] M. I. Dyakonov et al., eds., *Spin Physics in Semiconductors*, Springer Berlin Heidelberg, 2008

[33] M. Grundmann, *The Physics of Semiconductors*, Springer Berlin Heidelberg, 2006

[34] J. Rioux and J. E. Sipe, "Optical injection and control in germanium: Thirty-band $\mathbf{k} \cdot \mathbf{p}$ theory", *Phys. Rev. B* **81** (2010), 155215, DOI: `10.1103/PhysRevB.81.155215`

[35] C. Kittel, *Introduction to Solid State Physics*, John Wiley and Sons, 2004

[36] E. J. Loren et al., "Hole spin relaxation and intervalley electron scattering in germanium", *Phys. Rev. B* **84** (2011), 214307, DOI: `10.1103/PhysRevB.84.214307`

[37] X. Q. Zhou, H. M. van Driel, and G. Mak, "Femtosecond kinetics of pho-
      toexcited carriers in germanium", *Phys. Rev. B* **50** (1994), 5226–5230, DOI:
      10.1103/PhysRevB.50.5226

[38] D. W. Bailey and C. J. Stanton, "Calculations of femtosecond differential
      optical transmission in germanium", *Journal of Applied Physics* **77** (1995),
      2107–2115, DOI: 10.1063/1.358786

[39] F. Pezzoli et al., "Spin and energy relaxation in germanium studied by spin-
      polarized direct-gap photoluminescence", *Phys. Rev. B* **88** (2013), 045204,
      DOI: 10.1103/PhysRevB.88.045204

[40] C. Rinaldi et al., "Wide-range optical spin orientation in Ge from near-
      infrared to visible light", *Phys. Rev. B* **90** (2014), 161304, DOI: 10.1103/
      PhysRevB.90.161304

[41] M. Faraday, "Experimental Researches in Electricity. Nineteenth Series",
      Philosophical Transactions of the Royal Society of London **136** (1846), 1–20,
      DOI: 10.1098/rstl.1846.0001

[42] S. Sugano et al., eds., *Magneto-Optics*, Springer Berlin Heidelberg, 2000

[43] F. Bloch, "Nuclear Induction", *Phys. Rev.* **70** (1946), 460–474, DOI: 10.
      1103/PhysRev.70.460

[44] G. Slavcheva and P. Roussignol, *Optical Generation and Control of Quan-
      tum Coherence in Semiconductor Nanostructures*, Springer Berlin Heidelberg,
      2010

[45] L. Langer et al., "Access to long-term optical memories using photon echoes
      retrieved from semiconductor spins", *Nature Photonics* **8** (2014), 851–857,
      DOI: 10.1038/nphoton.2014.219

[46] Y. Yafet, *g Factors and Spin-Lattice Relaxation of Conduction Electrons*,
      ed. by F. Seitz and D. Turnbull, **14**, Academic Press, 1963, pp. 1–98, DOI:
      10.1016/S0081-1947(08)60259-3

[47] R. J. Elliott, "Theory of the Effect of Spin-Orbit Coupling on Magnetic
      Resonance in Some Semiconductors", *Phys. Rev.* **96** (1954), 266–279, DOI:
      10.1103/PhysRev.96.266

[48] M.W. Wu, J.H. Jiang, and M.Q. Weng, "Spin dynamics in semiconductors",
      Physics Reports **493** (2010), 61–236, DOI: 10.1016/j.physrep.2010.04.
      002

[49] M. I. D'yakonov and V. I. Perel, *Fiz. Tverd. Tel.* **13** (1971), 3581, [Sov. Phys. Solid State 13, 3023 (1972)]

[50] M. Heidkamp, "Spin-Coherence and -Dephasing of Donor and Free Conduction Band Electrons across the Metal-Insulator Transition in Si:GaAs", PhD thesis, RWTH Aachen, 2004

[51] J. Lohrenz, "Ultraschnelle feldaufgelöste Spektroskopie optischer Nichtlinearitäten in CdTe und Quarzglas", MA thesis, Technische Universität Dortmund, 2012

[52] C. Hautmann, "Ultrafast Spin Dynamics in Semiconductors: A Comparative Optical Analysis of Direct and Indirect Materials", PhD thesis, Technische Universität München, 2012

[53] M. E. Levinshteĭn, S. L. Rumyantsev, and M. Shur, *Handbook Series on Semiconductor Parameters: Volume 1*, World Scientific, 1996

[54] H. R. Philipp and E. A. Taft, "Optical Constants of Germanium in the Region 1 to 10 eV", *Phys. Rev.* **113** (1959), 1002–1005, DOI: `10.1103/PhysRev.113.1002`

[55] R. P. Seysyan, A. V. Varfolomeev, and B. P. Zakharchenya, *Fiz. Tekh. Poluprov.* **2** (1968), 1276, [Sov. Phys. Semicond. 2, 1069 (1969)]

[56] Ioffe Physico- Technical Institute, *Electronic archive: New Semiconductor Materials. Characteristics and Properties*, 2016, URL: `http://www.ioffe.ru/SVA/NSM/`, Accessed May 23, 2016

[57] L. M. Roth and B. Lax, "*g* Factor of Electrons in Germanium", *Phys. Rev. Lett.* **3** (1959), 217–219, DOI: `10.1103/PhysRevLett.3.217`

[58] L. M. Roth, "g Factor and Donor Spin-Lattice Relaxation for Electrons in Germanium and Silicon", *Phys. Rev.* **118** (1960), 1534–1540, DOI: `10.1103/PhysRev.118.1534`

[59] G. Nilsson and G. Nelin, "Phonon Dispersion Relations in Ge at 80 K", *Phys. Rev. B* **3** (1971), 364–369, DOI: `10.1103/PhysRevB.3.364`

[60] S. I. Novikova, *Sov. Phys. Solid State* **2** (1960), 37–38

[61] C. Guite and V. Venkataraman, "Measurement of Electron Spin Lifetime and Optical Orientation Efficiency in Germanium Using Electrical Detection of Radio Frequency Modulated Spin Polarization", *Phys. Rev. Lett.* **107** (2011), 166603, DOI: `10.1103/PhysRevLett.107.166603`

[62] M. M. Glazov et al., "Effect of pump-probe detuning on the Faraday rotation and ellipticity signals of mode-locked spins in (In,Ga)As/GaAs quantum dots", *Phys. Rev. B* **82** (2010), 155325, DOI: 10.1103/PhysRevB.82.155325

[63] M. Wesseli and M. Betz, "Analyzing nonequilibrium carrier distributions with spectrally resolved femtosecond Faraday rotation", *Phys. Rev. B* **76** (2007), 073201, DOI: 10.1103/PhysRevB.76.073201

[64] R. R. Alfano, *The Supercontinuum Laser Source*, Springer New York, 2016

[65] C. Guite and V. Venkataraman, "Temperature dependence of spin lifetime of conduction electrons in bulk germanium", *Applied Physics Letters* **101**, 252404 (2012), DOI: 10.1063/1.4772500

[66] J. Fabian and S. Das Sarma, "Spin relaxation of conduction electrons", *Journal of Vacuum Science & Technology B* **17** (1999), 1708–1715, DOI: 10.1116/1.590813

[67] P. P. Debye and E. M. Conwell, "Electrical Properties of N-Type Germanium", *Phys. Rev.* **93** (1954), 693–706, DOI: 10.1103/PhysRev.93.693

[68] C. M. Wolfe, G. E. Stillman, and W. T. Lindley, "Electron Mobility in High Purity GaAs", *Journal of Applied Physics* **41** (1970), 3088–3091, DOI: 10.1063/1.1659368

[69] A. Giorgioni et al., "Valley-dependent spin polarization and long-lived electron spins in germanium", *Applied Physics Letters* **105** (2014), 152404, DOI: 10.1063/1.4898078

[70] P. Li et al., "Anisotropy-Driven Spin Relaxation in Germanium", *Phys. Rev. Lett.* **111** (2013), 257204, DOI: 10.1103/PhysRevLett.111.257204

[71] C. Jacoboni et al., "Electron drift velocity and diffusivity in germanium", *Phys. Rev. B* **24** (1981), 1014–1026, DOI: 10.1103/PhysRevB.24.1014

[72] C. Hautmann et al., "Temperature and doping dependence of electron spin relaxation in GaSb", *Semiconductor Science and Technology* **24** (2009), 025018, DOI: 10.1088/0268-1242/24/2/025018

[73] E. E. Haller, W. L. Hansen, and F. S. Goulding, "Physics of ultra-pure germanium", *Advances in Physics* **30** (1981), 93–138, DOI: 10.1080/00018738100101357

[74] P. Li, D. Trivedi, and H. Dery, "Spin-dependent optical properties in strained silicon and germanium", *Phys. Rev. B* **87** (2013), 115203, DOI: 10.1103/PhysRevB.87.115203

[75]   M. O. Nestoklon, L. E. Golub, and E. L. Ivchenko, "Spin and valley-orbit splittings in SiGe/Si heterostructures", *Phys. Rev. B* **73** (2006), 235334, DOI: 10.1103/PhysRevB.73.235334

[76]   M. O. Nestoklon et al., "Electric field effect on electron spin splitting in SiGe/Si quantum wells", *Phys. Rev. B* **77** (2008), 155328, DOI: 10.1103/PhysRevB.77.155328

[77]   R. Vrijen et al., "Electron-spin-resonance transistors for quantum computing in silicon-germanium heterostructures", *Phys. Rev. A* **62** (2000), 012306, DOI: 10.1103/PhysRevA.62.012306

[78]   E. Gatti et al., "Ge/SiGe quantum wells on Si(111): Growth, structural, and optical properties", *Journal of Applied Physics* **116**, 043518 (2014), DOI: 10.1063/1.4891463

[79]   G. E. Moore, "Cramming more components onto integrated circuits", *Electronics* **38** (1965)

[80]   D. J. Richardson, J. M. Fini, and L. E. Nelson, "Space-division multiplexing in optical fibres", *Nature Photonics* **7** (2013), 354–362, DOI: 10.1038/nphoton.2013.94

[81]   Matthew Peach, *NEC and Corning achieve petabit optical transmission*, 2013, URL: http://optics.org/news/4/1/29, Accessed July 23, 2016

[82]   H. J. Caulfield and S. Dolev, "Why future supercomputing requires optics", *Nature Photonics* **4** (2010), 261–263, DOI: 10.1038/nphoton.2010.94

[83]   F. Idachaba, D. U. Ike, and O. Hope, "Future Trends in Fiber Optics Communication", in: *World Congress on Engineering London July*, 2014

[84]   F. M. Raymo, "Digital Processing and Communication with Molecular Switches", *Advanced Materials* **14** (2002), 401–414

[85]   V. R. Almeida et al., "All-optical control of light on a silicon chip", *Nature* **431** (2004), 1081–1084, DOI: 10.1038/nature02921

[86]   *Web of Science*, URL: http://www.webofknowledge.com, Accessed July 24, 2016

[87]   R. Charbonneau et al., "Passive integrated optics elements based on long-range surface plasmon polaritons", *Journal of Lightwave Technology* **24** (2006), 477–494, DOI: 10.1109/JLT.2005.859856

[88]   S. Bozhevolnyi, *Plasmonic Nanoguides and Circuits*, Pan Stanford, 2009

[89] H. Gorniaczyk et al., "Single-Photon Transistor Mediated by Interstate Ry-
      dberg Interactions", *Phys. Rev. Lett.* **113** (2014), 053601, DOI: `10.1103/`
      `PhysRevLett.113.053601`

[90] D. Tiarks et al., "Single-Photon Transistor Using a Förster Resonance", *Phys.*
      Rev. Lett. **113** (2014), 053602, DOI: `10.1103/PhysRevLett.113.053602`

[91] D. A. B. Miller, "Are optical transistors the logical next step?", *Nature*
      Photonics **4** (2010), 3–5, DOI: `10.1038/nphoton.2009.240`

[92] D. Ballarini et al., "All-optical polariton transistor", *Nature Communications*
      4 (2013), 1778, DOI: `10.1038/ncomms2734`

[93] S. I. Pekar, "The Theory of Electromagnetic Waves in a Crystal in which
      Excitons Are Produced", *Journal of Experimental and Theoretical Physics*
      (1957), [ZhETF, **33**, (1958), 1022]

[94] J. J. Hopfield, "Theory of the Contribution of Excitons to the Complex
      Dielectric Constant of Crystals", *Phys. Rev.* **112** (1958), 1555–1567, DOI:
      `10.1103/PhysRev.112.1555`

[95] R. G. Ulbrich and G. W. Fehrenbach, "Polariton Wave Packet Propagation
      in the Exciton Resonance of a Semiconductor", *Phys. Rev. Lett.* **43** (1979),
      963–966, DOI: `10.1103/PhysRevLett.43.963`

[96] T. V. Shubina et al., "Resonant Light Delay in GaN with Ballistic and
      Diffusive Propagation", *Phys. Rev. Lett.* **100** (2008), 087402, DOI: `10.`
      `1103/PhysRevLett.100.087402`

[97] S. L. Chen, W. M. Chen, and I. A. Buyanova, "Slowdown of light due to
      exciton-polariton propagation in ZnO", *Phys. Rev. B* **83** (2011), 245212,
      DOI: `10.1103/PhysRevB.83.245212`

[98] Y. Okawachi et al., "Tunable All-Optical Delays via Brillouin Slow Light in
      an Optical Fiber", *Phys. Rev. Lett.* **94** (2005), 153902, DOI: `10.1103/`
      `PhysRevLett.94.153902`

[99] A. C. Schaefer and D. G. Steel, "Nonlinear Optical Response of the GaAs
      Exciton Polariton", *Phys. Rev. Lett.* **79** (1997), 4870–4873, DOI: `10.1103/`
      `PhysRevLett.79.4870`

[100] G. Göger et al., "Ultrafast Optical Spectroscopy of Large-Momentum Ex-
      citons in GaAs", *Phys. Rev. Lett.* **84** (2000), 5812–5815, DOI: `10.1103/`
      `PhysRevLett.84.5812`

[101] H. Wang et al., "Transient nonlinear optical response from excitation induced dephasing in GaAs", *Phys. Rev. Lett.* **71** (1993), 1261–1264, DOI: `10.1103/PhysRevLett.71.1261`

[102] J. M. Shacklette and S. T. Cundiff, "Role of excitation-induced shift in the coherent optical response of semiconductors", *Phys. Rev. B* **66** (2002), 045309, DOI: `10.1103/PhysRevB.66.045309`

[103] T. Godde et al., "Subnanosecond delay of light in $Cd_xZn_{1-x}Te$ crystals", *Phys. Rev. B* **82** (2010), 115332, DOI: `10.1103/PhysRevB.82.115332`

[104] T. Takahashi and S. Watanabe, "Recent progress in CdTe and CdZnTe detectors", *IEEE Transactions on Nuclear Science* **48** (2001), 950–959, DOI: `10.1109/23.958705`

[105] A. Rohatgi et al., "Investigation of polycrystalline CdZnTe, CdMnTe, and CdTe films for photovoltaic applications", *Solar Cells* **27** (1989), 219–230, DOI: `10.1016/0379-6787(89)90030-6`

[106] J. Lohrenz et al., "Ultrafast dynamical response of the lower exciton-polariton branch in CdZnTe", *Phys. Rev. B* **93** (2016), 075201, DOI: `10.1103/PhysRevB.93.075201`

[107] S. Melzer, "Ultrafast optical control over the exciton polariton propagation in CdZnTe", MA thesis, Technische Universität Dortmund, 2014

[108] G. H. Wannier, "The Structure of Electronic Excitation Levels in Insulating Crystals", *Phys. Rev.* **52** (1937), 191–197, DOI: `10.1103/PhysRev.52.191`

[109] J. Frenkel, "On the Transformation of Light into Heat in Solids. II", *Phys. Rev.* **37** (1931), 1276–1294, DOI: `10.1103/PhysRev.37.1276`

[110] T. Kazimierczuk et al., "Giant Rydberg excitons in the copper oxide Cu_2O", *Nature* **514** (2014), 343–347, DOI: `10.1038/nature13832`

[111] P. Horodyský and P. Hlídek, "Free-exciton absorption in bulk CdTe: temperature dependence", *physica status solidi (b)* **76** (2006), 494–501, DOI: `10.1002/pssb.200541402`

[112] K. Kopitzki and P. Herzog, *Einführung in die Festkörperphysik*, Vieweg + Teubner Verlag, 2007

[113] J. J. Hopfield and D. G. Thomas, "Theoretical and Experimental Effects of Spatial Dispersion on the Optical Properties of Crystals", *Phys. Rev.* **132** (1963), 563–572, DOI: `10.1103/PhysRev.132.563`

[114] A. Otto, "Excitation of nonradiative surface plasma waves in silver by the method of frustrated total reflection", *Zeitschrift für Physik* **216** (1968), 398–410, DOI: `10.1007/BF01391532`

[115] R. H. Lyddane, R. G. Sachs, and E. Teller, "On the Polar Vibrations of Alkali Halides", *Phys. Rev.* **59** (1941), 673–676, DOI: `10.1103/PhysRev.59.673`

[116] Y. Segawa, Y. Aoyagi, and S. Namba, "Anomalously slow group velocity of upper branch polariton in CuCl", *Solid State Communications* **32** (1979), 229–231, DOI: `10.1016/0038-1098(79)90127-3`

[117] T. Itoh et al., "Time of flight of excitonic polaritons in CdSe", *Solid State Communications* **37** (1981), 925–930, DOI: `10.1016/0038-1098(81)91188-1`

[118] N. A. Vidmont, A. A. Maksimov, and I. I. Tartakovskii, "Measurement of the group velocity of polaritons in anthracene crystal", *JETP Letters* **37** (1983), 689, [Pis'ma Zh. Eksp. Teor. Fiz. 37, 578 (1983)]

[119] G. Manzke et al., "Density Dependence of the Exciton Energy in Semiconductors", *Phys. Rev. Lett.* **80** (1998), 4943–4946, DOI: `10.1103/PhysRevLett.80.4943`

[120] M. Joffre et al., "Coherent effects in pump-probe spectroscopy of excitons", en, *Optics Letters* **13** (1988), 276, DOI: `10.1364/OL.13.000276`

[121] C. Ruppert et al., "Ultrafast field-resolved semiconductor spectroscopy utilizing quantum interference control of currents", *Opt. Lett.* **37** (2012), 3879–3881, DOI: `10.1364/OL.37.003879`

[122] M. D. Dvorak et al., "Measurement of the anisotropy of two-photon absorption coefficients in zincblende semiconductors", *IEEE Journal of Quantum Electronics* **30** (1994), 256–268, DOI: `10.1109/3.283768`

[123] A. A. Said et al., "Determination of bound-electronic and free-carrier nonlinearities in ZnSe, GaAs, CdTe, and ZnTe", en, *J. Opt. Soc. Am. B* **9** (1992), 405, DOI: `10.1364/JOSAB.9.000405`

[124] E. W. Van Stryland et al., "Two Photon Absorption, Nonlinear Refraction, And Optical Limiting In Semiconductors", *Optical Engineering* **24** (1985), 244613, DOI: `10.1117/12.7973538`

[125] R. Boyd, *Nonlinear Optics*, Academic Press, 2008

[126] T. Meier, P. Thomas, and S. W. Koch, *Coherent Semiconductor Optics*, en, Springer Berlin Heidelberg, 2007

[127] M. Okoniewski, M. Mrozowski, and M. A. Stuchly, "Simple treatment of multi-term dispersion in FDTD", *IEEE Microwave and Guided Wave Letters* **7** (1997), 121–123, DOI: 10.1109/75.569723

[128] A. Taflove and S. C. Hagness, *Computational Electrodynamics: The Finite-Difference Time-Domain Method, Third Edition*, Artech House, Boston, MA, 2005

[129] T. Elsaesser et al., "Initial thermalization of photoexcited carriers in GaAs studied by femtosecond luminescence spectroscopy", *Phys. Rev. Lett.* **66** (1991), 1757–1760, DOI: 10.1103/PhysRevLett.66.1757

[130] E. S. Barnard et al., "Probing carrier lifetimes in photovoltaic materials using subsurface two-photon microscopy", *Scientific Reports* **3** (2013), 2098 EP, DOI: 10.1038/srep02098

[131] Y. P. Varshni, "Temperature dependence of the energy gap in semiconductors", *Physica* **34** (1967), 149–154, DOI: 10.1016/0031-8914(67)90062-6

[132] E. López-Cruz et al., "Photoconductive characterization of $Zn_xCd_{1-x}Te$ ($0 \leq x \leq 0.25$) single crystal alloys", *Journal of Vacuum Science & Technology A* **8** (1990), 1934–1938, DOI: 10.1116/1.576785

[133] "Zn(x)Cd(1-x)Te electronic properties", in: *II-VI and I-VII Compounds; Semimagnetic Compounds*, ed. by O. Madelung, U. Rössler, and M. Schulz, Springer Berlin Heidelberg, 1999, pp. 1–8, DOI: 10.1007/10681719_713

Publications

C. Ruppert, J. Lohrenz, S. Thunich, and M. Betz:
"Ultrafast field-resolved semiconductor spectroscopy utilizing quantum interference control of currents"
Optics Letters Vol. **37**, Issue 18, pp. 3879-3881 - Published 14 September 2012

J. Lohrenz, T. Paschen, C. Hautmann, M. Betz:
"Optical tailoring of electron and hole spin polarization in bulk germanium"
Proc. SPIE **8984**, Ultrafast Phenomena and Nanophotonics XVIII, 898418 - Published 7 March 2014

J. Lohrenz, T. Paschen, and M. Betz:
"Resonant spin amplification in intrinsic bulk germanium: Evidence for electron spin lifetimes exceeding 50 ns"
Phys. Rev. B **89**, 121201(R) - Published 10 March 2014

J. Lohrenz, S. Melzer, C. Ruppert, I. A. Akimov, H. Mariette, M. Reichelt, A. Trautmann, T. Meier, and M. Betz:
"Ultrafast dynamical response of the lower exciton-polariton branch in CdZnTe"
Phys. Rev. B **93**, 075201 - Published 2 February 2016

Acknowledgments

I would like to thank everyone who directly or indirectly contributed to the completion of this thesis. In particular, I would like to extend my gratitude to the following people:

- **My Workmates at E2** and **fellow students from the physics department** for a continuous, pleasant working atmosphere. Besides those already mentioned, special thanks to: **Dr. Sergiu Anghel, Thomas Czerniuk, Dr. Johannes Hackmann, Thorben Jostmeier, Laura Kodytek, Felix Paßmann, Dr. Martin Pohl, Dr. Elmar Sternemann,** and **Dr. Sebastian Thunich**.

- **Thomas Czerniuk**, **Geoff Phillips**, and **Dr. Elmar Sternemann** for proofreading.

- The entirety of the **Piratenbrüder Hildesheim** for fun and recreation.

- **My family** for their love and unconditional support.

- **Laura Rosenberg** for her caring love and support and for being the mother of our daughter **Luise Karola** (*August 01, 2016), whose imminent arrival provided a great source of motivation during the writing of this thesis.